CZECH TECHNICAL UNIVERSITY IN PRAGUE

FACULTY OF NUCLEAR SCIENCES AND PHYSICAL ENGINEERING

DEPARTMENT OF PHYSICAL ELECTRONICS

DOCTORAL THESIS

Development of a cryogenic 2 μm multi-pass amplifier in nanosecond regime

Prague 2021 FANGXIN YUE

UNIVERSITAT ROVIRA I VIRGILI

Departament de Química Física i Inorgànica

Universitat Rovira i Virgili
Campus Sescelades
Marcel·lí Domingo, nº1.
43007 Tarragona
Spain

CZECH TECHNICAL UNIVERSITY IN PRAGUE

Faculty of Nuclear Sciences and Physical Engineering

Břehová 7, 115 19 Praha 1
Czech Republic
Tel.: +420 22435 8310
Fax: +420 22232 0861
E-mail: info@fjfi.cvut.cz

WE STATE that the present study, entitled "Development of a cryogenic 2 μm multi-pass amplifier in nanosecond regime," presented by Fangxin Yue for the award of the degree of Doctor, has been carried out under the supervision at the Department of Inorganic and Physical Chemistry of the University of Rovira i Virgili in Tarragona, Spain & at the Faculty of Nuclear Sciences and Physical Engineering of Czech Technical University in Prague, and that it fulfils all the requirements to be eligible for the International Doctorate Award.

Tarragona, 29.03.2021
Prague, 29.03.2021

Doctoral Thesis Supervisor

Prof. Dr. Xavier Mateos | Dr. Jan Šulc | Dr. Venkatesan Jambunathan

BIBLIOGRAPHIC ENTRY

Author:	Fangxin Yue Czech Technical University in Prague, Prague, Czech Republic Faculty of Nuclear Sciences and Physical Engineering Department of Physical Electronics University Rovira i Virgili, Tarragona, Spain Department of Inorganic and Physical Chemistry

Title of Dissertation:	Development of a cryogenic 2 μm multi-pass amplifier in nanosecond regime
Degree programme:	Applications of Nature Science & Nanoscience, Materials and Chemical Engineering
Field of Study:	Physical Engineering

Supervisor CTU:	Ing. Jan Šulc, Ph.D. Department of Physical Electronics, CTU in Prague
Supervisor URV:	Prof. Dr. Xavier Mateos Department of Inorganic and Physical Chemistry, URV
Supervisor specialist:	Dr. Venkatesan Jambunathan HiLASE Centre, Institute of Physics of the CAS

Academic Year:	2020/2021
Number of Pages:	89
Keywords:	DPSSL, MOPA, cavity dumping, Tm:Y_2O_3, transparent ceramic, spectroscopy

BIBLIOGRAFICKÝ ZÁZNAM

Autor: Fangxin Yue
Český vysoké učení technické v Praze
Fakulta jaderná a fyzikálně inženýrska
Katedra fyzikální elektroniky

University Rovira i Virgili, Tarragona, Španělsko
Katedra anorganické a fyzikální chemie

Název práce: Vývoj kryogenního 2 μm vícepásmového zesilovače v nanosekundovém režimu

Studijní program: Aplikace přírodních věd &
Nanovědy, materiály a chemické inženýrství

Studijní obor: Fyzikální inženýrství

Školitel CTU: Ing. Jan Šulc, Ph.D.
Katedra fyzikální elektroniky, ČVUT v Praze

Školitel URV: Prof. Dr. Xavier Mateos
Katedra anorganické a fyzikální chemie, URV

Školitel specialista: Dr. Venkatesan Jambunathan
Centrum HiLASE, Fyzikální ústav AV ČR, v. v. i.

Akademický rok: 2020/2021

Počet stran: 89

Klíčová slova: DPSSL, MOPA, otevřená dutiny, Tm:Y_2O_3, transparentní keramika, spektroskopie

ABSTRACT

Motivated by the increasing application demands on the 2 μm high average/peak power lasers, this thesis is devoted to develop a cryogenic 2 μm multi-pass amplifier in the nanosecond regime based on the Tm:Y_2O_3 transparent ceramics. To reach this goal, the active medium Tm:Y_2O_3 transparent ceramic was well studied and the master oscillator power amplifier concept was employed for developing the cryogenic laser system.

This work is divided into 7 chapters. Chapter 1 introduces the current state-of-the-art of the 2 μm pulsed lasers as well as the motivation and objectives of this dissertation. Chapters 2, 3 and 4 describe the characterization of the active medium Tm:Y_2O_3 transparent ceramic in terms of material structure, cryogenic spectroscopy, and continuous-wave lasing potential, respectively. From those studies, crucial laser design parameters, such as the exact pump/lasing wavelength, lifetime, gain factor, etc., were obtained. Chapter 5 presents the demonstration of a master oscillator, which served as the seed source for the amplifier stage. Chapter 6 shows the energy scaling via the multi-pass amplifier in two different geometries. Finally, chapter 7 summarizes the achieved results and outlooks the future research.

ABSTRAKT

Tato práce je motivována rostoucími požadavky na lasery s vysokým středním/špičkovým výkonem generujícími v okolí vlnové délky 2 μm a jejím cílem je vyvinout kryogenní 2 μm víceprůchodový zesilovač pracující s impulzy v nanosekundovém režimu založený na transparentní keramice Tm:Y_2O_3. K dosažení tohoto cíle byla detailně studována transparentní keramika Tm:Y_2O_3 sloužící jako aktivní prostředí a pro vývoj kryogenního laserového systému byl použit koncept řídící oscilátor - výkonový zesilovač.

Tato práce je rozdělena do sedmi kapitol. Kapitola 1 popisuje současný stav impulzních 2 μm laserů a obsahuje motivaci a cíle této disertační práce. V kapitolách 2, 3 a 4 jsou popsány charakterizace aktivního média - transparentní keramiky Tm:Y_2O_3 - z hlediska struktury materiálu, spektroskopie od pokojové po kryogenní teploty a potenciálu laseru generujícího v kontinuálním režimu. Tyto výzkumy byly použity pro získání parametrů nezbytných pro návrh laseru, jako je přesná vlnová délka čerpacího záření, doba života na horní laserové hladině, součinitel zesílení zesílení atd. Kapitola 5 popisuje konstrukci a parametry řídícího oscilátoru, který sloužil jako zdroj zadávacích impulzu pro následující stupně zesilovače. Kapitola 6 popisuje konstrukci a výsledky získané pomocí

víceprůchodového zesilovače testovaného ve dvou různých konfiguracích. Závěrečná kapitola 7 shrnuje dosažené výsledky a výhledy budoucího výzkumu.

RESUMEN

Motivada por la creciente demanda de aplicación de los láseres de potencia media / pico alta a 2 μm, esta tesis doctoral está dedicada a desarrollar un amplificador criogénico multipaso a 2 μm en régimen de nanosegundos basado en la cerámica transparente Tm:Y_2O_3. Para alcanzar este objetivo, se estudió a fondo la cerámica transparente Tm:Y_2O_3 como medio activo y se empleó el concepto de amplificador de potencia de oscilador maestro (*master oscillator power amplifier*) para desarrollar el sistema láser criogénico.

Este trabajo se divide en 7 capítulos. El capítulo 1 presenta el estado actual de los láseres pulsados a 2 μm, así como la motivación y los objetivos de esta tesis. Los capítulos 2, 3 y 4 describen las caracterizaciones del medio activo (cerámica transparente Tm:Y_2O_3) en términos de estructura del material, espectroscopía criogénica y potencial láser en onda continua. A partir de esos estudios, se obtuvieron parámetros cruciales en el diseño del láser, como la longitud de onda exacta de bombeo / láser, la vida media del nivel emisor, el factor de ganancia, etc. El capítulo 5 presenta la demostración de un oscilador maestro (*master oscillator*), que sirvió como fuente semilla para la etapa del amplificador. El capítulo 6 muestra el escalado en energía a través del amplificador de paso múltiple en dos geometrías diferentes. Al final, el capítulo 7 resume los resultados obtenidos y proyecta la investigación futura.

ACKNOWLEDGMENT

This work was co-financed by the European Regional Development Fund and the state budget of the Czech Republic (project HiLASE CoE: Grant No. CZ.02.1.01/0.0/0.0/15_006/0000674) and by the European Union's Horizon 2020 research and innovation programme under grant agreement No. 739573. This work was also supported by the Ministry of Education, Youth and Sports of the Czech Republic (Programmes NPU I Project No. LO1602, and Large Research Infrastructure Project No. LM2015086).

I would like to express my gratitude to Dr. Tomáš Mocek for giving me the chance to work as HiLASIAN in this word-class laser institute. I would also like to thank Dr. Miroslav Čech, Prof. Ladislav Pina from CTU and Prof. Francesc Díaz, Prof. Magdalena Aguiló from URV for their support on the this joint doctoral supervision program between two universities.

I also want to express my thanks to my late colleague Dr. Antonio Lucianetti, head of Advanced Laser Development department, HiLASE center. It is a pity that he was not able to see this work finally accomplished.

I am very grateful for all help from my supervisors Dr. Jan Šulc and Dr. Xavier Mateos as well as my supervisor specialist Dr. Venkatesan Jambunathan. Without all your supervision, this work would not be possible. I am grateful for receiving your support and learning from your experience. Thank you for the corrections to this thesis and for all the help I have received from you.

I thank my colleagues Dr. Samuel Paul David and Dr. Petr Navratil as well, for your time and patience on the laboratory collaborations and valuable scientific discussions.

I also thank all my friends including Huiying, Yi, Site and Xiaoming for accompanying and helping me all along my study and research. Last but not least, I would like to say my love and thanks to my parents, YUE Zeng and FU Yanling. You are my first and best teacher leading me onto the way of science. Without your encouragement and support, I would not have accomplished these ten years oversea study. I dedicate this thesis to you and our family with great pleasure.

Contents

FIGURE LIST

TABLE LIST

NOMENCLATURE

AR	anti-reflective
ASE	amplified spontaneous emission
BSE	back-scattered electron
CDMO	cavity-dumped master oscillator
CL	cathode luminescence
CM	curved mirror
CR	cross relaxation
CW	continuous-wave
DM	dichroic mirror
DPSSL	diode pumped solid-state laser
FL	Füchtbauer-Ladenburg
FWHM	full width half maximum
HR	high-reflective
LD	laser diode
LIDT	laser induced damage threshold
LN	liquid nitrogen
LP	long pass
MC	McCumber
MOPA	master oscillator power amplifier
N.A.	numerical aperture
ND	neutral density
N/M/FIR	near/mid/far infrared
OC	output coupler
OPO	optical parametric oscillator

PC	Pockels cell
QY	quantum yield
RE	rare-earth
ROC	radius of curvature
RTP	rubidium titanyl phosphate
SE	secondary electron
SEM	scanning electron microscopy
SSL	solid-state laser
TFP	thin film polarizer
TRAM	total-reflection active mirror
UV	ultraviolet
VBG	volume Bragg grating
VIS	visible
XRD	X-ray diffraction

Chapter 1

Introduction

This chapter provides an overview of the applications and the state-of-the-art of the pulsed 2 μm solid-state lasers. The basic information about the active medium, cryogenic cooling and master oscillator power amplifier concept are also described. To the end, the motivation and objectives of this work are presented.

1.1. State-of-the-art

LASER, as the acronym of **L**ight **A**mplification by **S**timulated **E**mission of **R**adiation, is widely accepted as a device that generates electromagnetic waves of high coherence [1]. This high spatial and temporal coherent feature of laser radiation distinguishes lasers from other light sources and enables various novel applications, which, nowadays, cover a broad range of fields from daily life over industrial fabrication to high-tech scientific research. To be noted is that "light" here refers to the electromagnetic wave of any wavelength ranging from X-ray over ultraviolet (UV), visible (VIS), near/mid/far infrared (N/M/FIR) to microwaves and radio waves [2]. Wavelength, therefore, is a key parameter to classify the lasers.

Out of them, lasers emitting at the wavelength around two-micron (2 μm), belonging to the short-wave infrared (SWIR) spectral range, have attracted growing attention in recent years. This is firstly because the 2 μm wave has high absorption in water (the main ingredient of vitreous body in human eyes) [3], which is known as "eye-safe" feature. Such lasers are more suitable in the area of remote sensing, short-range optical communication, etc., compared with other shorter wavelength lasers [4,5]. Secondly, several atmosphere gases (e.g. H_2O, CO_2, N_2O) have absorption lines at 2 μm [3], which enables the direct sensing of such gases by using two-micron lasers as a key element in LIDAR (Light Detection And Ranging) or DIAL (Differential Absorption Lidar) systems. Several high energy 2 μm lasers have been proposed and investigated by multiple groups around the world [4-7]. In addition, the 2 μm waves have a relative short penetration depth in biological tissues and show a the coagulation effect [8], which makes the high energy pulsed laser emitting in this wavelength region favorable for medical surgery, such as spinal surgery, arthroscopy, urology, etc. [3,8]. Another application of pulsed 2 μm lasers can be found in the material processing industry, such as cutting and welding of transparent plastics, processing and fabrication of transparent bio-fluidic chips, for which 2 μm lasers possessing high beam quality are preferred than the widely spread 1 μm lasers [3]. Moreover, high energy 2 μm lasers can be used in the laser induced damage threshold (LIDT) measurement, which is a necessary qualification for all optics designed for this wavelength range [9]. As for scientific research, a pulsed 2 μm laser with high peak power can serve as the pump source for nonlinear materials, OPOs/OPAs (optical parametric oscillators/amplifiers) or Cr^{2+}-doped lasers to generate mid- and far-IR radiation [10-12].

In all above-mentioned applications, pulsed 2 μm lasers with high average and peak power (HAPP) are mostly required. To achieve pulsed lasing, active and passive Q-switching

are two commonly used techniques. Among these two, the active Q-switching is more preferred for HAPP laser demonstration due to its multiple advantages. For example, actively Q-switched pulses can reach a much higher energy, e.g., mJ even hundreds of mJ. However, the passively Q-switched ones have usually pulse energies of only μJ [13]. Moreover, the repetition rate is controllable in the active Q-switching process and the pulse duration is less affected by the repetition rate. Thus, high energy short pulses with variable repetition rate can be obtained.

In the past two decades, several active media with different switching materials (acousto/electro optics (AO/EO)) have been studied for the 2 μm HAPP laser development. An overview of the actively Q-switched 2 μm solid-state lasers is presented in Table 1-1. In [15], the highest pulse energy of 550 mJ and peak power of 39 MW were reported using Ho:YLF as active medium and an EO switch. However, its repetition rate was limited to only 1 Hz. For high repetition rate operation, as example, a laser was reported in [16] based on Tm:YAP generating pulses at a repetition rate of 200 kHz. However, its pulse energy reached only 13.9 μJ, resulting in a low peak and average power. The highest average power reported was 106 W in [17], which used Ho:YAG as the active medium and AO switch for pulse generation. The single pulse energy of 5.3 mJ, peak power of 252 kW, and repetition rate of 20 kHz were also added credit to this laser. However, the beam quality of this laser was reported as M^2 of only 1.6.

Table 1-1 Overview of the actively Q-switched 2 μm solid-state lasers [14]

Active medium	Wavelength [nm]	Energy [mJ]	Pulse width [ns]	Repetition rate [kHz]	Peak power [kW]	Average power [W]	Switch
Tm:YAG	2015	128	160	0.01	800	1.28	AO
Tm:YAP	1990	1.6	126	6	12.7	9.6	AO
Tm:YAP	1940	7	75	5	93	35	AO
Tm:LuAG	2023	0.53	170	1	3	0.53	AO
Tm,Y:CaF_2	1912	0.335	280	1	1.2	0.335	AO
Tm:YbAG	2020	0.1	45	6.7	2.2	0.67	AO
*Tm:YLF	1908	10	47	0.133	220	1.33	AO
Tm,Ho:$GdVO_4$	2050	1.1	23	3	47.8	3.3	AO
Tm,Ho:YVO_4	2055	1.3	24.2	15	53.7	19.5	AO
Tm,Ho:YAP	2119	0.97	66.85	7.5	14.5	7.3	AO
Ho:YAG	2090	30	100	0.1	300	3	AO
Ho:YAG	2090	5.3	21	20	252	106	AO
Ho:YLF	2060	1.1	43	0.1	25.6	0.11	AO
Ho:$GdVO_4$	2050	0.9	4.7	5	191	4.5	AO
**Ho:YAG	2090	2.4	8.8	4	272.7	9.6	AO
Tm:YAG	2015	7.5	58	1	129	7.5	EO

Tm:YAP	1990	0.0139	5.5	200	2.5	2.78	EO
Tm:LuAG	2013	0.0122	3	100	4.1	1.22	EO
Tm:LuAG	2023	10.8	52	0.1	207.7	1.08	EO
Tm, Ho:YAP	2130	1.65	107	0.2	15.4	0.33	EO
Ho:YLF	2051	550	14	0.001	3.9×10^4	0.55	EO

* was cited from [18], and ** from [19]

Based on the above studied reports, one can see that, although various materials and laser techniques have been tested, it is still an ongoing and challenging task to develop pulsed 2 μm lasers with demanded performances, such as high brightness, high average/peak power, high single pulse energy, short pulse width, operational ease, low cost, etc. One of the main bottlenecks limiting the 2 μm HAPP laser performance is the thermal management of the active medium. The heat deposited in the laser active medium during intense pumping results in important thermal gradients inside the sample causing unwanted thermal issues, such as thermal lensing, thermal induced mechanical stress, even thermal induced damages in the gain medium, etc. Therefore, it is highly motivated to explore novel 2 μm laser active media with advanced thermo-optical/-mechanical properties and laser potential, to study the effect of cryogenic laser operation to limit the thermal issues, as well as to explore various laser configurations to achieve high power scaling in the 2 μm laser development.

1.2. Background

1.2.1 Laser active medium

For the 2 μm HAPP laser development, the active medium, a key component of a solid-state laser (SSL), must be precisely studied. This is mainly because the basic properties of a SSL are dominated by the interaction of the laser-active ion and the host lattice [2]. Here, in this section, the dopant ion (laser-active ion), the host material (host lattice), and the advantages of transparent ceramics are introduced.

- **Dopant ion: trivalent thulium (Tm^{3+})**

Among the rare-earth (RE) ions, the lanthanide series, are natural candidates for SSL as active ions. This is because of their sharp VIS and IR transitions within the 4f sub shell [20]. Among these ions, to achieve the 2 μm emission, the trivalent thulium (Tm^{3+}) and holmium (Ho^{3+}) (hereafter Tm and Ho) are of great interest. The Tm lasers have emissions in the range of 1.9 – 2 μm due to the $^3F_4 \rightarrow {}^3H_6$ transition, while the Ho lasers exhibit a $^5I_7 \rightarrow {}^5I_8$ transition in the 1.95 – 2.15 μm range [21].

In this work, the Tm-doped materials are preferred for two reasons. Firstly, Tm materials can be easily pumped by ~ 800 nm diode lasers, which are commercial, well-established and

cheap. As shown in Figure 1-1, the Tm ion can be excited from the ground state $^3H_6$ to the higher energy level $^3H_4$. This energy difference amounts to ~ 800 nm, which matches well with the emission wavelength of the commercially available AlGaAs diode lasers. This ease of pumping scheme is advantageous compared with that for Ho-doped lasers, whose pump sources based on GaSb diodes are not mature yet for reliable pumping.

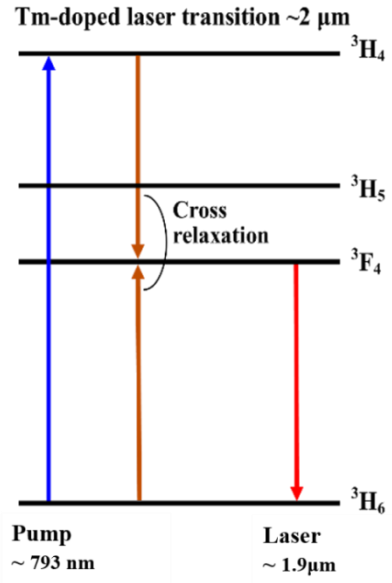

Figure 1-1 Energy levels Tm. Relevant pump and laser transitions of the Tm ion.

The other advantage of the Tm lasers is the so-called "two-for-one" effect or cross-relaxation (CR) process. In this phonon assistant process, the upper laser level ($^3F_4$) is populated by two Tm ions for each absorbed pump photon: one coming from $^3H_4$ and the other one from $^3H_6$ [22]. Thus, the slope efficiency of Tm lasers can be strongly increased by the CR, which can be quantified by the parameter quantum yield (QY). With an ideally efficient CR, the maximum QY value η_{QY} = 2 can be reached, which means the quantum defect limited slope efficiency of ~ 40 % will be doubled to ~ 80 % for Tm lasers. A detailed study on how the QY influences the laser slope efficiency will be presented in 4.1.1.

- **Host material: yttrium oxide (Y_2O_3)**

The host material also plays a critical role in the laser design, mainly for two reasons. Firstly, the crystal field and symmetry of the host lattice influence the exact energy level positions of each manifold, especially of the Stark splitting, consequently influence the exact transition wavelength/bandwidth, lifetime, etc. of the laser. Secondly, the host material strongly influences the thermo-mechanical/-optical properties of the active medium, which further influences the thermal management and the overall performance of the laser.

Here, we focused on the host material yttrium oxide (Y_2O_3), which is a cubic oxide material and belongs to the sesquioxide family (RE_2O_3, RE = Y, Sc, Lu). Sesquioxides are promising host materials for the trivalent Tm dopant mainly due to their good thermal, mechanical, and optical properties. Some basic parameters of the three sesquixoides are shown in Table 1-2. Accordingly, one can see that sesquioxides have higher thermal conductivity compared with the widely used host material YAG (0.11 W/cm·K for un-doped YAG at room temperature [23]). In addition, the cation densities of sesquioxides are much higher compared to YAG's 1.38×10^{22} cm^{-3}. This high cation density enables the possibility of higher dopant concentration [25]. Besides, the Tm-doped sesquioxides also have very broad emission spectra, which are beneficial for the short-pulse generation and tunable laser design [26]. Among the three sesquioxides, Y_2O_3 is favored for multiple reasons. For instance, the maximum phonon energy of Y_2O_3 is the lowest compared to the other two sesquioxides, which reduces the multi-phonon relaxation losses during laser operation. Secondly, the thermo-optic coefficient and thermal expansion coefficient of Y_2O_3 are the smallest within the sesquioxide family, which minimizes the trouble from thermal lensing and thermal stress. In addition, compared with the other two materials, Y_2O_3 also exhibits price superiority, which is much beneficial in further industrial or medical applications.

Table 1-2 Properties of sesquioxide host materials [24]

	Lu_2O_3	Sc_2O_3	Y_2O_3
Lattice	cubic	cubic	cubic
Space group	$Ia\bar{3}$	$Ia\bar{3}$	$Ia\bar{3}$
Site symmetry	C_2/C_{3i}	C_2/C_{3i}	C_2/C_{3i}
Coordination number	6	6	6
Cation radius [Å]	0.86	0.75	0.9
Lattice constant [Å]	10.391	9.857	10.602
Cation density [10^{22} cm^{-3}]	2.852	3.355	2.687
Density [g/cm^3]	9.42	3.85	5.03
Melting point [℃]	2450	2430	2430
Mohs hardness	6 ½	6 ½	6 ½
Young's modulus [GPa]	180	200	180
Refractive index at 2 μm	1.896	1.946	1.874
Transparency range [μm]	0.225 - 8	0.210 - 8	0.220 – 8
Specific heat [J/g·K]	0.24	0.70	0.44
Thermal conductivity undoped	12.8	18	13.4
1 at.% Yb-doped	~ 12.5	~ 9.2	~ 10.0
Thermo-optic coefficient dn/dT [10^{-6} K^{-1}]	9.1	8.9	8.5
Thermal expansion coefficient 1/L dL/dT [10^{-6} K^{-1}]	8.6	9.6	8.5
Max. Phonon energy [cm^{-1}]	618	672	597

- **Transparent laser ceramics**

To date, only limited laser operations have been reported using the crystal-based Tm-doped Y_2O_3. This is mainly because of the difficulties in growing the crystal due to its feature of high melting point and phase transition below the melting point. Moreover, growing a crystal with large volume is also a challenging task that costs long process time and high expense [27]. Therefore, alternatives are demanded in the laser community. The laser quality transparent ceramic is a good candidate.

As a laser active media, transparent laser ceramics have many advantages. The first and most important advantage is the ease of ceramic fabrication compared to crystal growth. For instance, the sintering temperature for Y_2O_3 is only around 1700 ℃, which is much lower than its melting point (2430 ℃) [28]. Secondly, the fabrication process of transparent laser ceramics enables to produce laser ceramics with high dopant concentration and large sample volume, which improves the power scaling capacity of high power lasers, as well as mass production. Moreover, various geometries of composite ceramics are also possible, as shown in Figure 1-2, which can be used to suppress parasitic losses, to control the spectrum, to control the gain volume, and so on [29].

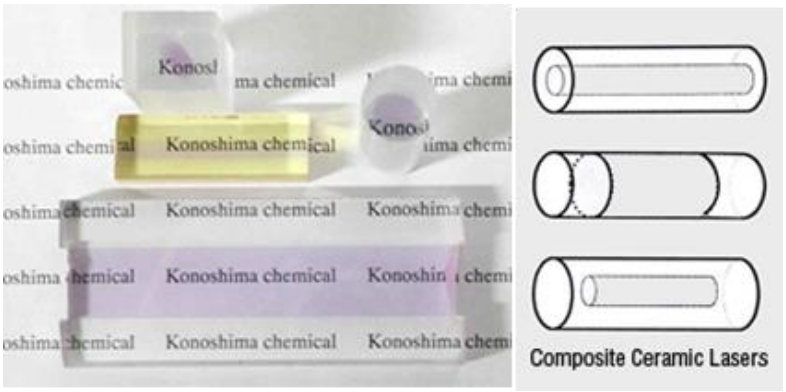

Figure 1-2 Novel structures of composite laser ceramics [30]

The use of ceramic-based Tm-doped sesquioxides have been reported by many researches [28, 31-33]. Several lasers using Tm:Y_2O_3 ceramics were demonstrated at room temperature. In [34], a CW laser with a maximum output of 2.4 W and 0.3 W were achieved for laser emission at 1.95 and 2.05 μm, respectively. Reference [35] reported both CW and Q-switched laser operation around 2050 nm. The maximum output for the CW laser was 7.2 W corresponding to 40 % slope efficiency. In the Q-switching operation, the authors obtained 1 kHz pulses with the shortest pulse width of 115 ns. A planar-waveguide laser was also reported in [36]. Using a volume Bragg grating, a laser around 2.1 μm was also demonstrated

[37]. In this work, commercial Tm:Y_2O_3 ceramics were employed as the active medium for the seed source demonstration and were also used for the amplifier design.

1.2.2 Cryogenic cooling

As mentioned in Section 1.1, the thermal management is the main bottleneck in the diode-pumped Tm HAPP laser development. The difficulties are mainly due to the large quantum defect of the Tm ions and their quasi-three-level nature at room temperature, as well as other parasitic processes. To mitigate these issues, cooling the active medium down to cryogenic temperatures is a commonly used technique [38,39]

Cryogenic cooling of the laser active medium was applied in the first demonstration of a SSL and has been attractive for the laser community ever since. The advantages of cryogenic cooling are in multiple aspects. Firstly, the thermo-optical and thermo-mechanical properties of the active medium get enhanced when the active medium is cooled down to cryogenic temperature [23]. The unwanted thermal-related issues during laser operation, such as thermal aberration, thermal lensing, thermal induced mechanical stress, etc., can be suppressed. As an example, the thermal conductivity, thermal expansion coefficient and dn/dT of Y_2O_3 are shown in Figure 1-3. One can see from the figure that the thermal conductivity increases 4 times from 0.13 W/cm·K at 300 K to 0.52 W/cm·K at 100 K, while the expansion coefficient decreases to only 1/7 from 6.3 to 0.9 10^{-6} K^{-1}.

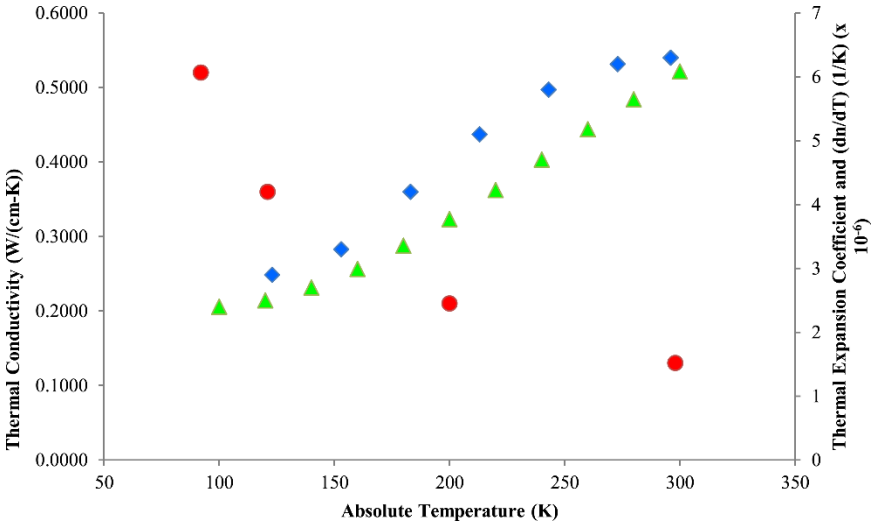

Figure 1-3 Y_2O_3 thermal conductivity (red circles), thermal expansion coefficient (blue diamonds), and (dn/dT) (green triangles) as a function of absolute temperature [39].

Secondly, cooling the active medium to cryogenic temperatures increases the transition cross-sections of the active medium due to the linewidth narrowing at lower temperatures. As shown in Table 1-3, the absorption cross-section of Tm:Y_2O_3 increases around 1.5 times from 2.83×10^{-21} at 300 K to 4.62×10^{-21} cm^2 at 100 K. The same trend is observed also from the

emission and gain cross-sections. Hence, higher output power can be achieved with lower pump power at cryogenic temperatures.

Table 1-3 Temperature dependent cross-sections of Tm:Y_2O_3 (measured)

Temperature [K]	σ_{abs} @793 nm [10^{-21} cm^2]	σ_{ami} @1932 nm [10^{-21} cm^2]	σ_{gain} @1932 nm β = 0.1 [10^{-21} cm^2]
100	4.62	23.6	2.6
200	3.46	12.4	1.0
300	2.83	7.5	0.45

In addition, the Stark splitting of the Tm ground state gets thermally depopulated at cryogenic temperatures, which results in a four-level system from quasi-three-level. Therefore, this results in minimizing the reabsorption losses, reducing the pump threshold as well as enhancing the power scaling capability. Moreover, other unwanted processes of the Tm-doped materials, such as the excited state absorption (ESA), energy-transfer upconversion (ETU), etc., can be suppressed at cryogenic temperatures leading to an increased overall efficiency [40].

Applications of the cryogenic cooling technique can be found in many high power laser systems. For example, cryogenic cooling setups are employed in the total reflection active mirror (TRAM) amplifiers reported in [41], and in large laser facilities such as DiPOLE [42] and Bivoj [43], which are able to generate 100 Joule-class, high-energy, nanosecond pulsed laser. However, these laser systems are mostly based on ytterbium or neodymium doped material emitting around 1 μm. Cryogenic 2 μm laser based on Tm is still under investigation.

1.2.3 Master oscillator power amplifier

To achieve high power scaling with demanded laser performance, the master oscillator power amplifier (MOPA) is a commonly used concept. In a MOPA system, the master oscillator is designed to generate the initial laser seed pulses, whose most performance aspects, such as the laser wavelength, beam quality, pulse duration, and repetition rate, can be disconnected from generating high power. Thus, the seed laser gains more flexibility but reduces the damage risk of the employed optical components. Correspondingly, the power scaling is achieved in the following single or multiple amplifier stages, where the injected seed pulse energy is amplified to the aimed value and other laser properties are maintained the same as the seed. Thus, the MOPA system can generate relatively short pulses with high power, high beam quality, and adjustable repetition rate [13]. To date, many two-micron lasers have been demonstrated based on the MOPA concept, although only at room temperature. In [44], a 600

mJ Ho:Tm:LuLF laser was reported using a MOPA system. Then, the same group using double-stage amplifier increased the output energy to 1.05 J [45]. In [46], a 30 mJ MOPA system based was reported using Ho:YLF as gain medium. In [47], 200 nJ pulse energy and 11.2 kW peak power were achieved using a thulium-doped all-fiber MOPA system.

1.3. Motivation and objectives

Due to the increasing application demands on 2 μm HAPP lasers, developing such lasers becomes much attractive in the laser society. However, many difficulties still need to be addressed, such as thermal management, finding the proper pump source, clear understanding of the active media's properties, etc.

Bared all these facts in mind, it is decided to take this challenging task to develop a compact two-micron HAPP laser. Thus, the general objective of this work was to demonstrate a cryogenic 2 μm multi-pass amplifier in the nanosecond regime based on Tm-doped Y_2O_3 transparent ceramics. In order to achieve this general objective, several objectives need to be attained.

The first objective was to study the material properties of the Tm:Y_2O_3 transparent ceramic. To accomplish this objective, the Tm:Y_2O_3 transparent ceramic was studied in terms of material structure, cryogenic spectroscopy, and lasing potential. From this study, crucial laser design parameters, such as the exact pump wavelength, laser wavelength, lifetime, gain behavior, optimal operation temperature, etc., were obtained.

The second objective was to demonstrate a suitable seed source emitting at 2 μm based on cryogenically cooled Tm:Y_2O_3 transparent ceramics. To fulfill this objective, a laser oscillator with tunable repetition rate was demonstrated at cryogenic temperature.

The final objective was to demonstrate a cryogenic multi-pass amplifier using the Tm:Y_2O_3 transparent ceramic as the gain medium. This objective was accomplished at liquid nitrogen temperature via various geometries. A double-pass geometry was designed to optimize the amplifier parameters and a four-pass setup was used for energy scaling.

1.4. References

[1] K. F. Renk, *Basics of Laser Physics: For Students of Science and Engineering*, Springer-Verlag Berlin Heidelberg, p.4 (2012).
[2] B. Denker and E. Shklovsky (Eds), *Handbook of Solid-State Lasers*, Woodhead Publishing (2013).
[3] K. Scholle, P. Fuhrberg, P. Koopmann, and S. Lamrini, "2 μm Laser Sources and Their Possible Applications," in B. Pal (Ed.), "Frontiers in Guided Wave Optics and Optoelectronics," Ch. 21, INTECH Open Access Publisher, Rijeka (2010).
[4] S. Ishii, K. Mizutaani, T. Itabe, T. Aoki, Y. Ohno, H. Horie, T. Shimabukuro, A. Sato, and K. Asai, "Development of 2 μm airborne coherent Doppler lidar at NICT," Proc. SPIE 6409, Lidar Remote Sensing for Environmental Monitoring VII, 64090J (2006).

[5] S. Ishii, M. Koyama, P. Baron, H. Iwai, K. Mizutani, T. Itabe, A. Sato, and K. Asai, "Ground-based integrated path coherent differential absorption lidar measurement of CO_2: Foothill target return," Atmos. Meas. Tech. 6, 1359-1369 (2013).
[6] G. J. Koch, J. Y. Beyon, B. W. Barnes, M. Petros, J. Yu, F. Amzajerdian, M. J. Kavaya, and U. N. Singh "High-energy 2 μm Doppler lidar for wind measurements," Opt. Eng. 46, 116201-116214 (2007).
[7] F. Gibert, D. Edouart, C. Cénac, and F. Le Mounier, "2-μm high-power multiple-frequency single-mode Q-switched Ho:YLF laser for DIAL application," Appl. Phys. B 116, 967-976 (2014).
[8] T. Bach, T. Herrmann, C. Cellarius, and A. J. Gross, "Bladder neck incision using a 70 W 2 micron continuous wave laser (RevoLix)," World J. Urol. 25, 263 (2007).
[9] N. Bloembergen, "Role of Cracks, Pores, and Absorbing Inclusions on Laser Induced Damage Threshold at Surfaces of Transparent Dielectrics," Appl. Opt. 12, 661-664 (1973).
[10] V. A. Akimov, V. Kozlovsky, Y. V. Korostelin, A. I. Landman, Y. Podmar'kov, Y. K Skasyrskii, and M. Frolov, "Efficient pulsed $Cr(^{2+})$: CdSe laser continuously tunable in the spectral range from 2.26 to 3.61," Quantum Electronics 38, 205-208 (2008).
[11] E. Lippert, H. Fonnum, G. Arisholm, and K. Stenersen, "A 22-watt mid-infrared optical parametric oscillator with V-shaped 3-mirror ring resonator," Opt. Express 18, 26475-26483 (2010).
[12] N. Leindecker, A. Marandi, R. L. Byer, K. L. Vodopyanov, J. Jiang, I. Hartl, M. Fermann and P. G. Schunemann, "Octave-spanning ultrafast OPO with 2.6-6.1 μm instantaneous bandwidth pumped by femtosecond Tm-fiber laser," Opt. Express 20, 7046-7053 (2012).
[13] W. Wu, X.g Li, R. Yan, Y. Zhou, Y.i Ma, R. Fan, Z. Dong, and D. Chen, "100 kHz, 3.1 ns, 1.89 J cavity-dumped burst-mode Nd:YAG MOPA laser," Opt. Express 25, 26875-26884 (2017).
[14] K. Yang, Y. Yang, J. He, and S. Zhao, *Q-Switched 2 Micron Solid-State Lasers and Their Applications* [online first], IntechOpen, (2019).
[15] H. Fonnum, E. Lippert, and M. W. Haakestad, "550 mJ Q-switched cryogenic Ho:YLF oscillator pumped with a 100 W Tm:fiber laser," Opt. Lett. 38, 1884-1886 (2013).
[16] S. Ma, D. Lu, H. Yu, H. Zhang, X. Han, Q. Lu, C. Ma, J. Wang, "Langasite electro-optic Q-switched 2μm laser with high repetition rates and reduced driven voltages," Opt. Commun. 447, 13-17 (2019).
[17] X. M. Duan, Y.J. Shen, B.Q. Yao, Y.Z. Wang, "A 106W Q-switched Ho:YAG laser with single crystal," Optik 169, 224-227 (2018).
[18] J. K. Jabczynski, L. Gorajek, W. Zendzian, J. Kwiatkowski, H. Jelinkova, J. Sulc, and Nemec, "High repetition rate, high peak power, diode pumped Tm:YLF laser," Laser Phys. Lett. 6, 109-112 (2009).
[19] J. Kwiatkowski, J. K. Jabczynski, and W. Zendzian, "High repetition rate, Q-switched Ho:YAG laser resonantly pumped by a 20 W linearly polarized Tm:fiber laser,"Appl. Phys. B 114, 395-399 (2014).
[20] V. Jambunathan, *Infrared lasers based on $Ho^{3+}KRE(WO_4)_2$ crystals with Tm^{3+} or Yb^{3+} as sensitizers*, doctoral dissertation, Universitat Rovira i Virgili, Tarragona, Spain (2011).
[21] I. T. Sorokina and L. Konstantin, *Solid-State Mid-Infrared Laser Sources*, in I. T. Sorokina, and K. L. Vodopyanov (Eds.), Series: *Topics in applied physics*, Springer-Verlag Berlin Heidelberg (2003).
[22] J. A. Caird, L. DeShazer and J. Nella, "Characteristics of room-temperature 2.3-μm laser emission from Tm^{3+}in YAG and $YAlO_3$," in IEEE J. Quant. Electron. 11, 874-881 (1975).
[23] D. C. Brown, S. Tornegard, J. Kolis, C. McMillen, C. Moore, L. Sanjeewa, and C. Hancock, "The Application of Cryogenic Laser Physics to the Development of High Average Power Ultra-Short Pulse Lasers," Appl. Sci. 6, (2016).
[24] C. Kraenkel, "Rare-Earth-Doped Sesquioxides for Diode-Pumped High-Power Lasers in the 1-, 2-, and 3-μm Spectral Range," in IEEE J. Sel. Top. Quant. 21, 250-262 (2015).
[25] R. Peters, C. Kränkel, S. T. Fredrich-Thornton, K. Beil, K. Petermann, G. Huber, O. H. Heckl, C. R. E. Baer, J. C. Saraceno, T. Südmeyer, and U. Keller, "Thermal analysis and efficient high power continuous-wave and mode-locked thin disk laser operation of Yb-doped sesquioxides," Appl. Phys. B 102, 509—514 (2011).
[26] A. A. Lagatsky, O. L. Antipov and W. Sibbett, "Broadly tunable femtosecond Tm:Lu_2O_3 ceramic laser operating around 2070 nm," Opt. Express 20, 19349-19354 (2012).
[27] J. Sanghera, W. Kim, G. Villalobos, B. Shaw, C. Baker, J. Frantz, B. Sadowski, and I. Aggarwal, "Ceramic Laser Materials," Materials 5, 258-277 (2012).
[28] A. Pirri, G. Toci, B. Patrizi, and M. Vannini, "An Overview on Yb-Doped Transparent Polycrystalline Sesequioxide Laser Ceramics," in IEEE J. Sel. Top. Quant. 24, 160218 (2018).
[29] A. Ikesue, Y. L. Aung, T. Kamimura, S. Honda, and Y. Iwamoto, "Composite Laser Ceramics by Advanced Bonding Technology," Materials 11, 271 (2018).
[30] Konoshima Chemical Co., Ltd., URL: http://www.konoshima.co.jp/eng/ceramics/feature.html

[31] A. A. Lagatsky, P. Koopmann, P. Fuhrberg, G. Huber, C. T. A. Brown, and W. Sibbett, "Passively mode locked femtosecond Tm:Sc_2O_3 laser at 2.1 μm," Opt. Lett. 37, 437-439 (2012).
[32] X. Xu, Z. Hu, D. Li, P. Liu, J. Zhang, B. Xu, and J. Xu, "First laser oscillation of diode-pumped Tm^{3+}-doped $LuScO_3$ mixed sesquioxide ceramic," Opt. Express 25, 15322-15329 (2017).
[33] O. L. Antipov, A. A. Novikov, N. G. Zakharov, and A. P. Zinoviev, "Optical properties and efficient laser oscillation at 2066 nm of novel Tm:Lu_2O_3 ceramics," Opt. Mater. Express 2, 183-189 (2012).
[34] P. A. Ryabochkina, A. N. Chabushkin, Y. L. Kopylov, V. V. Balashov, and K. V. Lopukhin, "Two-micron lasing on diode-pumped Y_2O_3: Tm ceramics," Quantum Electronics, vol.46, no.7, 597 – 600 (2016).
[35] H. Wang, H. Huang, P. Liu, L. Jin, D. Shen, J. Zhang, and D. Tang, "Diode-pumped continuous-wave and Q-switched Tm:Y_2O_3 ceramic laser around 2050 nm," Opt. Mater. Express 7, 296-303 (2017).
[36] J. Szela, K. A. Sloyan, T. L. Parsonage, J. I. Mackenzie, and R. W. Eason, "Laser operation of a Tm:Y_2O_3 planar waveguide," Opt. Express 21, 12460-12468 (2013).
[37] H. Huang, H. Wang and D. Shen, "VBG-locked continuous-wave and passively Q-switched Tm:Y_2O_3 ceramic laser at 2.1 μm," Opt. Mater. Express 7, 3147-3154 (2017).
[38] T. Y. Fan, D. J. Ripin, R. L. Aggarwal, J. R. Ochoa., C. Bien, M. Tilleman, and J. Spitzberg, "Cryogenic Yb^{3+}-Doped Solid-State Lasers," IEEE J. Sel. Top. Quant. 13, 448–459 (2007).
[39] D. Brown, S. Tornegård, and J. Kolis, "Cryogenic nanosecond and picosecond high average and peak power (HAPP) pump lasers for ultrafast applications," High Power Laser Sci. 4, E15 (2016).
[40] Z. Hubka, J. Sulc, H. Jelinkova, K. Nejezchleb, and V. Skoda, "Cryogenic Tm:YAP microchip laser," Proc. SPIE 9893, Laser Sources and Applications III, 98930Q (2016).
[41] M. Divoky, S. Tokita, S. Hwang, T. Kawashima, H. Kan, A. Lucianetti, T. Mocek, and J. Kawanaka "1-J operation of monolithic composite ceramics with Yb:YAG thin layers: multi-TRAM at 10-Hz repetition rate and prospects for 100-Hz operation," Opt. Lett. 40, 855-858 (2015).
[42] K. Ertel, S. Banerjee, P. D. Mason, P. J. Phillips, C. Hernandez-Gomez and J. L. Collier, "The DiPOLE project: Towards high energy, high repetition rate diode pumped lasers," Conf. L. Electro-Opt. P. R. (CLEOPR), Kyoto, 1-2 (2013).
[43] M. De Vido, P. D. Mason, K. Ertel, J. Phillips, S. Banerjee, J. Smith, T. Butcher, M. Divoky, J. Pilar, M. Hanus, A. Lucianetti, C. Hernandez-Gomez, C. Edwards, T. Mocek, and J. Collier, "The first kilowatt average power 100J-level DPSSL," IEEE H. P. D. L. Sys. Conf. (HPD), Coventry, 19-20 (2017).
[44] J. Yu, A. Braud, and M. Petros, "600 mJ, Double-pulsed 2-micron laser," Opt. Lett. 28, 540 (2003).
[45] S. Chen, J. Yu, M. Petros, Y. Bai, U. N. Singh, M. J. Kavaya, "Joule-level double-pulsed Ho:Tm:LuLF Master-Oscillator-Power-Amplifier (MOPA) for potential spaceborne lidar applications," Proc. SPIE 5653, Lidar Remote Sensing for Industry and Environmental Monitoring V, (2005).
[46] A. Dergachev, D. Armstrong, A. Smith, T. Drake, and M. Dubois, "3.4-μm ZGP RISTRA nanosecond optical parametric oscillator pumped by a 2.05-μm Ho:YLF MOPA system," Opt. Express 15, 14404-14413 (2007).
[47] J. Liu, Q. Wang, and P. Wang, "High average power picosecond pulse generation from a thulium-doped all-fiber MOPA system," Opt. Express 20, 22442-22447 (2012).

Chapter 2

Material characterization of Tm:Y_2O_3 transparent ceramics

In this chapter, studies on the material characterization of the active medium, 3 and 5 at.% Tm:Y_2O_3 transparent ceramics, are presented, which include scanning electron microscopy for determining the quality, X-ray diffraction for determining the structure and Raman spectroscopy measurements for determining the phonon energy. This chapter is devoted to have a better understanding of the transparent ceramics studied in this work from the view of material science. The experiments were carried out in the laboratories of the Physics and Cristallography of Matericals and Nanomaterials group (FiCMA – FiCNA), Rovira i Virgili University, Tarragona, Spain and Institute of Science and Technology for Ceramics (ISTEC-CNR), Faenza, Italy.

2.1. Methods and data analysis

2.1.1 Scanning Electron Microscopy (SEM)

For transparent laser ceramic samples, the surface microstructural study is one of the most important characterizations to understand the ceramic quality and to improve the ceramic fabrication process. Due to the grain size of ceramics, which is usually at the micron or even sub-micron level, an advanced measurement technique is required. Therefore, SEM measurements are introduced due to many advantages.

Firstly, the images produced by SEM have high spatial resolution and contain massive topography and compositional information of the surface. This is because of the wide range of signals generated by scanning the sample surface using a focused electron beam. The gathered signal includes secondary electrons (SE), reflected or back-scattered electrons (BSE), characteristic X-rays and light (cathode luminescence) (CL), absorbed current (specimen current) and transmitted electrons resulted from the interactions of the electron beam with atoms at various depths within the sample [1]. Secondly, SEM measurements have high analytical capability. With the attached Energy Dispersive Spectrometer and Electron Backscatter Diffractometer, qualitative or semi-quantitative analysis on the chemical composition, crystalline structure, and crystal orientations can be done via SEM. In addition, SEM measurements require minimal sample preparation and are easy to operate.

In this work, the SEM images were measured by a Zeiss Sigma FE-SEM 300 (as shown in Figure 2-1), which gathered enough signal by detecting SE BSE. The polished surfaces of 3 and 5 at.% Tm:Y_2O_3 transparent ceramic samples were scanned. Both samples have 3 mm in thickness and 10 mm in diameter. This equipment was provided by the Institute of Science and Technology for Ceramics (ISTEC-CNR), Faenza, Italy.

Figure 2-1 Zeiss Sigma FE-SEM 300 used in this work for the surface characterization of the Tm:Y_2O_3 transparent ceramic samples.

2.1.2 X-Ray Diffraction (XRD)

The XRD characterization can provide information about the crystalline structure and unit cell parameters of the transparent ceramic samples. Thus, the structural properties of the poly-crystalline transparent ceramics can be compared and confirmed with their single-crystalline counterparts.

In the XRD measurement, the characteristic atomic structure of the sample is obtained from the XRD spectrum, which is generated based on the constructive interference and Bragg's Law. In the measurement, an X-ray beam generated by an X-ray tube is shot into the probe at an angle Θ, and gets scattered by the material lattice. The diffraction occurs when the scattered light interferes constructively with the scattered rays from other atomic planes, resulting in a peak intensity in the XRD spectrum, which follows the Bragg's law:

$$2dsin\Theta = \lambda_0, \tag{2.1}$$

where λ_0 is the wavelength of the incident X-ray beam (λ_0 = 1.54051 Å for CuKα_1 line here), d is the inter-planar spacing distance in the sample lattice and 2Θ is the angle between the

incident ray and the diffracted beam [2,3]. Because each material has a set of unique *d*-spacing's, the corresponding (*hkl*)-indices can be achieved by comparison of *d*-spacing's with standard reference patterns. For the cubic Y_2O_3 crystal, the JCPDS card no. 25-1011 was referenced in this work. Furthermore, the lattice constant *a* of the isotropic ceramic sample can be obtained by the relation:

$$d = \frac{a}{\sqrt{h^2+k^2+l^2}}. \tag{2.2}$$

Combining equation (2.1) and (2.2), the lattice constant *a* can be calculated by:

$$a = \frac{\lambda_0}{2sin\Theta} \cdot \sqrt{h^2 + k^2 + l^2}. \tag{2.3}$$

Figure 2-2 Siemens D-500 diffractometer used in this work for the structural characterization of the Tm:Y_2O_3 transparent ceramic samples.

In this work, the XRD measurements were carried out at room temperature using a Siemens D-500 diffractometer (as shown in Figure 2-2). The X-ray intensity versus 2Θ was measured from 5˚ to 70˚ with 0.05˚ step. This equipment was provided by the *Servei de Recursos Científics i Tècnics* of the Rovira i Virgili University, Tarragona, Spain.

2.1.3 Raman spectroscopy

Raman spectroscopy is a practical technique for chemical analysis providing the important

information of the probe sample, such as the vibrational modes of the different chemical bonds, the maximum phonon energy, crystal structure or degree of crystallinity, etc.

The mechanism of Raman spectroscopy is based on Raman scattering, which is the inelastic scattering of a photon with low frequency mode, i.e., phonon in the crystal lattice in the case of solid-state materials. The measured Raman spectrum shows the intensity of the scattered photons versus the frequency difference (measured in wavenumbers with unit cm^{-1}) to the incident photons. Peaks only appear in the Raman spectrum if vibrational modes in the system are sensitive to the laser wavelength used (514 nm provided by an Ar^+-ion laser here) [4,5].

Figure 2-3 Renishaw in Via confocal Raman microscope used in this work for the vibrational characterization of the Tm:Y_2O_3 transparent ceramic samples

In this work, the Raman spectrum of the samples was measured using a Renishaw in Via confocal Raman microscope (as shown in Figure 2-3) placed at the *Servei de Recursos Científics i Tècnics* of the Rovira i Virgili University, Tarragona, Spain.

2.2. Experimental results

2.2.1 SEM characterization

To understand the grain size and grain growth of the transparent ceramic samples, SEM images were measured on the polished surface of two ceramic samples, as shown in Figure 2-4. In (a) we show the SEM image of the 3 at.% sample, while in (b), the one for the 5 at.%

sample. From the two images, one can see that the grains and grain boundaries of both samples are clean and free from pores or impurities on the microscopic scale (micron meters). High homogeneity of the ceramic grain growth can be observed. The grain size of both samples is approximately 1μm. It should be noted that different grey scales can be observed in most of the grains in both images. The spots with different grey scale can be intragranular Tm_2O_3 particles or incomplete-grown grains. Even though, the uniformity of the Tm ion distribution in the macroscopic scale was still confirmed by the element mapping measurement.

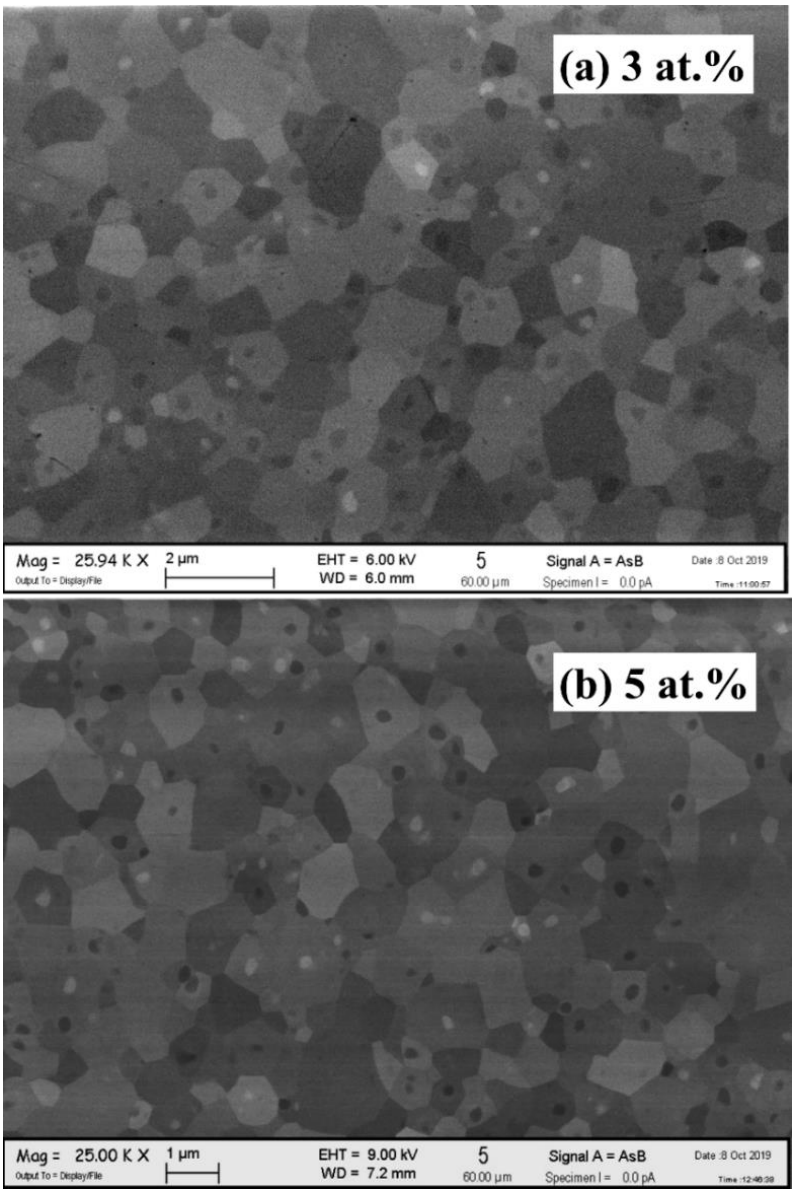

Figure 2-4 The SEM microstructure of (a) 3 and (b) 5 at.% Tm:Y_2O_3 transparent ceramic samples, measured from the polished surface.

2.2.2 XRD characterization

XRD patterns for both 3 and 5 at.% Tm:Y_2O_3 were measured, as shown in Figure 2-5. The X-ray intensity versus 2Θ was measured from 5˚ to 70˚ in a step of 0.05˚. The measured peaks of both ceramics are labeled with (*hkl*)-indices, which agree with the JCPDS card no. 25-1011 of the cubic Y_2O_3 crystal. In this aspect, the ceramic samples maintain well the cubic crystallinity of Y_2O_3. In addition, the patterns show no additional peaks or peak shifts due to Tm dopant concentration variation, indicating that the structure is not affected by the introduction of Tm ions into Y_2O_3.

Based on the (*hkl*)-indices and the Bragg's law, the lattice constant of the Tm:Y_2O_3 transparent ceramic samples was estimated. As shown in Table 2-1, the lattice constant amounts to ~ 10.61(1) Å, which agrees with the literature value in [6].

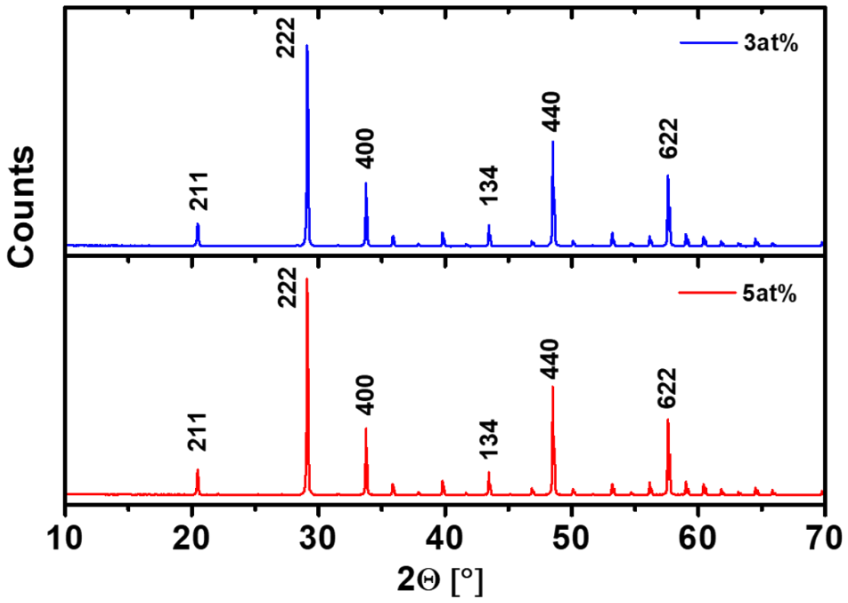

Figure 2-5 XRD patterns of the 3 and 5 at.% Tm:Y_2O_3 transparent ceramic samples. (*hkl*)-indices: JCPDS card no. 25-1011 of the cubic Y_2O_3.

Table 2-1 Crystal parameters of Tm:Y_2O_3 transparent ceramic

(*hkl*)	2Θ [°]	*d* [Å]	*a* [Å]
211	20.5	4.33	10.60
222	3.75	3.06	10.62
400	33.75	2.65	10.61
134	43.45	2.08	10.61
440	48.5	1.87	10.61
622	57.6	1.60	10.60

2.2.3 Raman characterization

Figure 2-6 shows the Raman spectra measured for both 3 and 5 at.% Tm:Y_2O_3 transparent ceramic samples in a resolution of 1.2 cm^{-1}. The excitation of the samples is by means of an Ar^+-ion laser at 514 nm. For both samples, the maximum phonon energy is estimated at 592 cm^{-1}, which is close to the literature value of 597 cm^{-1} [6]. The maximum intensity peak locates at 377 cm^{-1}, which comes from the Fg mode lattice vibration of O or Y ions [7]. The crystallinity is confirmed for the ceramic samples by the Raman spectroscopy because the appearance of clear and intense peaks and the absence of bands typical for glassy materials.

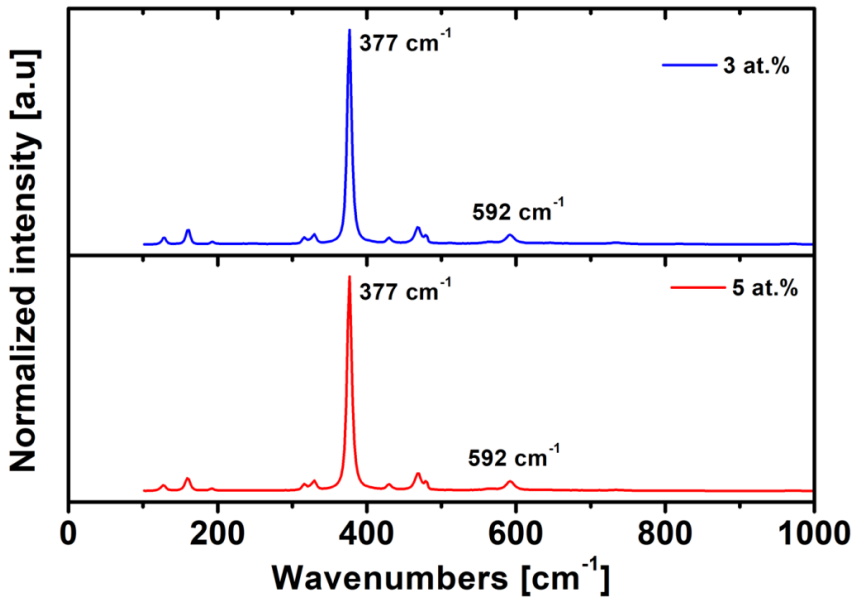

Figure 2-6 Raman spectra of the 3 and 5 at.% Tm:Y_2O_3 ceramic samples.

2.3. Summary

In this chapter, the active media, 3 and 5 at.% Tm:Y_2O_3 transparent ceramics were characterized by the measurement of SEM, XRD and Raman spectroscopy. In all such characterizations, the transparent ceramic samples exhibit the same properties as their crystalline counterparts, indicating that there is no limitation to consider them as an alternative.

2.4. References

[1] Manfred von Ardenne, "Das Elektronen-Rastermikroskop," Z. Physik 109, 553–572 (1938).
[2] B.D. Cullity, Elements of X Ray Diffraction (2nd ed.), Reading, Massachusetts: Addison-Wesley Publishing Company, ISBN 0-534-55396-6, (1978).

[3] W.H. Bragg and W.L.Bragg, "The Reflexion of X-rays by Crystals," Proc. R. Soc. Lond. A. 88, 428–438 (1913).
[4] JoVE Science Education Database, *Analytical Chemistry*, Raman Spectroscopy for Chemical Analysis, JoVE, Cambridge, MA, (2019).
[5] R.L. McCreery, *Raman Spectroscopy for Chemical Analysis*, in: Chemical Analysis: A Series of Monographs on Analytical Chemistry and Its Applications, John Wiley & Sons, ISBN 0471231878, (2005).
[6] C. Kraenkel, "Rare-Earth-Doped Sesquioxides for Diode-Pumped High-Power Lasers in the 1-, 2-, and 3-μm Spectral Range," in IEEE J. Sel. Top. Quant. 21, 250-262, (2015).
[7] N.J. Shivaramu, B.N. Lakshminarasappa, K.R. Nagabhushana, and F. Singh, "Synthesis characterization and luminescence studies of gamma irradiated nanocrystalline yttrium oxide," Spectrochimica Acta Part A: Molecular and Biomolecular Spectroscopy 154, 220–231 (2016).

Chapter 3

Spectroscopic characterization of Tm:Y_2O_3 transparent ceramics

In this chapter, spectroscopic characterizations on the active medium, Tm:Y_2O_3 transparent ceramics, are presented, which include optical transmission/absorption, emission and fluorescence lifetime measurements. The purposes of these characterizations are to acquire better understanding of the spectroscopic properties and to get information on crucial laser design parameters, which will be employed in the further laser operations. The optical transmission and emission spectra measurements were done in FiCMA - FiCNA laboratories, Rovira i Virgili University, Tarragona, Spain. The fluorescence lifetime was measured at HiLASE Centre, Institute of Physics of the Czech Academy of Sciences, Prague, Czech Republic.

3.1. Methodology and data processing

3.1.1 Optical transmission measurement

The optical transmission of Tm:Y_2O_3 transparent ceramics was measured using Cary 5000 UV-Vis-NIR (as shown in Figure 3-1) spectrophotometer covering various manifolds of the Tm ion. The optical transmission at room temperature was firstly measured for the 650 – 2100 nm range in a data interval of 1 nm for both 3 and 5 at.% samples. Then, each manifold was measured with higher resolution at various temperatures (details are found in the following paragraphs). The measured room temperature whole range spectra were compared with the Fresnel loss determined theoretical transmission between two sample surfaces, which was calculated using the equation:

$$Trans(\lambda) = (1 - FL)^2 \frac{1}{1-FL^2}, \tag{3.1}$$

where $Trans(\lambda)$ is the theoretical transmission and FL is the Fresnel loss. The Fresnel loss can be calculated from the wavelength dependent refractive index n of Tm:Y_2O_3 using:

$$FL = \left(\frac{n-1}{n+1}\right)^2. \tag{3.2}$$

According to the database of refractive index in [1], the refractive index of Y_2O_3 can be calculated by:

$$n^2 = 1 + \frac{2.578\lambda^2}{\lambda^2-0.1387^2} + \frac{3.935\lambda^2}{\lambda^2-22.936^2}, \tag{3.3}$$

where λ is the wavelength of transmitted light in the unit of [μm].

In the cryogenic spectra measurements, a data interval of 0.05 nm was used for the wavelength range of 650 – 720 nm and 750 – 840 nm, corresponding to the $^3H_6 \rightarrow {}^3F_{2,3}$ and $^3H_6 \rightarrow {}^3H_4$ transitions, respectively. So that, the narrow spectral lines at cryogenic temperatures can be resolved. In the wavelength range of 1100 – 1300 nm and 1500 – 2100 nm, the data interval used was set to 0.5 nm, corresponding to the $^3H_6 \rightarrow {}^3H_5$ and $^3H_6 \rightarrow {}^3F_4$ transition, respectively. Among these transmission bands, the 750 – 840 nm and 1500 – 2100 nm bands are laser relevant. The former one corresponds to the laser absorption wavelength range, while the latter one covers the Tm fluorescence emission around 2 μm.

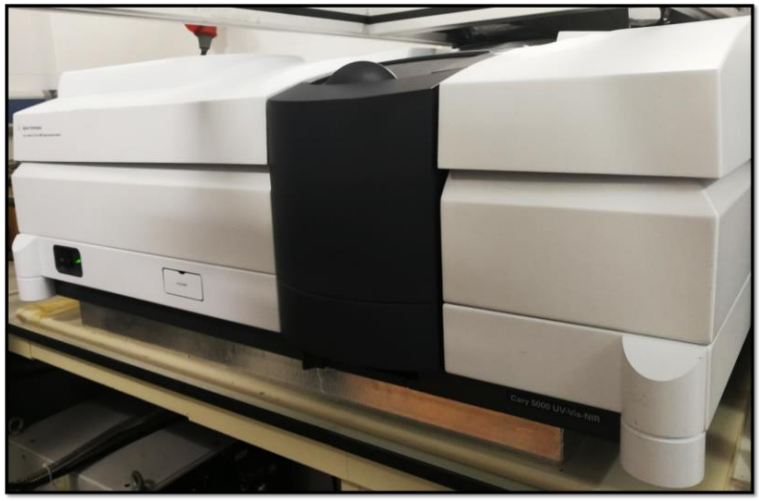

Figure 3-1 Cary 5000UV-Vis-NIRspectrophotometer.

To achieve the cryogenic temperatures from 6 K to 300 K in step size of 20 K, the sample was fixed in a vacuum chamber using an aluminum holder (Figure 3-2 (a)) and cooled by a Leybold helium closed cycle cryostat (Figure 3-2 (c)). Inside the vacuum chamber, a vacuum below 10^{-5} mbar was maintained to avoid condensation on the sample surfaces. The sample temperature and the vacuum pressure were controlled by the control panel in Figure 3-2 (b). In addition, the sample was placed at normal incidence direction to the transmitted light of the spectrometer to minimize reflection loss.

3.1.2 Emission spectra measurement

The emission spectra were measured using the 3 at.% Tm:Y_2O_3 transparent ceramic sample, also in the full temperature range from 6 K – 300 K in step size of 20 K and in the spectra range from 1550 – 2200 nm in a resolution of 0.5 nm. To achieve the cryogenic temperatures, the same cryogenic cooling system from the optical transmission measurements was used in this experiment. The sample in the vacuum chamber was excited by a fiber coupled (core diameter 200 μm, N.A. = 0.22) laser diode (LD) from BWT Beijing LTD (as shown in Figure 3-3). The radiation from LD was un-polarized light centered at 793 nm ($\Delta\lambda \sim 3$nm), which was focused by a set of lenses (L1 and L2, f = 100 mm) onto the sample surface at a tip, so that the reabsorption can be minimized. The fluorescence emission from the sample was collected by lenses L3 and L4 (f = 100 mm) and then coupled by a fiber (core diameter 600 μm, N.A. = 0.39) to the optical spectrum analyzer (AQ6375B, YOKOGAWA), as shown in

Figure 3-4 (a). The schematic setup is illustrated in Figure 3-4 (b).

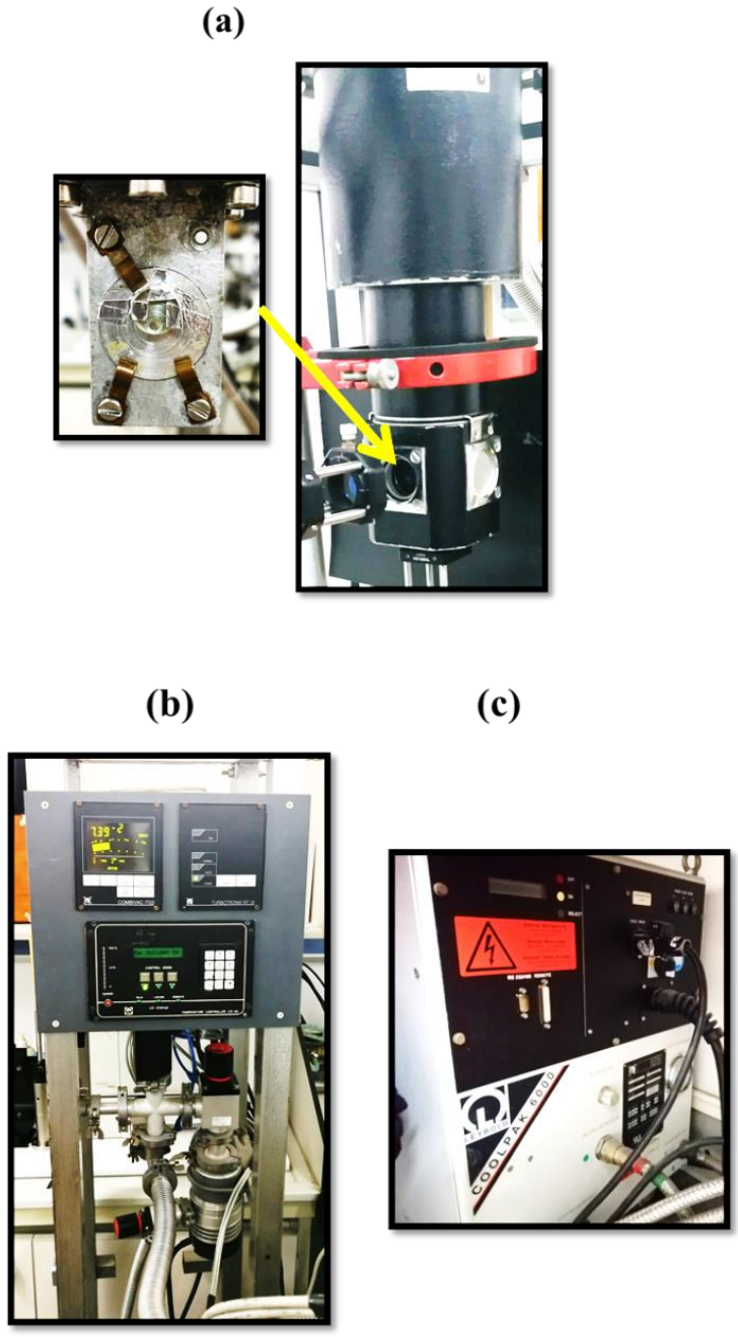

Figure 3-2 Experimental setup for cryogenic transmission spectra measurement: (a) vacuum chamber and the sample holder inside (one sample mounted), (b) vacuum and temperature control panel, (c) Leybold helium closed cycle cryostat.

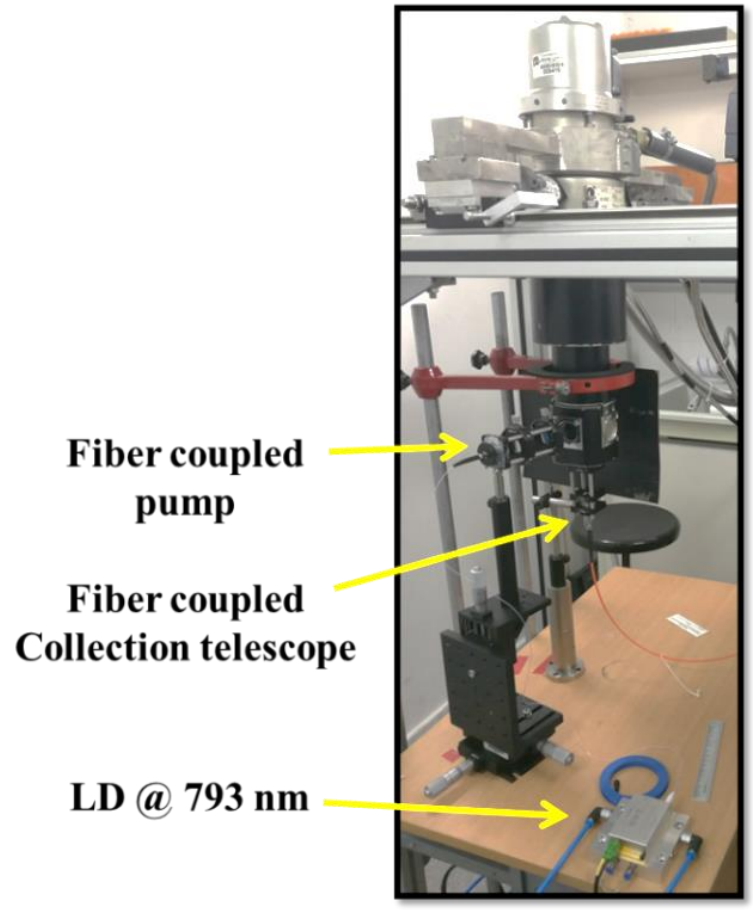

Figure 3-3 Experimental setup for emission measurement with laser diode (LD), vacuum chamber and set of lenses.

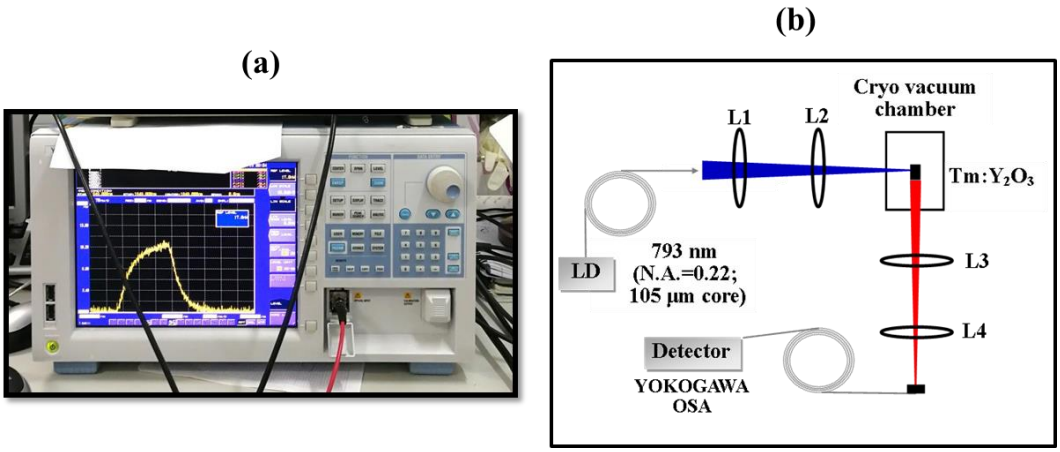

Figure 3-4 (a) YOKOGAWA optical spectrum analyzer, (b) schematic setup illustration with lenses of f = 100 mm (L1 – L4).

3.1.3 Fluorescence lifetime of laser upper level $^3F_4$

For the temperature-dependent lifetime measurement, both 3 and 5 at.% samples were

employed. The experimental setup and devices employed are shown in Figure 3-5. As shown in the figure, the sample was pumped by the tight focused pulsed LD (the same one from the emission measurement) at an angle, so that the excited volume of the sample was limited to a minimal size and the effect of reabsorption was reduced [2]. The pump pulse duration and repetition rate were controlled by a digital delay generator (DG645, Stanford research systems) and were set as 10 ms and 20 Hz (20 % duty cycle). To detect the radiation from the $^3F_4$ level of Tm ions, a PbS detector (PDA30G-EC, Thorlabs) was employed, to which a long pass filter cutting at 1000 nm was used, so that the pump radiation was blocked. The detected fluorescence signal was then collected and averaged by a digital oscilloscope (WaveSurfer 64MXs-B, Teledyne LeCroy). To obtain the value of the fluorescence lifetime, an exponential function as shown in eq. (3.4) was fitted to the measured data, in which τ is the fitted lifetime value of the $^3F_4$ level.

$$I = I_0 + Aexp(-\frac{t-t_0}{\tau}), \tag{3.4}$$

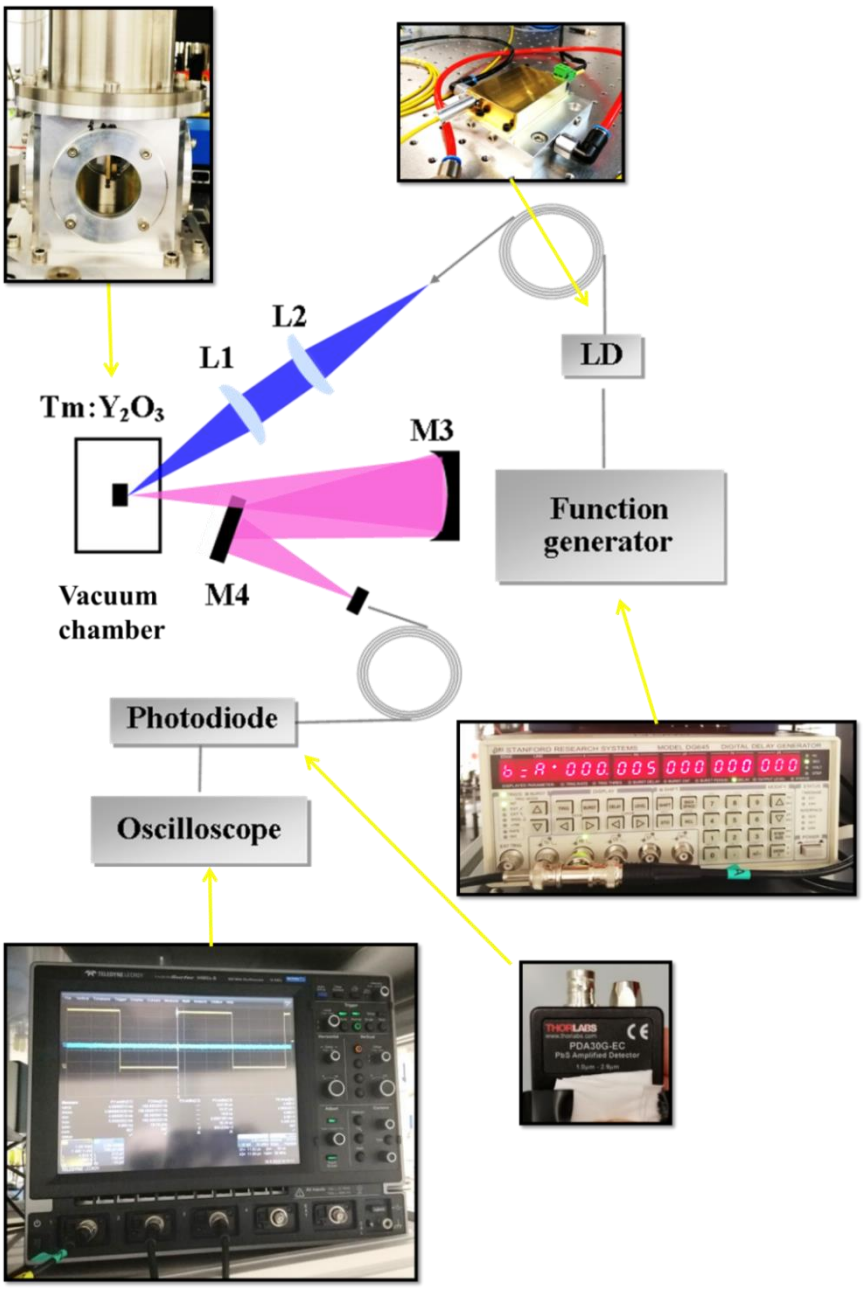

Figure 3-5 Setup of the fluorescence lifetime measurement for the $^3F_4$ energy level of Tm ion.

3.1.4 Absorption cross-section calculation

Based on the obtained transmission spectra, absorption cross-sections were calculated using the Lambert Beer's law [3]:

$$I = I_0 \exp(-\alpha d), \tag{3.5}$$

where α is the absorption coefficient of Tm:Y_2O_3, d = 0.3 cm is the sample thickness. The ratio $\frac{I}{I_0}$ between I and I_0 equals the measured transmission $T(\lambda)$. Combined with the relation

between absorption coefficient and absorption cross-section:

$$\alpha(\lambda) = \sigma_{abs}(\lambda) * N_{dop} * d, \tag{3.6}$$

the absorption cross-section can be written as:

$$\sigma_{abs}(\lambda) = \frac{\log(T(\lambda)) * \ln(10)}{N_{dop} * d}, \tag{3.7}$$

where N_{dop} is the ion number of the doped rare earth ion Tm. For the 3 at.% sample, it was calculated as 7.96×10^{20} cm^{-3} using the equation:

$$N_{dop} = \frac{2\rho}{(2*88.9+3*16.0)*1.6726\times10^{-24}g} * 0.03, \tag{3.8}$$

where ρ = 5.04 g/cm^3 is the mass density of the host material Y_2O_3 [4].

3.1.5 Emission cross-section calculation

To obtain the emission cross-sections, two spectroscopic methods can be used. One is the Füchtbauer-Ladenburg (FL) method [5] and the other is the McCumber (MC) method (reciprocity method) [6]. In this work, the emission cross-section of Tm:Y_2O_3 was estimated by combining both methods [2].

- *Füchtbauer-Ladenburg method*

In the FL method, the emission cross-section is calculated based on the equation:

$$\sigma_{emi}(\lambda) = \frac{\lambda^4}{8\pi c n^2 \tau_r} \frac{I(\lambda)}{\int I(\lambda) d\lambda}, \tag{3.9}$$

$$c = 3 \times 10^8\ m/s, \qquad n = 1.888, \qquad \tau_r = 3.5\ ms$$

where c is light velocity; n is refractive index of Tm:Y_2O_3 [7]; τ_r is the radiative lifetime [8] and $\frac{I(\lambda)}{\int I(\lambda) d\lambda}$ is the normalized line shape function. $I(\lambda)$ is the wavelength dependent fluorescence intensity in the measured emission spectra. In this work, a fixed value of n = 1.888 (@1931 nm) was applied in the whole emission wavelength range of 1550 – 2200 nm, because the deviation of n amounts to only 0.007 (0.4%)..

- *McCumber method*

In the MC method, the emission cross-section is calculated using

$$\sigma_{emi}(\lambda) = \sigma_{abs}(\lambda) \frac{Z_l}{Z_u} \exp[\frac{E_{zpl} - \frac{hc}{\lambda}}{kT}], \tag{3.10}$$

which is derived from the definition of Einstein coefficient [8]. In (3.10), $\frac{Z_l}{Z_u}$ is the thermal steady-state ratio between lower and upper laser level populations, which can be estimated from the splitting energy of the lower and upper laser levels ($^3H_6$ and $^3F_4$, respectively). A comparison with the measured values will be presented later in 3.2.3. In addition, E_{zpl} is the "zero-phonon-line" energy, which can be estimated by using the equation:

$$E_{zpl} = \frac{hc}{\lambda_{zpl}}, \tag{3.11}$$

k and h are the Boltzmann and Planck's constants; T is the temperature. All parameters for emission cross-section calculation are shown in Table 3-1.

Table 3-1 Data used for calculation of emission cross-sections with the reciprocity and FL methods

	Tm:Y_2O_3	Reference
$^3H_6$ level splitting [cm $^{-1}$]	0,31,89,219,230,340,382,436,488,692,788,797	[9]
$^3F_4$ level splitting [cm $^{-1}$]	5615,5674,5780,6005,6018,6114,6144,6189	[9]
λ_{zpl} [nm] – zero phonon line	1781	[9]
Z_l/Z_u	1.31 (80 K), 1.39 (160 K), 1.46 (240 K), 1.48 (280 K)	
τ [ms] – radiative lifetime	3.5	[1]
n – Refractive index @ 1931 nm	1.888	[7]
k [m^2kg/s^2K]	1.38×10^{-23}	[10]
h [m^2kg/s]	6.626×10^{-34}	[10]

3.1.6 Gain cross-section calculation

Based on the data of absorption and emission cross-sections, gain cross-sections can be calculated using to the equation:

$$\sigma_{gain} = \beta\sigma_{emi} - (1-\beta)\sigma_{abs}, \tag{3.12}$$

where β is the inversion ratio of the laser. Information about the active media's laser potential can be obtained from the gain spectra, such as the temperature or cavity loss dependent lasing wavelength selection, the small-signal gain coefficient g_0, etc.

3.2. Experimental results

3.2.1 Optical transmission spectra at room temperature

Figure 3-6 shows the photograph of the two Tm:Y_2O_3 transparent ceramics employed in this

work, which have the diameter of 10 mm and a thickness of 3 mm. The left one is 3 at.% and the right one is 5 at.%. Both samples are acquired from and polished to laser quality by *Konoshima Chemical Co. Ltd.* (flatness ~ λ/10). From the figure, one can see that both samples have high transparency and exhibit no color inhomogeneity or difference between each other.

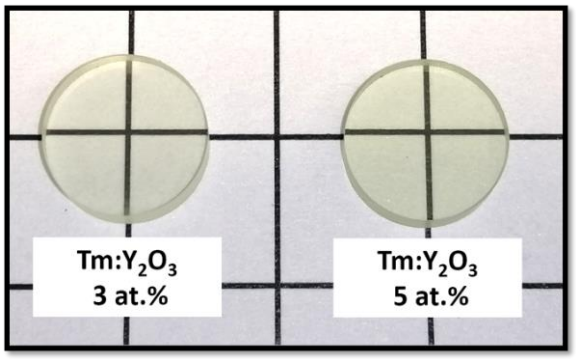

Figure 3-6 Photograph of the 3 (left) and 5 (right) at.% Tm:Y_2O_3 ceramic with thickness of 3 mm and diameter of 10 mm.

The optical transmission in the visible and infrared regions of both ceramic samples is presented in Figure 3-7, which ranges from 600 to 2100 nm measured with data interval of 1 nm. Different transition bands of Tm^{3+} are labeled as $^3F_{2,3}$, $^3H_4$, $^3H_5$ and $^3F_4$, corresponding to the absorption around 680, 800, 1200, and 1630 nm, respectively.

The green curves show the wavelength dependent theoretical transmission determined by the Fresnel loss, which amounts to ~ 17.2 % at 2.1 μm. As shown in the figure, the measured data agree well with the theoretical values, indicating the high optical quality of the transparent ceramic samples. In both samples, enough absorption can be estimated.

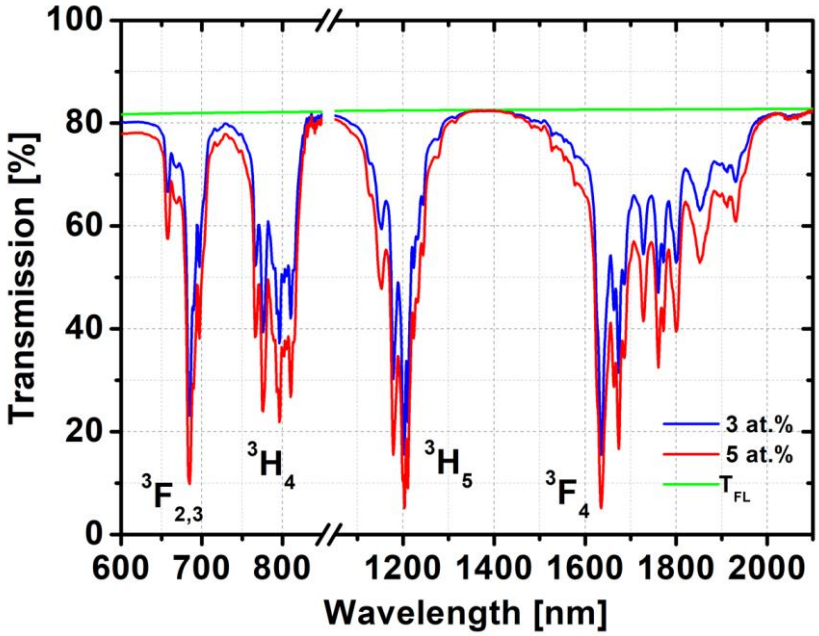

Figure 3-7 Red and blue curves: transmission spectra at room temperature of the 3 and 5 at.%Tm:Y_2O_3 ceramic sample (thickness of 3 mm). Green curves: theoretical transmission based on Fresnel loss.

3.2.2 Absorption cross-section

Figure 3-8 shows the absorption cross-section spectra of Tm:Y_2O_3 from 6 K to 300 K in the laser relevant wavelength ranges of 750 – 840 nm and 1500 – 2100 nm, corresponding to the $^3H_6 \rightarrow {}^3H_4$ (pump) and $^3H_6 \rightarrow {}^3F_4$ (laser) transitions, respectively. Figure 3-8 (a) shows the absorption cross-section of the 750 – 840 nm band, which matches the emission wavelength of the diode pump source. In this region, near room temperature (300 K), the highest absorption cross-section of 3.9×10^{-21} cm^{-2} is found at 796.6 nm with full width at half maximum (FWHM) of 1.7 nm, while at 6 K the maximum value of 18.1×10^{-21} cm^{-2} is found at 775.8 nm with FWHM of 0.8 nm. Figure 3-8 (b) shows the absorption cross-section in the 1500 – 2100 nm band, which is the reverse transition of the Tm^{3+} fluorescence around 2 μm. At 300 K, the highest absorption cross-section in this wavelength range is estimated to be 7.0×10^{-21} cm^{-2} at 1634.9 nm, while at 6 K it is 14.1×10^{-21} at 1635.7 nm. The measured absorption spectra at room temperature agree well with the literature spectra in [7].

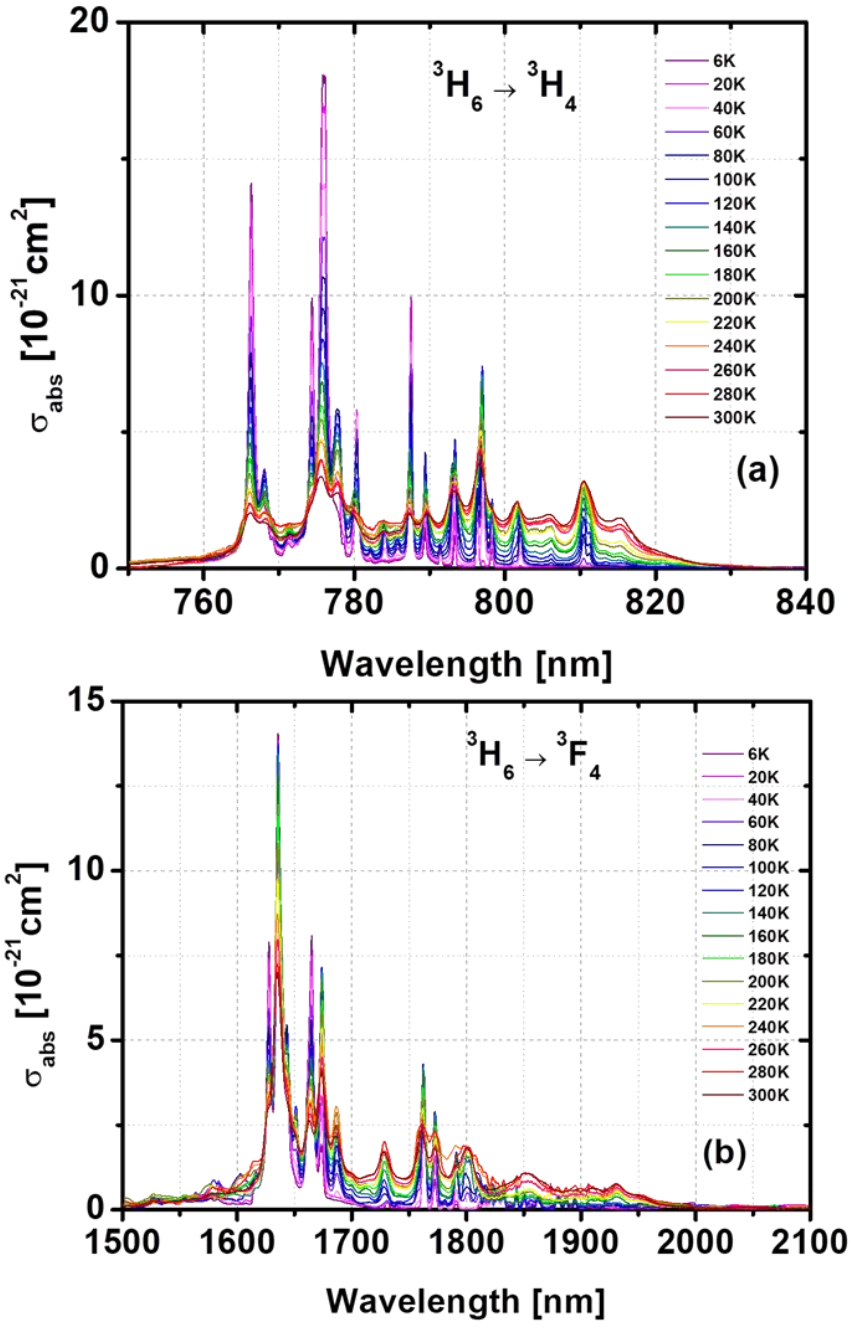

Figure 3-8 Absorption cross-sections in the laser relevant bands: (a) 750 – 850 nm, (b) 1500 – 2100 nm.

When we study the absorption peak values and absorption bandwidths in Figure 3-8 clear temperature dependence can be observed, which can be explained by two mechanisms. One is the thermal narrowing effect of the lineshape at lower temperatures. According to the lineshape function,

$$g(\upsilon) = \left(\frac{\Delta\upsilon}{2\pi}\right)\left[(\upsilon - \upsilon_0)^2 + \left(\frac{\Delta\upsilon}{2}\right)^2\right]^{-1}, \tag{3.13}$$

the absorption peak value $g(\nu_0) = \frac{2}{\pi * \Delta\nu}$ increases when the bandwidth $\Delta\nu$ narrows at lower temperatures [11], which explains the change of the peaks at 766, 774, 776, 780, 787.5 nm in Figure 3-8 (a) and the peaks at 1628, 1636, 1665 nm in Figure 3-8 (b). The other mechanism is the depopulation of degenerated Stark splitting and elimination of vibronic (electron–phonon interaction) peaks, which results in the decrease of peak values even the absence of peaks at lower temperature. For the peaks such as 784, 810.5, 1728 nm and peaks > 1800 nm, both the peak value and bandwidth decrease with the decrease of temperature. Other peaks exhibit the maximum peak value neither at 6 K nor 300 K, because those peaks consist of multiple lines and the population fraction of each line changes with temperature.

The maximum peak values and relevant temperatures are listed in Table 3-2 for all peaks from 750 to 840 nm. In this aspect, one can see from the table that the most interesting absorption peak for the cryogenic laser operations can be the one at 793.4 nm. This wavelength matches well with the emission wavelength of the pump source AlGaAs laser diode, and the maximum absorption cross-section at 793.4 nm is obtained at 80 K, near liquid nitrogen temperature, which is suitable for cryogenic operation.

Table 3-2 Maximum peak values and relevant temperatures of absorption cross-section in the wavelength range of 750 – 840 nm

λ_o[nm]	766.3	768.0	774.4	775.8	776.1	777.8	780.3	783.9
$\sigma_{abs,\,max}$ [10^{-21} cm^{-2}]	14.1	3.7	9.9	18.1	18.1	5.9	5.8	1.8
T [K]	6	60	6	6	6	80	6	300
λ_o[nm]	787.5	789.4	793.4	797.0	798.3	801.6	810.5	
$\sigma_{abs,\,max}$ [10^{-21} cm^{-2}]	9.9	4.3	4.7	7.4	2.5	2.5	3.2	
T [K]	6	80	80	120	100	240	300	

For the cryogenic laser operation, near liquid nitrogen temperature (80 K) is of great interest as mentioned above. At 80 K, the maximum absorption cross-section is obtained at 775.9 nm with FWHM of 0.8 nm as shown in Figure 3-8, which amounts to 10.7×10^{-21} cm^{-2}. Although several absorption peaks are available for pumping at 80 K, the most interesting ones are those at 793 nm and 797 nm because of their relatively large absorption cross-sections, broad band, and the possibility to be excited by the commercially available high power AlGaAs laser diodes. These two peaks are enlarged in Figure 3-9. From the figure, one can see that at 80 K, the central wavelength of the absorption cross-section peak around 793

nm shows almost no shift compared to that at 300 K, while a red shift of 0.5 nm can be observed for the peak around 797 nm.

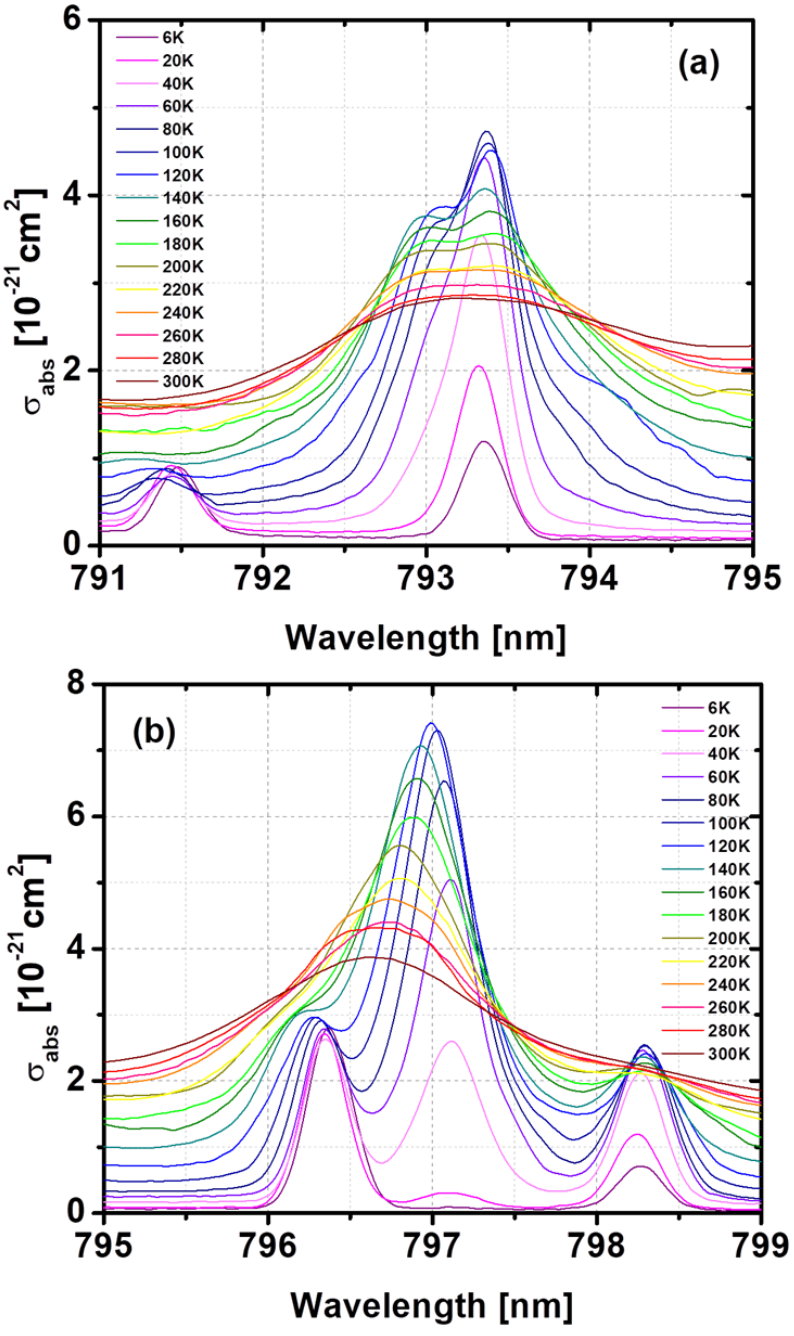

Figure 3-9 Enlarged absorption peaks at (a) 793 nm and (b) 797 nm.

A summary of the peak values and FWHM are plotted in Figure 3-10 as function of temperature. As shown in the graph, the maximum absorption cross-section around 793 nm is obtained at 80 K, which amounts to 4.7×10^{-21} cm^{-2}, ~ 1.7 times the value at 300 K. The FWHM narrows down to 0.64 nm from 2.60 nm. For the peak around 797 nm, the maximum

absorption cross-section of 7.5×10^{-21} cm^{-2} is found at 120 K, 1.7 times the value at 300 K. The FWHM is 0.6 nm at 80 K, while 1.8 nm at 300 K.

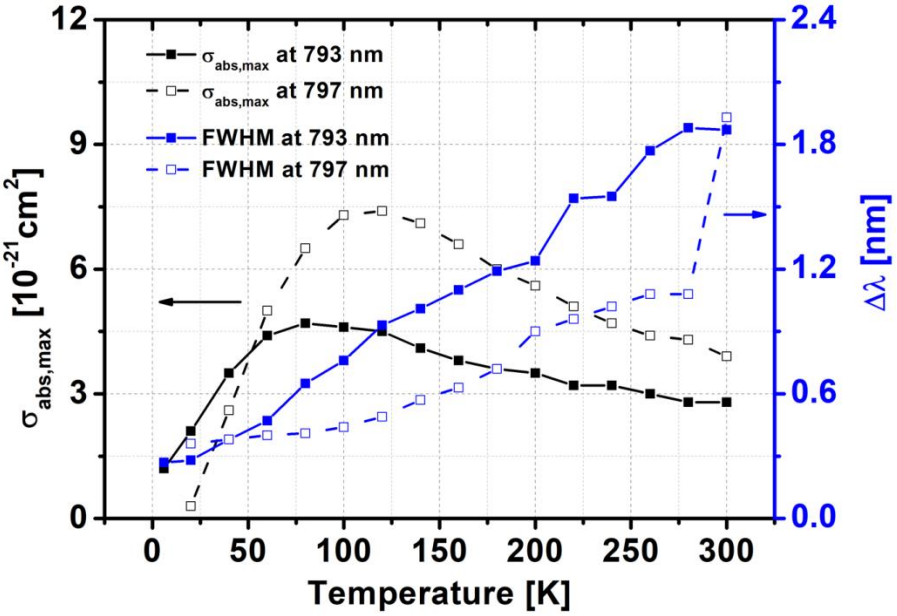

Figure 3-10 Peak values (black) and FWHM (blue) of the absorption cross-section peaks around 793 and 797 nm, plotted as a function of temperature.

The absorption cross-sections of $^3H_6 \rightarrow {}^3F_{2,3}$ and $^3H_6 \rightarrow {}^3H_5$ transitions are also measured, which are shown in Figure 3-11 (a) and (b), ranging from 650 – 720 nm and 1100 – 1300 nm, respectively. The temperature dependence of the peak value and bandwidth is as clear as the other two manifolds shown in Figure 3-8 . The maximum absorption cross-section in the 650 – 720 nm range is centered at 686.1 nm and found at 6 K with a value of 26.6×10^{-21} cm^{-2}, which is 3.7 times of the value at 300 K. In the 1100 – 1300 nm region, a maximum of 26.2×10^{-21} cm^{-2} is observed at 1180.2 nm at 6 K, more than 6 times the value at 300 K.

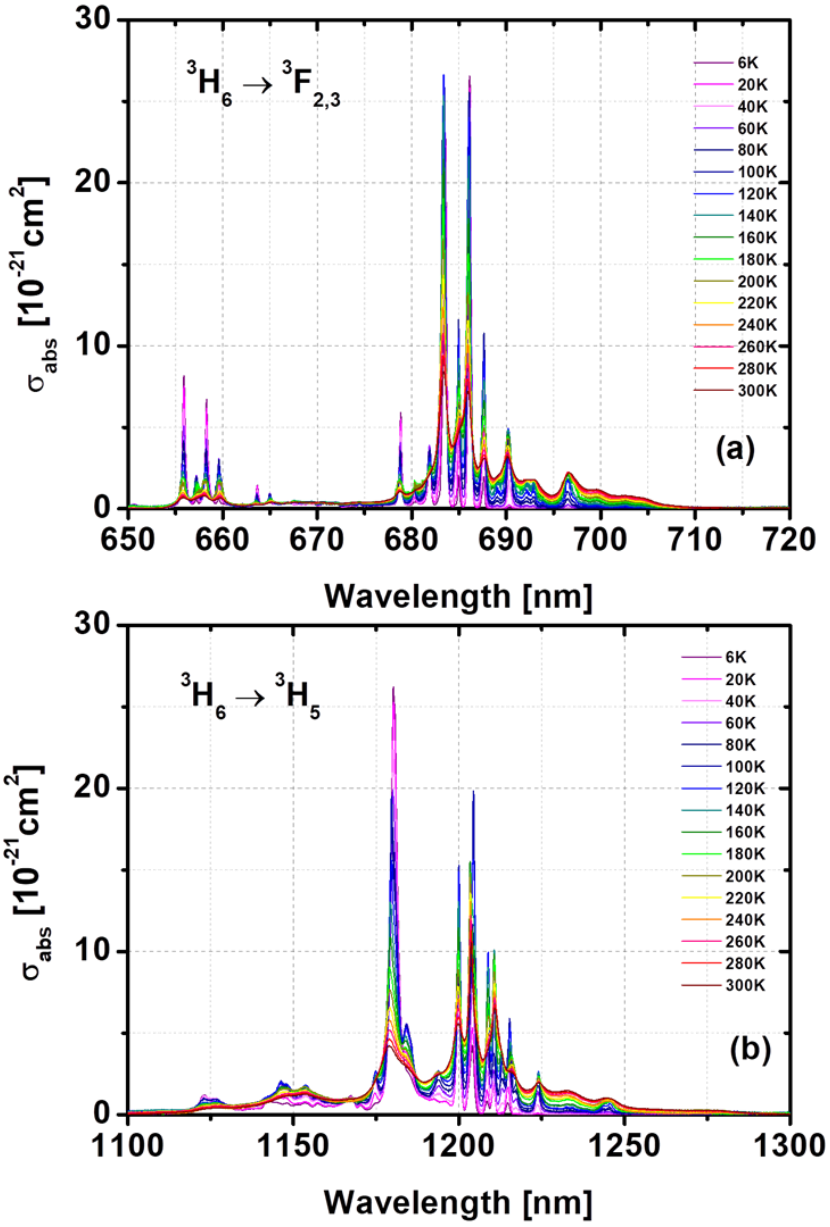

Figure 3-11 Absorption cross-sections in the wavelength ranges: (a) 650 – 750 nm, (b) 1100 – 1400 nm.

3.2.3 Stark splitting of the $^3H_6$ and $^3F_4$ energy levels

To determine the Stark splitting of the laser relevant energy levels $^3H_6$ and $^3F_4$, the optical absorption and emission at 6 K are employed. We plotted the absorption and emission spectra for the transitions between the energy level $^3H_6$ and $^3F_4$ in wavenumbers, as shown in Figure 3-12. The energy level splitting is list in Table 3-3. The Stark energy level splitting for Tm:Y_2O_3 single crystal has been reported in the literature [10], being comparable with the

data we achieved for the transparent ceramic sample. Two splitting values of $^3H_6$ (marked as * in Table 3-3) were missing in the measurements, because only $^3H_6 \leftrightarrow {}^3F_4$ transitions were included. Other $^3H_6$ relevant transitions were not employed here.

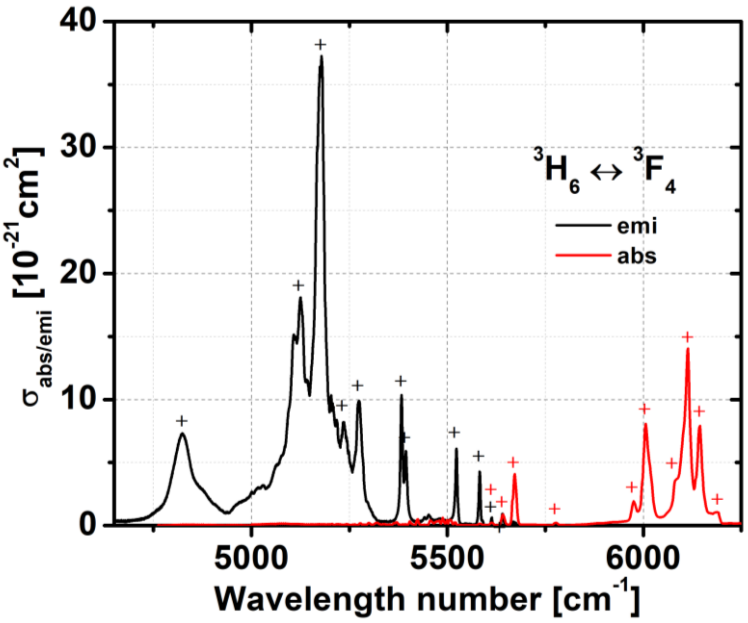

Figure 3-12 Low temperature (6 K) optical absorption and emission between energy levels $^3H_6$ and $^3F_4$.

Table 3-3 Stark splitting of energy levels $^3H_6$ and $^3F_4$ in comparison with literature data

$^{2S+1}L_J$	Energy [cm^{-1}] This work	Energy [cm^{-1}] From [9]	$^{2S+1}L_J$	Energy [cm^{-1}] This work	Energy [cm^{-1}] From [9]
$^3H_6$	0	0	$^3F_4$	5613	5615
	30	31		5674	5674
	90	89		5777	5780
	219	219		6006	6005
	230	230		6081	6018
	339	340		6113	6114
	378	382		6191	6189
	435.5	436			
	488	488			
	*	692			
	789	788			
	*	797			

3.2.4 Emission cross-section

The emission cross-section of Tm:Y_2O_3 was calculated by combining the FL and MC methods. A comparison of these two methods is shown in Figure 3-13, where two emission cross-section curves of 300 K are shown as examples. From the figure one can see that the

peak central wavelengths estimated using both methods match well with each other in the full emission wavelength range from 1500 – 2100 nm. The peak intensity of these two curves merges in the wavelength range around 1880 – 1940 nm. In the shorter wavelength range (1500 – 1880 nm), better peak information is obtained using the MC method, where the absorption cross section measurements have higher accuracy [2]. However, in the longer wavelength range > 1960 nm, the emission cross-section calculated by the MC method is not accurate any more due to the high noise in the absorption cross section spectra, which was strongly amplified by the calculation, as the blue curve shown in Figure 3-13. In contrast, FL-method obtains better accuracy in this range, where the reabsorption was carefully avoided during measurements, as the black curve shown in Figure 3-13 [2]. Accordingly, the emission cross-sections of Tm:Y_2O_3 were estimated in the way that the MC method was used in the shorter wavelength range till 1940 nm and the FL method was employed in the longer wavelength range.

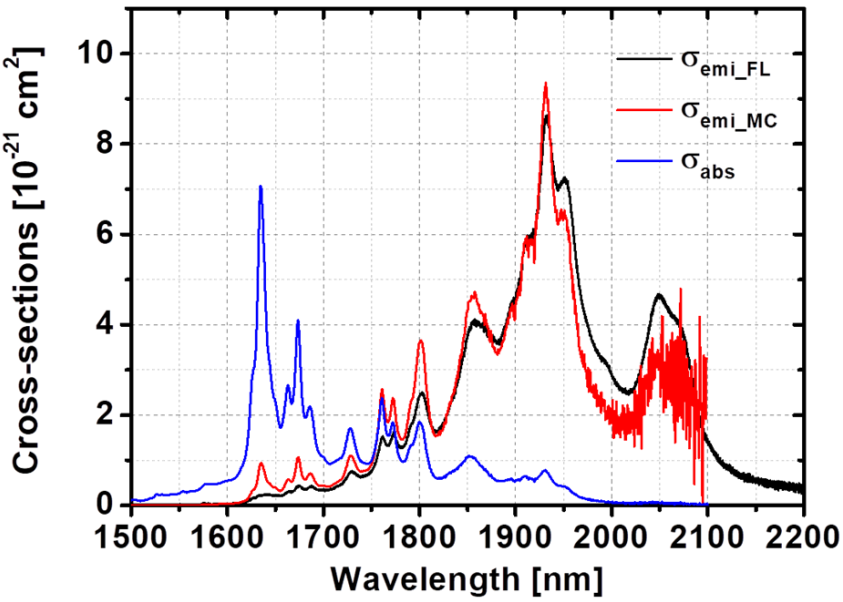

Figure 3-13 Comparison between emission cross-sections calculated by the FL (black) and MC (red) methods at 300 K. The blue curve is the corresponding absorption cross-section.

As shown in Figure 3-14 , the emission cross-section of Tm:Y_2O_3 from 1550 – 2200 nm, corresponding to the $^3F_4 \rightarrow {}^3H_6$ transition, is presented from 6 K to 300 K in step size of 20 K. From the figure, one can see that no temperature-dependent wavelength shift is observed at the maximum emission cross-sections, which locate around 1932 nm irrespective to the

sample temperature. At 300 K, the highest cross-section is 10.4×10^{-21} cm^{-2}, while at 6 K the highest cross-section amounts to 37.3×10^{-21} cm^{-2}, around 4 times the value at 300 K. The emission band of Tm:Y_2O_3 is around 450 nm broad at 300 K, which ranges from 1700 – 2150 nm. At 6 K, the effective emission band is still ~ 280 nm broad, ranging from 1870 – 2150 nm. Near the liquid nitrogen temperature (80 K), the maximum emission cross-section is calculated to be 30.3×10^{-21} cm^{-2}, locating at ~ 1932 nm. The emission band at 80 K ranges from 1870 – 2150 nm, still 280 nm broad, which is favorable in some laser operations, such as mode-locking. In sum, Tm:Y_2O_3, as an active medium, shows high laser potential together with a broad emission band at 80 K, which will be beneficial for the further cryogenic laser operation.

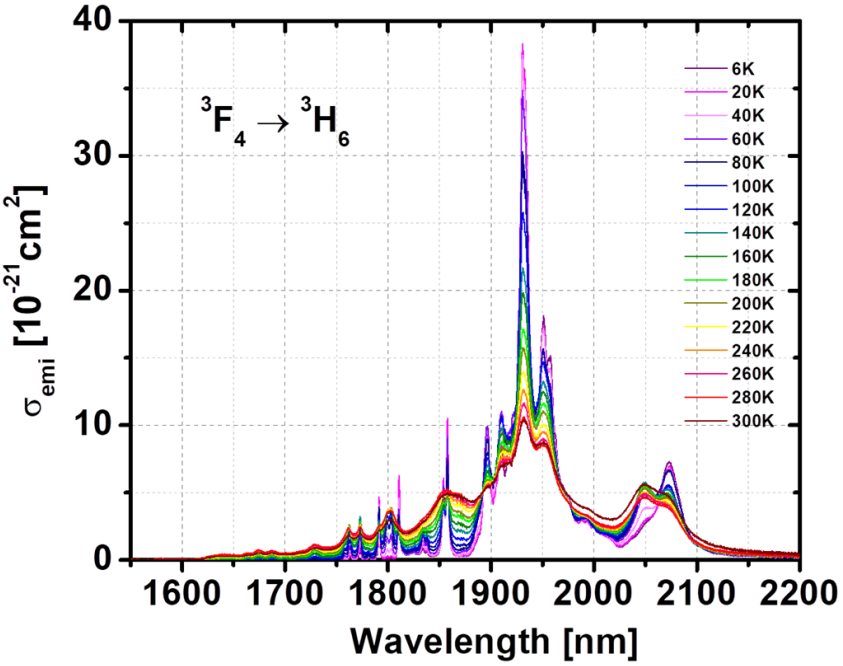

Figure 3-14 Emission cross-section for $^3F_4 \rightarrow {}^3H_6$ transition from 1500 – 2200 nm, calculated by combining FL and MC methods at various temperatures.

3.2.5 Gain cross-section

In this section, the gain cross-sections of Tm:Y_2O_3 were estimated in two ways: with fixed population inversion ratio β but various sample temperatures or with fixed sample temperature but various β values.

Figure 3-15 shows the estimated gain cross-sections for various temperatures with fixed population ratio of $\beta = 0.1$. From the figure, one can infer that the gain cross-section increases with the decrease of temperature for a given β value. The highest gain peak is centered at ~ 1932 nm for temperatures lower than 240 K, while the maximum gain at 300 K shifts to longer wavelength at ~ 2050 nm. The peak value and wavelength of the maximum gain are summarized in Table 3-4 for $\beta = 0.1$.

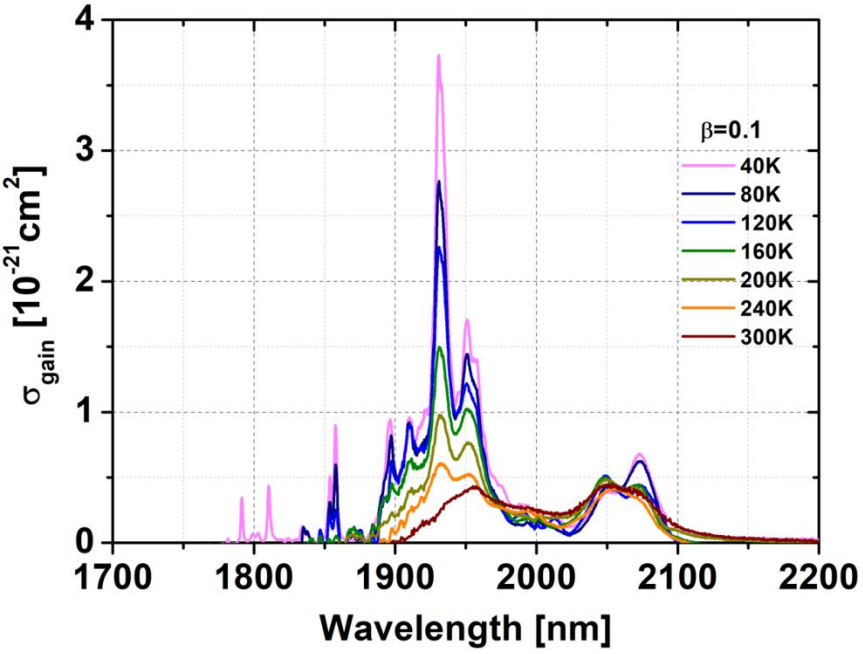

Figure 3-15 Gain cross-sections at various temperatures for $\beta = 0.1$.

Table 3-4 Peak value and relevant wavelength of the maximum gain at various temperatures with $\beta = 0.1$

T [K]	40	80	120	160	200	240	300
λ_o [nm]	1931	1931	1931	1931.5	1932	1932.5	2050
$\sigma_{gain,\ max}$ [10^{-21} cm^{-2}]	3.7	2.8	2.2	1.5	1.0	0.6	0.45

In Figure 3-16, the gain cross-sections at 80 and 300 K are estimated by varying the β value from 0.1 to 0.5. As shown in Figure 3-16 (a), the maximum gain cross-section at 80 K always locates at ~ 1932 nm irrespective to the change of β value, indicating that the lasing wavelength of Tm:Y_2O_3 will be always at ~ 1932 nm at 80 K irrespective to the loss of the laser cavity. However, as shown in Figure 3-16 (b), the gain cross-section spectra at 300 K differ with the gain spectra at 80 K in the structure. At 300 K the gain peak around 2050 nm is

comparable to the peak around 1930 nm, especially for small β's, while at 80 K the gain peak around 1932 nm dominates in the spectra. Hence, at room temperature, it is possible to achieve lasing at longer wavelength (> 2000 nm) for the Tm:Y_2O_3 laser, while at cryogenic temperature, only laser around 1932 nm can be achieved. The maximum gain cross-section and the corresponding wavelength are plotted as a function of β in Figure 3-17.

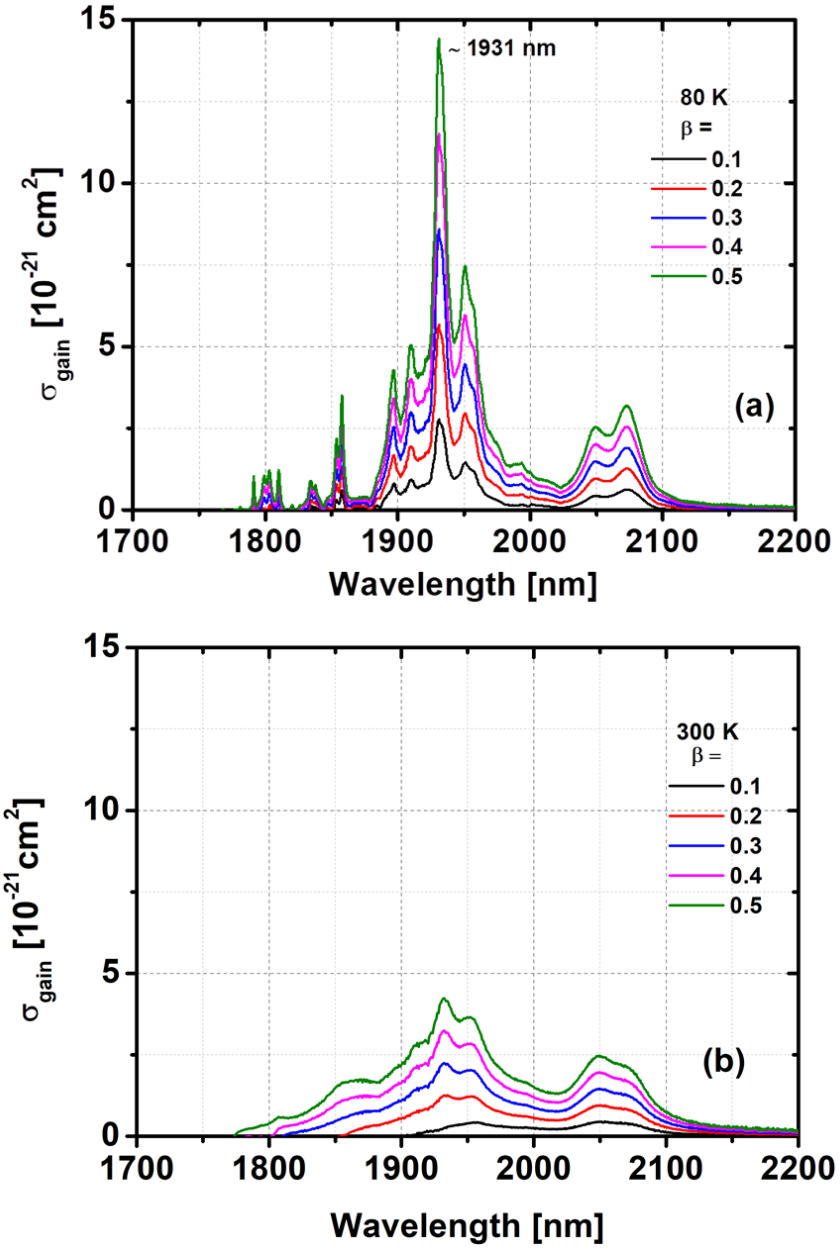

Figure 3-16 Gain cross-sections at (a) 80 and (b) 300 K, calculated using various β values.

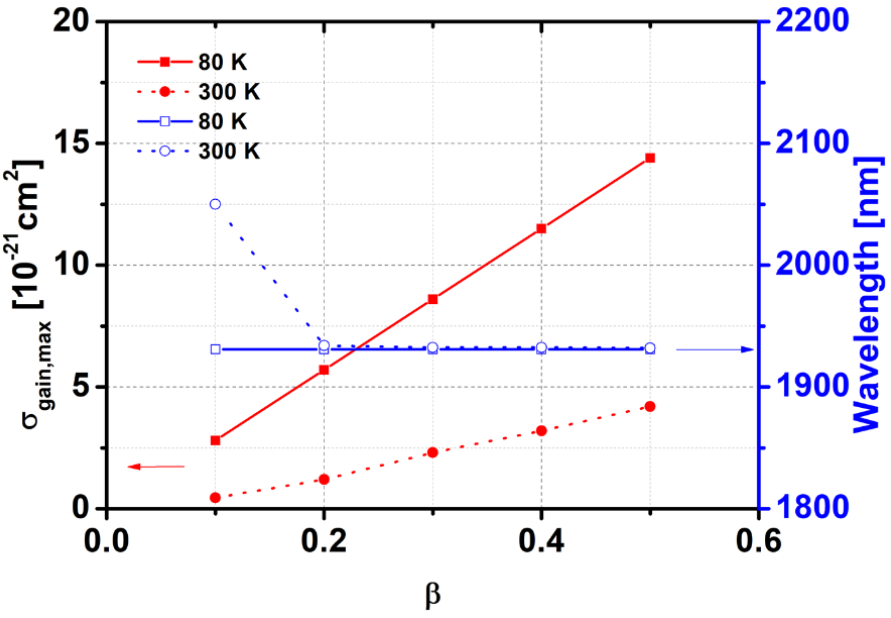

Figure 3-17 The wavelength (blue) and peak value (red) of the maximum gain cross-section at 80 (solid) and 300 K (dashed) as a function of β.

3.2.6 Fluorescence lifetime of the $^3F_4$ energy level

The temperature-dependent fluorescence lifetime of the upper laser level $^3F_4$ is presented as the dashed line in Figure 3-18 for 3 at.% Tm:Y_2O_3. As shown in the figure, the lifetime of Tm:Y_2O_3 transparent ceramics ranges from 3.1 to 3.6 ms, comparable with the literature value of 3.5 ms in [7], which was calculated using Judd-Ofelt method. A slight decrease of the lifetime is observed, when the temperature increases. This decrease can be a result from the parasitic decay process [12]. The fluorescence lifetime can be calculated as:

$$\frac{1}{\tau_f} = \frac{1}{\tau_r} + \frac{1}{\tau_p}, \tag{3.14}$$

where τ_r is the radiative lifetime and τ_p is the parasitic decay time. As a lower limit of τ_r, the measured τ_f at 6 K is used, which is 3.6 ms. With the increase of temperature, the parasitic decay contribution increases for the sample, as the solid line shown in Figure 3-18.

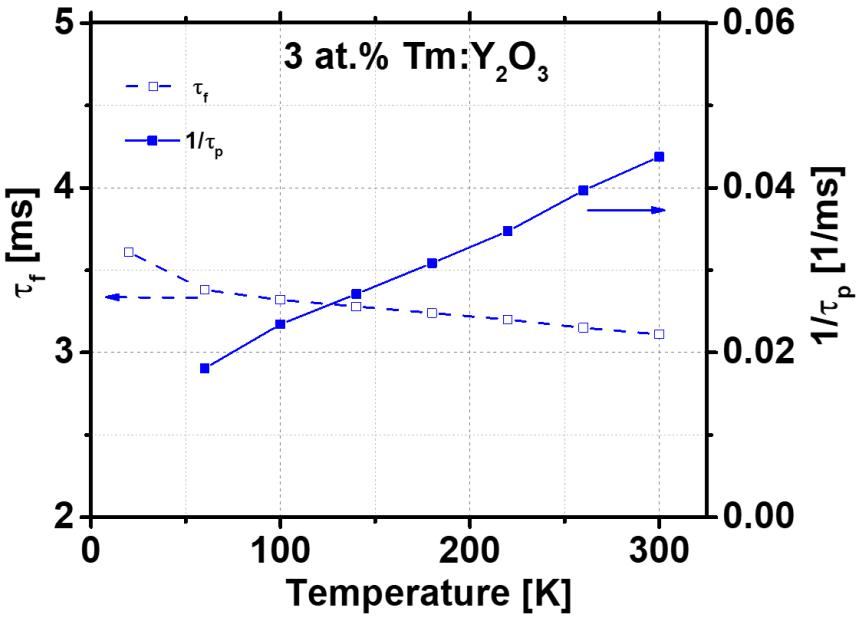

Figure 3-18 Temperature dependent luminescence lifetime/parasitic decay time (dashed/solid line) of $^3F_4$ level for 3 at.% Tm:Y_2O_3 transparent ceramic.

3.3. Summary

In this chapter, the active media, 3 and 5 at.% Tm:Y_2O_3 transparent ceramics, were characterized in terms of spectroscopy, that includes measurements of optical transmission/absorption, emission spectra and fluorescence lifetime of the upper laser level $^3F_4$. All measurements were carried out at various temperatures, from which crucial parameters such as the exact pump wavelength, absorption bandwidth, small signal gain, and amplified spontaneous emission estimation were obtained for the design of HAPP laser. In the absorption measurements, the absorption peaks around 793 and 797 nm were detailed studied, because those wavelengths match well with the emission wavelength of the diode pump source. For the 793 nm peak, the best operation temperature is 80 K, while for the 797 nm peak it is 120 K. According to the temperature-dependent emission spectra, the Tm:Y_2O_3 transparent ceramics exhibit broad emission band even at cryogenic temperatures. The highest emission cross-section was found at 1932 nm irrespective to the temperature. In addition, at 80 K, the lasing wavelength of a laser oscillator can also be expected to be at 1932 nm, according to the calculated gain cross-sections at this temperature, where the highest gain cross-section was found always at 1932 nm irrespective to the population ratio value β, i.e. the

cavity loss. The measured fluorescence lifetime shows a decrease with the increase of temperature, due to the increased influence from the parasitic decay.

3.4. References

[1] https://refractiveindex.info, last visit on 31st Dec. 2019.
[2] J. Körner, V. Jambunathan, J. Hein, R. Seifert, M. Loeser, M. Siebold, U. Schramm, P. Sikovinski, A. Lucianetti, T. Mocek and M. C. Kaluza, "Spectroscopic characterization of Yb^{3+}-doped laser materials at cryogenic temperatures," Appl. Phys. B 116, 75-81, (2014)
[3] M. Fox, *Optical Properties of Solids (2 ed.)*, Oxford University Press, p. 3-4, (2010).
[4] P. Villars (Chief Editor), *PAULING FILE in: Inorganic Solid Phases*, SpringerMaterials (online database), Springer, Heidelberg (ed.) SpringerMaterials.
[5] W. Koechner, *Solid-State Laser Engineering*, New York: Springer, p. 17, (1986).
[6] D. E. McCumber, "Einstein relations connecting broadband emission and absorption spectra," Phys. Rev. 136, A954-A957, (1964).
[7] P. Loiko, P. Koopmann, X. Mateos, J. M. Serres, V. Jambunathan, A. Lucianetti, T. Mocek, M. Aguilo, F. Diaz, U. Griebner, V. Petrov, and C. Kraenkel, "Highly Efficient, Compact Tm^{3+}:RE_2O_3 (RE = Y, Lu, Sc) Sesquioxide Lasers Based on Thermal Guiding," in IEEE J. Sel. Top. Quant. 24, 1-13, (2018).
[8] A. Einstein, "Strahlungs-Emission und -Absorption nach der Quantentheorie," Verb. Dtsch. Phys. Ges.18, 318-323 (1916).
[9] R. P. Leavitt, J. B. Gruber, N. C. Chang and C. A. Morrison, "Optical spectra, energy levels, and crystal-field analysis of tripositive rare-earth ions in Y_2O_3. II. Non-Kramers ions in C_2 sites," J. Chem. Phys. 76, (1982).
[10] Siegfried Flügge (Ed.), *Handbuch der Physik*, vol. 54, Springer, pp. 90, (1962).
[11] W. Koechner and M. Brass, *Solid state lasers : a graduate text*, Springer-Verlag New York Berlin Heidelberg, p.23, (2003).
[12] J. Körner, T. Lühder, J. Reiter, I. Uschmann, H. Marschner, V. Jambunathan, A. Lucianetti, T. Mocek, J. Hein, M. C. Kaluza, "Spectroscopic investigations of thulium doped YAG and YAP crystalsbetween 77 K and 300 K for short-wavelength infrared lasers," J. Lumin. 202, 427-437, (2018).

Chapter 4

Cryogenic $Tm:Y_2O_3$ laser characterization

In this chapter, the laser properties of $Tm:Y_2O_3$ transparent ceramic at cryogenic temperature were tested by operating the lasers in continuous-wave (CW) regime. The theoretical and experimental studies were devoted to obtain the optimal laser design parameters, such as the pump wavelength and its bandwidth, the cooling efficiency of the sample holder, the optimal output coupling transmission, the laser operation temperature, the dopant concentration of the active medium, among others. All the laser operations were carried out in the laboratory of HiLASE Centre, Institute of Physics of the Czech Academy of Sciences, Dolní Břežany, Czech Republic.

4.1. Theoretical background

According to the laser oscillator theory in [1], the laser output power P_{out} can be defined in a simple way as:

$$P_{out} = \eta_{slope}(P_{in} - P_{th}), \tag{4.1}$$

where η_{slope} is the slope efficiency and $P_{in/th}$ is the incident/threshold pump power.

For a two-mirror laser oscillator, which was used in the further CW laser operation, the parameters of eq. (4.1) can be derived from the laser steady state condition and gain saturation. In the steady state, the laser gain per pass equals the internal and external losses in the cavity. Thus, the condition for oscillation is

$$R_1 R_2 \exp(g - \alpha)\, 2d = 1, \tag{4.2}$$

where $R_{1/2}$ is the reflectivity of the cavity mirrors, g/α is the gain/absorption coefficient per unit length, and d is the length of the active medium. In an oscillator with one side high-reflective (HR) mirror and one side output coupler, R_1 equals 1 and $R_2 = 1 - T_{OC}$, where T_{OC} is the transmission of the output coupler. Other losses such as Fresnel loss and losses from other optical elements due to misalignment can be taken as small leakage δ of the HR mirror. Thus, R_1 is taken as $1 - \delta$, and the gain coefficient can be obtained from eq. (4.2) as:

$$g = \frac{1}{2d} * (L - \ln(1 - T_{OC})), \tag{4.3}$$

where L is the intra-cavity loss $2\alpha d + ln\delta$.

The gain coefficient g can also be derived from the rate equation as:

$$g = \sigma_{emi} n = \sigma_{emi} n_{tot} \left(W_p - \frac{\gamma - 1}{\tau_f}\right)\left(\gamma c \sigma_{emi} \Phi + W_p + \frac{1}{\tau_f}\right)^{-1}, \tag{4.4}$$

where n is the population inversion at steady-state, $\gamma = 1 + \frac{g_2}{g_1}$ is given by the line-shape factor $g_{1/2}$ of the upper and lower laser levels, c is the speed of light, σ_{emi} is the stimulated emission cross-section, Φ is the photon density, W_p is the pump rate and τ_f is the fluorescence lifetime of the upper laser level. The Tm laser at cryogenic temperature can be taken as a 4-level-system laser due to the depopulation of the lower laser level. Thus, γ equals 1 and $W_p \ll 1/\tau_f$. Eq. (4.4) can be re-arranged as:

$$g = \frac{\sigma_{emi} n_{tot} W_p \tau_f}{\sigma_{emi} c \Phi \tau_f + 1}, \tag{4.5}$$

and further in the form of

$$g = \frac{g_0}{1+I/I_s}, \tag{4.6}$$

where $g_0 = \sigma_{emi} n_{tot} W_p \tau_f$ is the small signal gain, $I = \Phi h \frac{c^2}{\lambda_L}$ is the power density in the system and $I_s = \frac{hc}{\sigma_{emi}\lambda_L \tau_f}$ is the saturated flux, at which the small signal gain is reduced by 1/2. λ_L is the laser wavelength. The power density *I* in the system can also be derived from eq. (4.3) and eq. (4.6**)** as:

$$I = I_s[\frac{2g_0 d}{L-\ln(1-T_{OC})} - 1]. \tag{4.7}$$

The output power derived from the circulating power of a two-mirror oscillator is

$$P_{out} = AI\frac{1-R_2}{1+R_2} \tag{4.8}$$

with effective beam area of A. Combining eq. (4.7**)** and eq. (4.8**)**, the output power is written as:

$$P_{out} = AI_s[\frac{2g_0 d}{L-\ln(1-T_{OC})} - 1] \cdot \frac{T_{OC}}{2-T_{OC}} \tag{4.9}$$

and then as:

$$P_{out} = \frac{hcA}{\sigma_{emi}\lambda_L \tau_f} \cdot \frac{T_{OC}}{(2-T_{OC})(L-\mathrm{T_{OC}})} \cdot [2g_0 d - (L-\ln(1-T_{OC}))]. \tag{4.10}$$

Compared eq. (4.10**)** with the form of eq. (4.1), the incident power P_{in} needs to be introduced by the small signal gain g_0. In eq. (4.6**)**, $g_0 = \sigma_{emi} n_{tot} W_p \tau_f$, which can be further expressed as:

$$g_0 = \frac{\sigma_{emi}\tau_f \lambda_L}{hcV}\eta_0 P_{in}, \tag{4.11}$$

where *V* is the material volume and η_0 is the intrinsic efficiency. For Tm lasers, $\eta_0 = \frac{\lambda_p}{\lambda_L}\eta_{abs}\eta_{QY}\eta_B$ is proportional to the quantum efficiency $\frac{\lambda_p}{\lambda_l}$ between pump and laser wavelength, absorption efficiency η_{abs} to the pump power, quantum yield η_{QY} of the active medium and the mode coupling efficiency η_B [2]. Re-arranging eq. (4.10**)** with eq. (4.11**)** in the form of eq. (4.1) the slope efficiency and threshold incident power are obtained:

$$\eta_{slope} = \frac{2\eta_0 T_{OC}}{(2-T_{OC})[L-\ln(1-T_{OC})]}, \tag{4.12}$$

$$P_{th} = \frac{Ahc}{2\eta_0 \sigma_{emi}\tau_f \lambda_L}[L-\ln(1-T_{OC})]. \tag{4.13}$$

4.2. Experimental setup

The experimental setup of the CW laser is illustrated in Figure 4-1. The pump part consisted of pump source and two lenses (marked as LD, L1 & L2 in the figure). As pump source, two

diode lasers (LD's) (BWT Beijing Ltd.) were used. One had broad bandwidth ($\Delta\lambda_P$ ~ 3 nm) and the other was stabilized by a Volume Bragg Grating (VBG) to a bandwidth of 0.5 nm. Both LD's emitted around 793 nm and were coupled by a fiber of core diameter of 105 µm (N.A. = 0.22). The operational temperature of the LD's was controlled by a water chiller (SMART H150-1000, LabTech), which had a tuning range from 8 to 35 ℃. The maximum output power of the broadband and VBG-stabilized lasers were 30 and 25 W, respectively. The radiation from the pump source was focused onto the active medium in 1:2 ratio by two anti-reflection (AR) coated achromatic lenses (L1 and L2, with focal lengths of 100 and 200 mm, respectively).

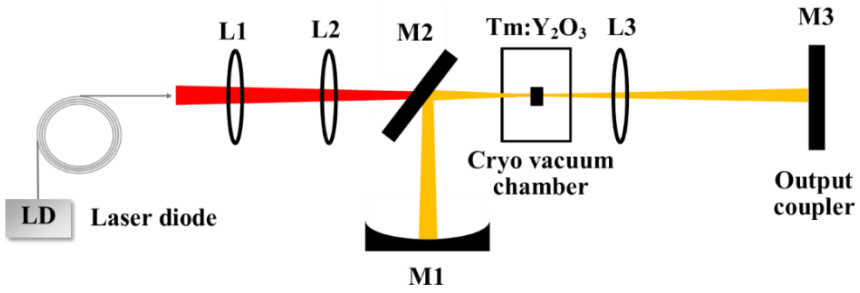

Figure 4-1 Sketch of the CW laser setup. LD – pump laser diode; L1 & L2 - achromatic lenses; M1 – plano-concave cavity mirror; M2 - dichroic mirror; L3 – plano-convex thin lens; M3 – output coupler.

In the oscillator cavity part, as active medium, uncoated transparent ceramic Tm:Y_2O_3 of 3 and 5 at.% were employed. A sample holder with high thermal conductivity was used to fix the sample to the cooling finger of a closed cycle helium cryostat (CH-204, JANIS), which cooled the sample temperature down to cryogenic temperature. The cooling power of the cryostat was 13.5 W at 100 K. A Lake Shore temperature controller (DT 670) was used to monitor and maintain the sample temperature, which includes 2 silicon diode sensors and a 50 Ω heater. In addition, the active medium and the cooling finger were fixed at the center of a vacuum chamber, whose pressure was kept below 10^{-5} mbar to avoid condensation on the sample and chamber windows. The total dimension of the vacuum chamber along the optical axis was 100 mm. Inside the chamber, the sample was mounted at normal incidence to the pump light and its distance to L2 was L2's focal length. Taking the vacuum chamber dimension and the distance between L2 and the active medium into account, an asymmetric L-shaped cavity consisting of M1, M2, L3 and M3 was mounted. M1 was the plano-concave

cavity mirror HR coated for 1800 - 2200 nm. Its radius of curvature was ROC = - 300 mm. M2 was a dichroic mirror AR coated at the pump wavelength range on the rear side (left side on the graph), letting the pump radiation to transmit the active medium surface, and HR coated at the laser wavelength range on the front side of M2, bending the cavity into L-shape. L3 was a plano-convex lens with a focal length of 150 mm and AR coated at the laser wavelength. M3 was the plane output coupler (OC) with various transmissions (5, 9, 15, 20, and 30 %) at the laser wavelength. The distance between M1 and the active medium was ~ 300 mm including 110 mm between M2 and the active medium. After adjusting the cavity length for mode matching, L3 was placed 165 mm from the active medium and the total cavity length amounted to ~ 775 mm including the distance between L3 and M3 (310 mm). A photograph of the experimental setup in the laboratory is shown in Figure 4-2, in which the pump radiation is marked as the red line and the laser oscillation path is highlighted with yellow lines.

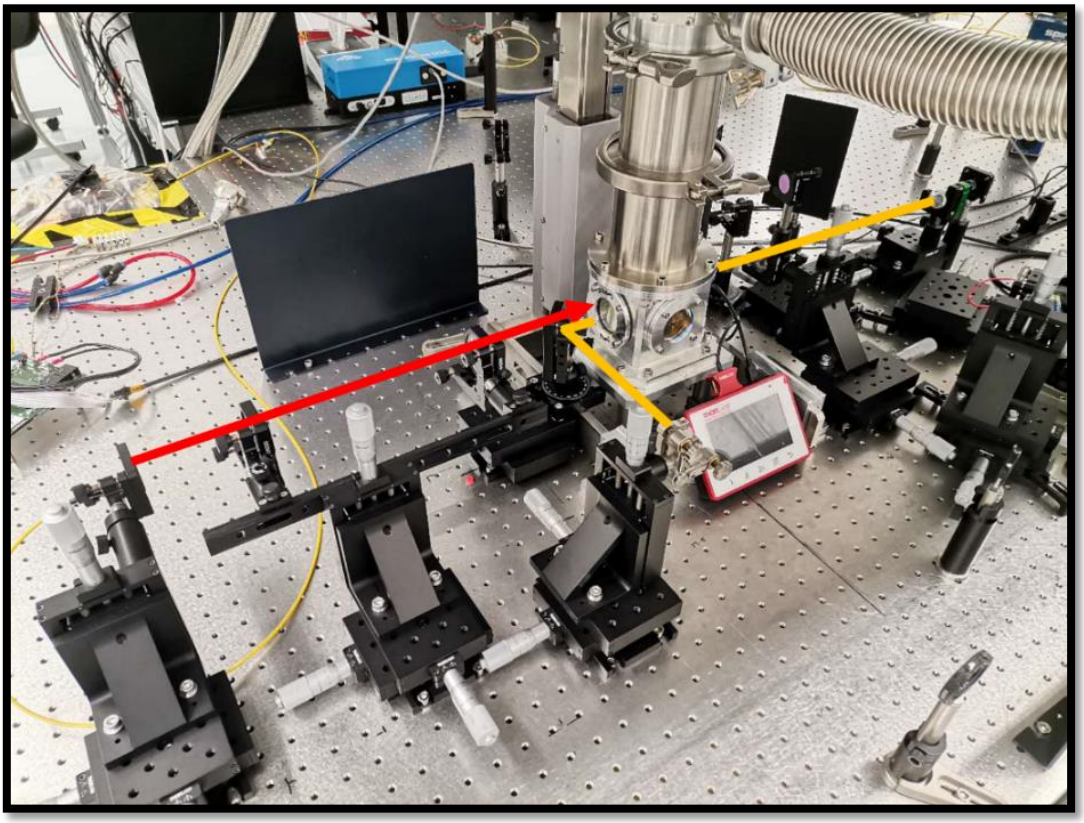

Figure 4-2 Photograph of the experimental setup in the laboratory. Red line: pump radiation, yellow line: laser oscillation path.

4.3. Results and discussion

4.3.1 Optimization of the pump source

In this section, to confirm the pump efficiency of both LD's, the wavelength of the pump source and sample absorption were compared first.

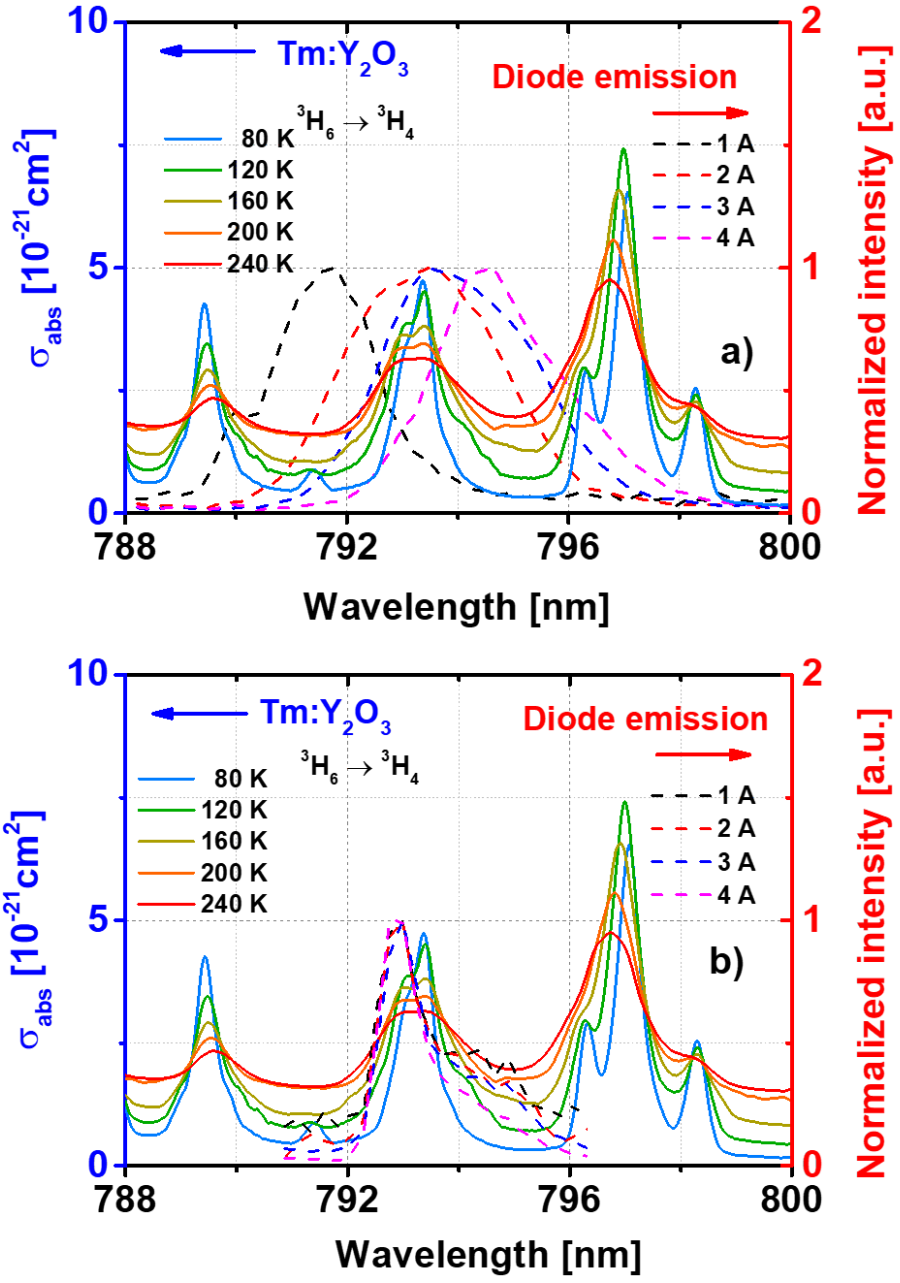

Figure 4-3 Dashed lines: emission spectra around 793 nm of (a) the broadband diode and (b) the VBG stabilized diode at various diode currents. Solid lines: Tm:Y_2O_3 absorption peaks around 793 nm at various temperatures.

As shown in Figure 4-3 (a), the dashed lines show the emission wavelength of the broadband LD at 25 ℃, which has a strong pump current dependence. As the pump current increases from 1 to 4 A (maximum allowed current: 4.4 A), the LD emission wavelength shifts from ~ 791 to ~ 795 nm. In addition, the bandwidth of this LD is much broader than the sample absorption peak at 793 nm (solid lines in Figure 4-3). At all currents, the pump wavelength/bandwidth matches only partially the 793 nm absorption peak. In contrast, as shown in Figure 4-3 (b), the emission wavelength of the VBG-stabilized LD does not change with the pump current (chiller temperature: 35 ℃) and the pump wavelength/bandwidth matches much better with 793 nm. For confirmation, CW lasing of Tm in Y_2O_3 transparent ceramics using both LD's was demonstrated and characterized.

In the first set of experiments, CW lasing was characterized using the broadband pump diode and the 3 at.% uncoated sample. By varying the chiller temperature of LD (20 – 35 ℃), the incident/output characteristics were achieved and shown in Figure 4-4 (sample temperature: 100 K, T_{OC}: 15 %). In the characteristics, the incident power was measured after the dichroic mirror (M2) and the Fresnel loss of the uncoated sample was not excluded. From the figure, one can see that clear linearity was obtained only at the chiller temperature of 20 ℃ and only at low pump power (< 8 W). At 20°C, the output power decreased for higher pump power. At other chiller temperatures, the slope efficiency changes with the incident power due to the shift of the pump wavelength. The highest slope efficiency of 13.6 % and maximum output power of 1.7 W were achieved at a LD temperature of 25 ℃.

With the chiller temperature fixed to 25 ℃, the laser output was tested for various T_{OC}'s at 80 K and for various sample temperatures with T_{OC} = 30 %, as shown in Figure 4-5 (a) and (b), respectively. From figure (a), one can observe that at 80 K the linear dependence is not clear and even lost for incident power > 15 W, irrespective to the T_{OC} value. This is mainly due to the mismatch between the absorption band of Tm:Y_2O_3 and the pump emission band of the diode. A maximum output power of 2.2 W with a slope efficiency of 16.4 % was achieved using an output coupler of Toc = 30 %.

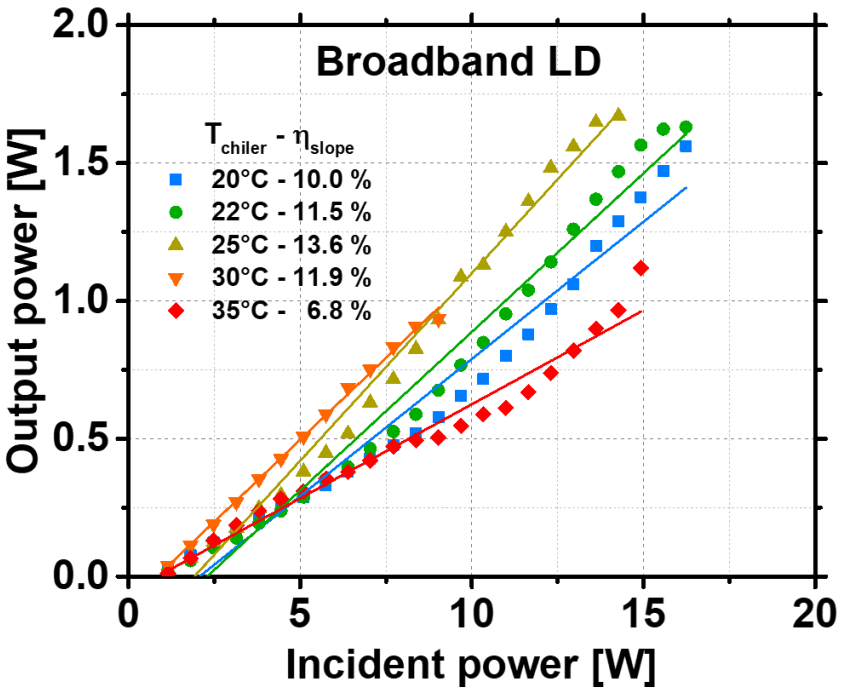

Figure 4-4 Incident/output characteristics of CW laser pumped by a broadband LD at various chiller temperatures, sample temperature fixed at 100 K, T_{OC} of 15 %.

When the sample temperature was increased from 80 K up to 120 K, the slope efficiency increased from 16.4 to 22.9 %, as shown in Figure 4-5 (b). This indicates a better absorption of the pump power at 120 K due to the increase of the absorption bandwidth at 793 nm. The absorption estimated at the threshold (non-lasing conditions) from 80 to 120 K increased from 21 to 28 %. When the temperature increased from 120 to 200 K, the slope efficiency decreased from 22.9 to 13.0 % due to the decrease of the absorption cross-sections and thermal effects.

In the next step, the VBG stabilized diode was employed as a pump source to obtain better wavelength/bandwidth matching between the pump and sample absorption. The chiller temperature of the LD varied from 25 to 35 ℃. As shown in Figure 4-6, the output power increases linearly with the incident power until 12.5 W, where a thermal roll-over starts to play a role. For all 3 chiller temperatures, the laser slope efficiency differs minor from each other ($\Delta\eta_{slope}$ ~ 2 %). The highest slope efficiency is 29.2 %, which was obtained at a chiller temperature of 35 ℃.

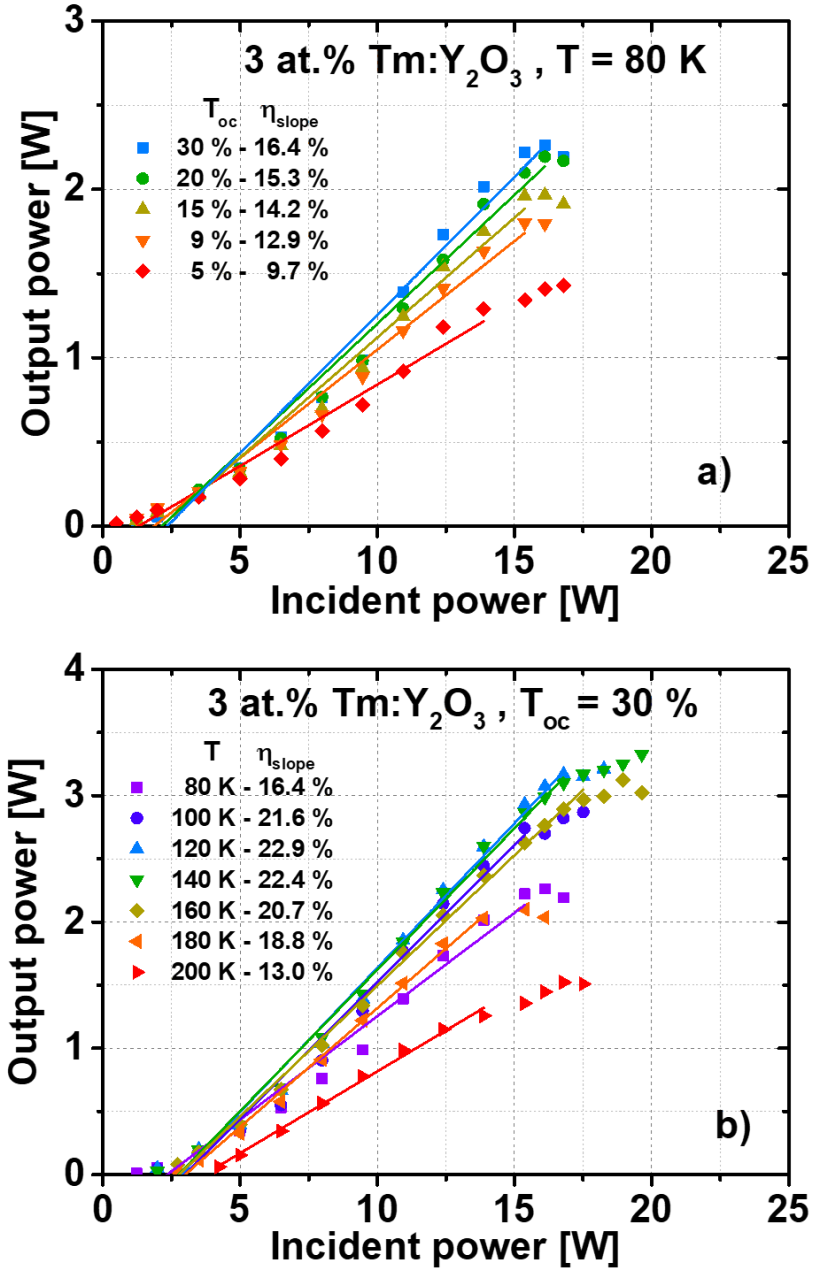

Figure 4-5 Incident/output characteristics and slope efficiency of the CW laser pumped by a broadband LD (a) at 80 K with various T_{OC}'s and (b) at various sample temperatures with T_{OC} of 30 %.

From this preliminary study of the laser pump sources, the importance of matching the wavelength and bandwidth of the sample absorption and the pump emission is confirmed. As summarized in Table 4-1, the VBG stabilized LD is advantageous in the further laser operations.

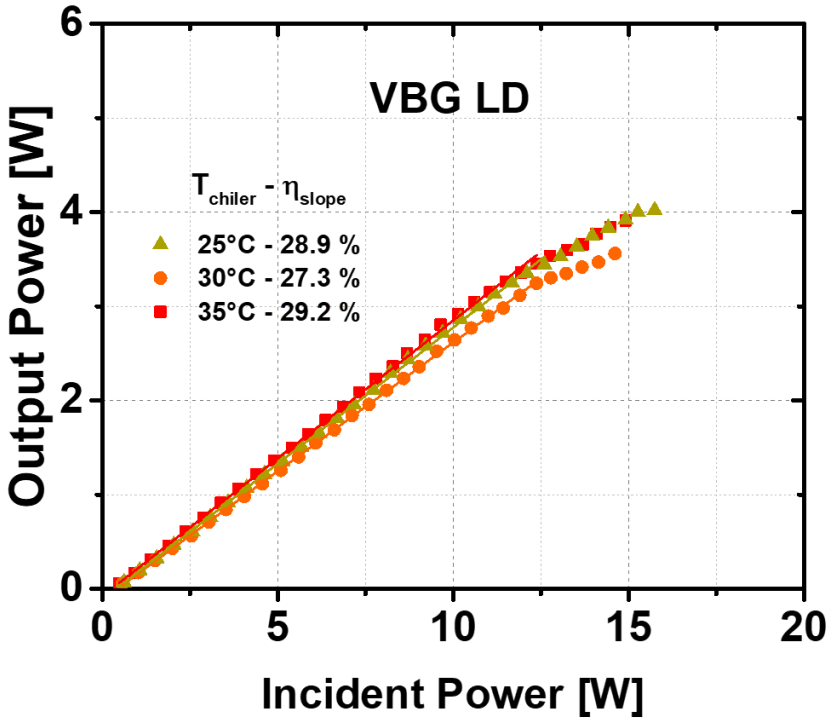

Figure 4-6 Incident/output characteristics and slope efficiency of a CW laser pumped by the VBG stabilized LD at various chiller temperatures, sample temperature fixed at 80 K, T_{OC} of 15 %.

Table 4-1 Comparison of the broadband and VBG LD's

LD	$\Delta\lambda_P$ [nm]	λ_P [nm]	$T_{chiller}$ [℃]	η_{slope} [%]	$P_{out,max}$ [W]	P_{in}/P_{out} linearity
Broadband	3	791 - 795	25	22.9 (@120 K)	3.3 (@120 K)	no
VBG	0.5	793	35	29.2 (@ 80 K)	4.0 (@ 80 K)	yes

4.3.2 Optimization of the cooling efficiency

In the previous experiments, the 3 at.% Tm:Y_2O_3 transparent ceramic was mounted in a brass sample holder. As already shown in Figure 4-6, the incident/output characteristics lost the linearity at incident powers > 12.5 W, where thermal roll-over started to play a role due to insufficient cooling power. For confirmation, CW laser using various T_{OC}'s (5, 9, 15, 20, and 30 %) was studied at 80 K. As shown in Figure 4-7 (a), the thermal issue appeared at high incident power for all T_{OC}'s. To increasing the cooling efficiency, a copper holder with the same dimension was used, whose incident/output characteristics and slope efficiencies are presented in Figure 4-7 (b). From the figure, one can see that the laser output/incident power linearity until the maximum pump power were well preserved at 80 K by using the copper holder.

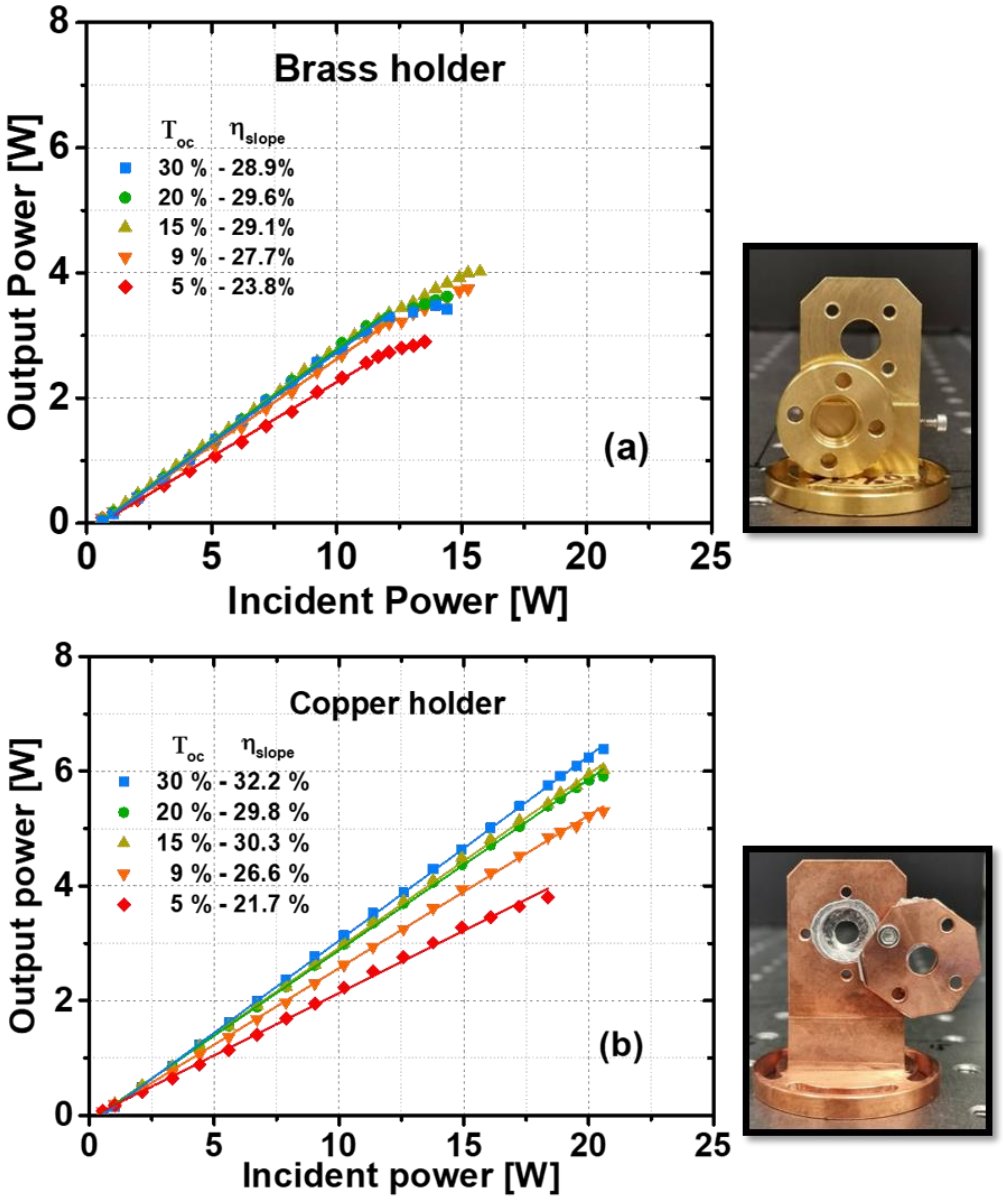

Figure 4-7 Incident/output characteristics and slope efficiency of CW laser with various T_{OC}'s at 80 K using 3 at.% sample mounted in (a) a brass holder and (b) a copper holder.

From the T_{OC} dependent slope efficiency, an intra-cavity loss at 80 K was estimated for this L-shaped cavity using eq. (4.12). This parameter shows the quality of the laser oscillator. As shown in Figure 4-8, the loss L was estimated to be 3.0 % from the fitted curve. This loss is mainly resulted from the transmission/reflection loss of the optical elements employed in the oscillator cavity. The Fresnel loss of the un-coated sample was exclusive in L but inclusive in the pump absorption efficiency, which was measured at 80 K under non-lasing threshold condition. From the intrinsic slope efficiency η_0, a quantum yield η_{QY} of 1.38 was

estimated, for which a pump absorption of 62 %, quantum efficiency of 41 % and mode coupling efficiency of 1 were used. The η_{QY} is much lower than the value at room temperature (~ 1.87 read from Figure 1-3). This low value of η_{QY} corresponds to a suppression of the phonon assisted cross-relaxation process due to the cryogenic temperature.

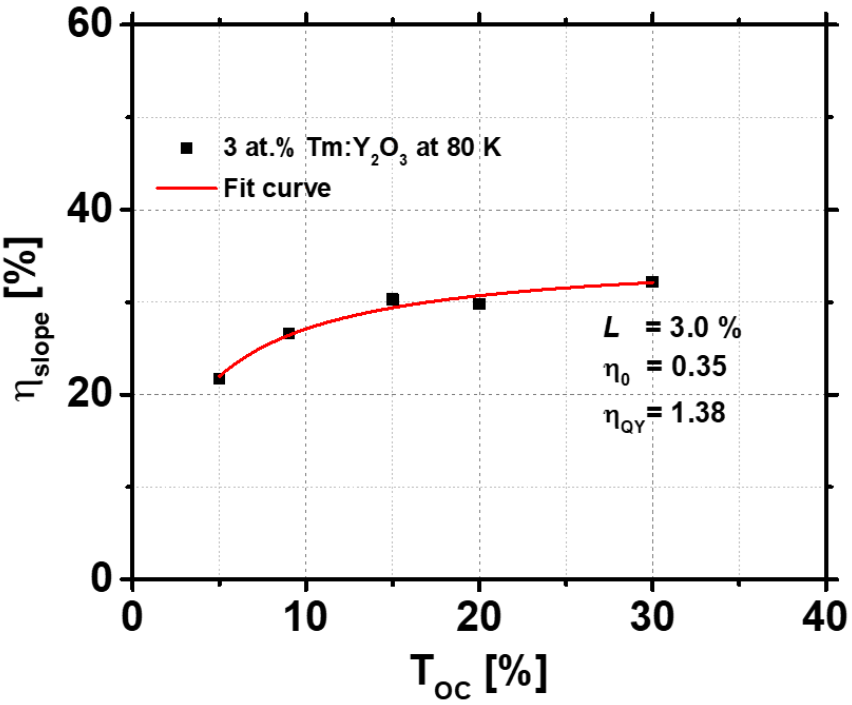

Figure 4-8 Slope efficiency as a function of T_{OC} and fitted curve for cavity loss estimation.

To confirm the necessity of cryogenic cooling, a sample temperature-dependent laser characterization was carried out from 80 to 180 K in step size of 20 K. For all temperatures, the T_{OC} was fixed to 30 %. The sample temperature was limited up to 180 K to avoid sample damage. The incident/output power characteristics are shown in Figure 4-9, where a clear influence of the sample temperature on the laser output and slope efficiency can be observed. Above 120 K, a thermal roll-over appeared at high incident power, which strongly limited the power scaling.

The laser threshold with respect to the incident power, maximum output power and slope efficiency were plotted as function of sample temperature in Figure 4-10. As the sample temperature increased, the laser threshold grew from 0.5 to 2.1 W resulting from the populating of lower laser level and the increased saturation flux. Besides, the maximum output power and slope efficiency decrease with the temperature from 6.4 to 2.1 W and from

32.2 to 18.7 %, respectively. This trend is mainly due to the influence of reabsorption and parasitic processes arising at higher temperatures. According to this performance, the cryogenic cooling is still beneficial despite the reduced quantum yield.

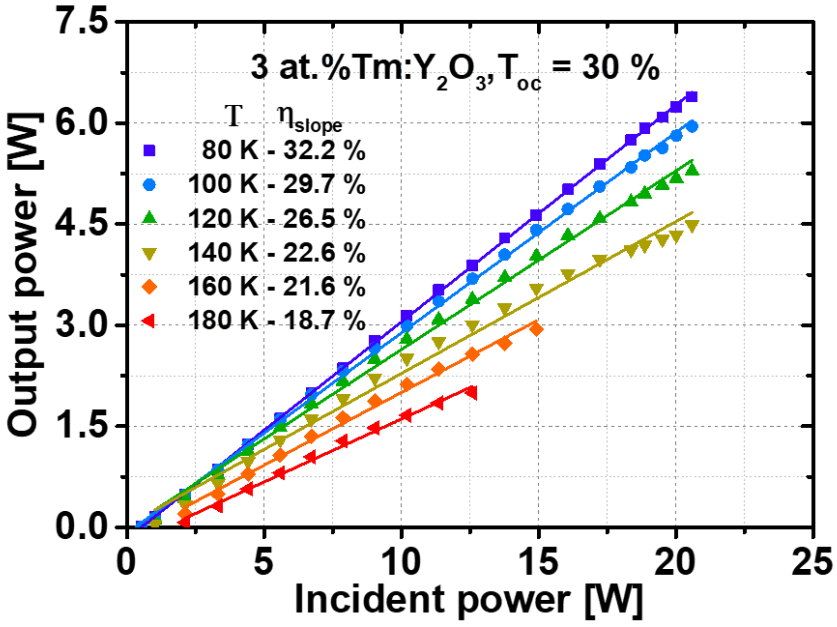

Figure 4-9 Incident/output characteristics and slope efficiency of CW laser at various temperatures, T_{OC} = 30 %.

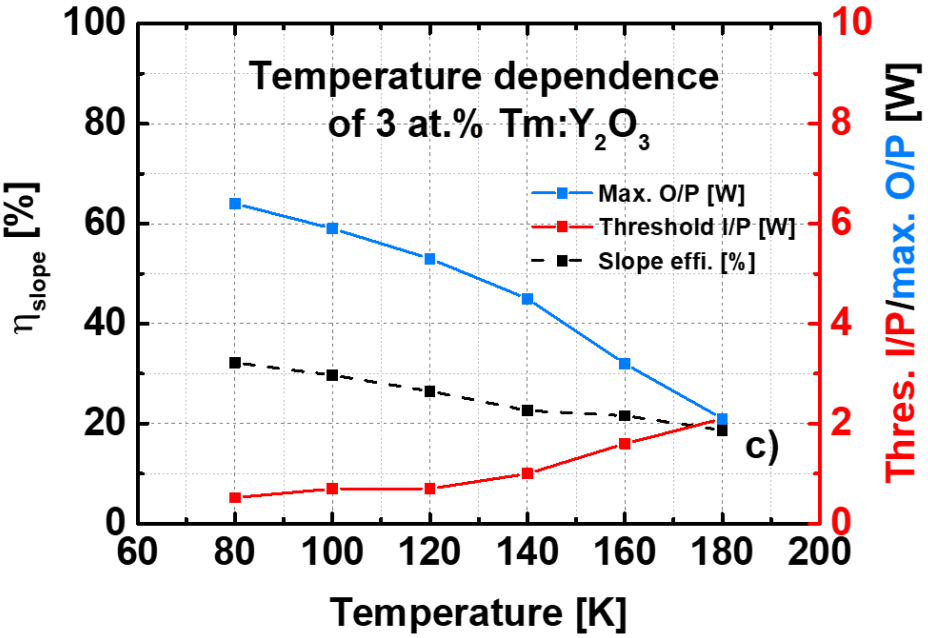

Figure 4-10 Threshold incident power, maximum output power and slope efficiency as function of sample temperature. T_{OC} is fixed to 30 %.

4.3.3 Dopant concentration dependence

As estimated in the previous section, the quantum yield at 80 K of this 3 at.% Tm:Y_2O_3 sample was estimated to be 1.38, which is lower than the theoretical maximum value of 2. To obtain a higher quantum yield at 80 K, which could consequently, lead to power scaling, a sample of 5 at.% was studied as the active medium.

As shown in Figure 4-11 (a), the CW lasing was firstly realized at 80 K using various T_{OC}'s. The output power increased linearly with the incident power, which was the same as the 3 at.% sample. No thermal roll-over was observed at this temperature, confirming a sufficient cooling efficiency. The highest slope efficiency of 43.0 % was achieved again using T_{OC} = 30 %, corresponding to a maximum output power (P_{max}) of 8.2 W at full incident power. The L and η_{QY} estimation are presented in Figure 4-11 (b). An intracavity loss of 3.0 % was found from the fitting, which matches well with the 3 at.% CW laser setup. From η_0, the quantum yield of this 5 at.% sample was estimated to be 1.59. The absorption efficiency was measured as 72 % under the same condition of 3 at.% sample. This increased η_{QY} reflects to an increase of η_{slope} and P_{max} compared to laser using the 3 at.% sample. A summary of the laser parameters using 3 and 5 at.% Tm:Y_2O_3 with respect to the incident pump power is shown in Table 4-2. From the table, one can see that the optimal laser setup parameters (T & T_{OC}) and the cavity quality (regarding the intra-cavity loss L) do not show dopant concentration dependence, while an overall improvement in laser performance was achieved by using the 5 at.% sample. The maximum output power increased from 6.4 W to 8.2 W, and the slope efficiency increased from 32.2 % to 43.0 %. So does the quantum yield, from 1.37 to 1.59. To be noted is that the threshold incident power decreased from 0.52 W (3 at.%) to 0.27 W (5 at.%). The corresponding threshold with respect to absorbed power was estimated to be 0.32 W (3 at.%) and 0.19 W (5 at.%). This 0.13 W decrease can be resulted from a lower saturation energy of the 5 at.% sample.

The temperature-dependent incident/output characteristics of 5 at.% Tm:Y_2O_3 was carried out only until 120 K, where the clear thermal roll-over started to affect the power scaling, as shown in Figure 4-12. To preserve the sample, no higher temperature was tested. The temperature dependence behaved the same as the 3 at.% sample. At temperature > 120 K,

higher cooling efficiency is required for the 5 at.% sample by methods such as increasing the sample holder cooling area, increasing cryostat's cooling power, etc.

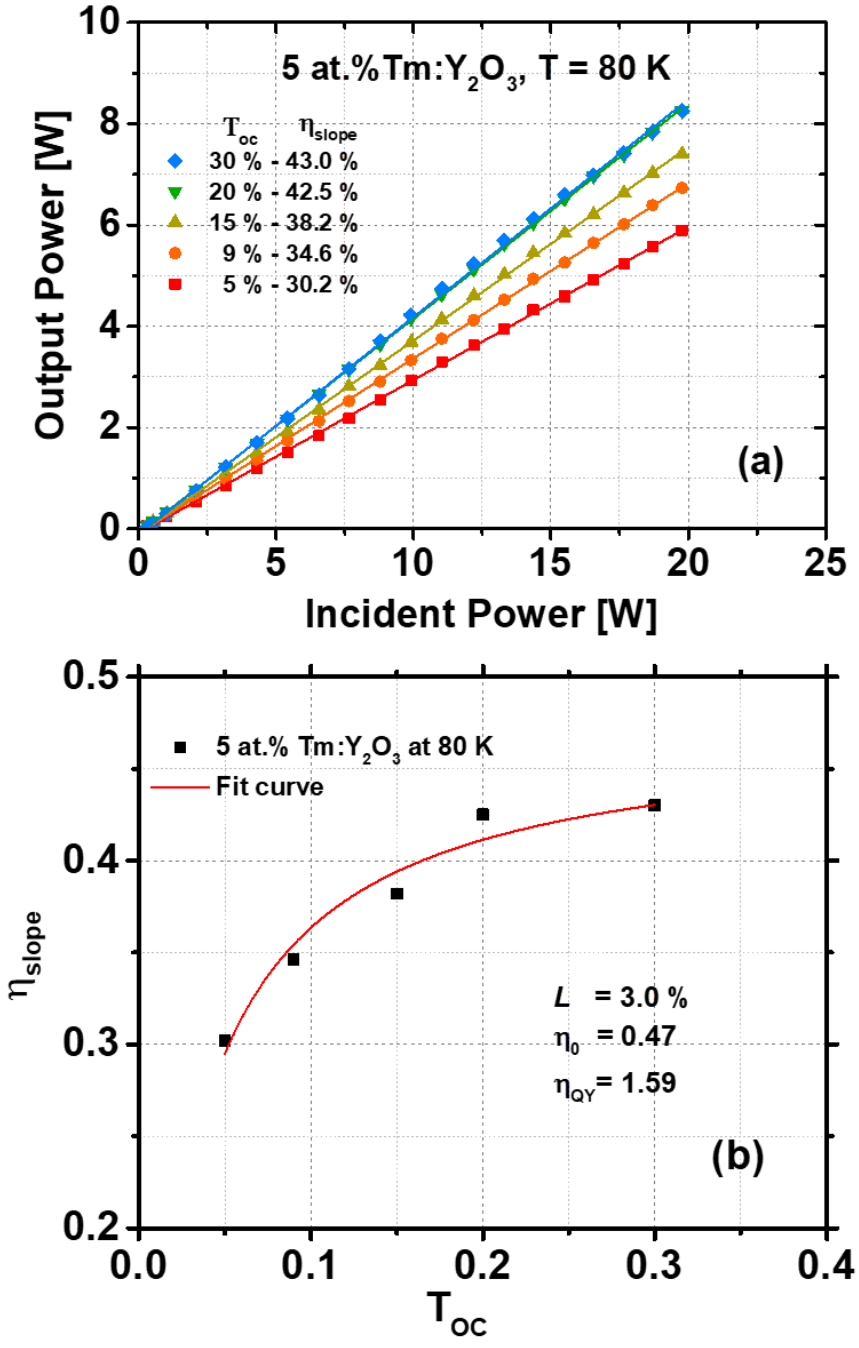

Figure 4-11 (a) Incident/output characteristics of 5 at.% Tm:Y_2O_3 using various T_{OC}'s, operating at 80 K; (b) slope efficiency as a function of T_{OC} and fitted curve for cavity loss estimation.

Table 4-2 Comparison of laser using 3 and 5 at.% Tm:Y_2O_3 transparent ceramics

Dopant %	T [K]	T_{OC} [%]	P_{th} [W]	$P_{out,max}$ [W]	η_{slope} [%]	η_{QY} [%]	L [%]
3	80	30	0.52	6.4	32.2	1.37	3.0
5	80	30	0.27	8.2	43.0	1.59	3.0

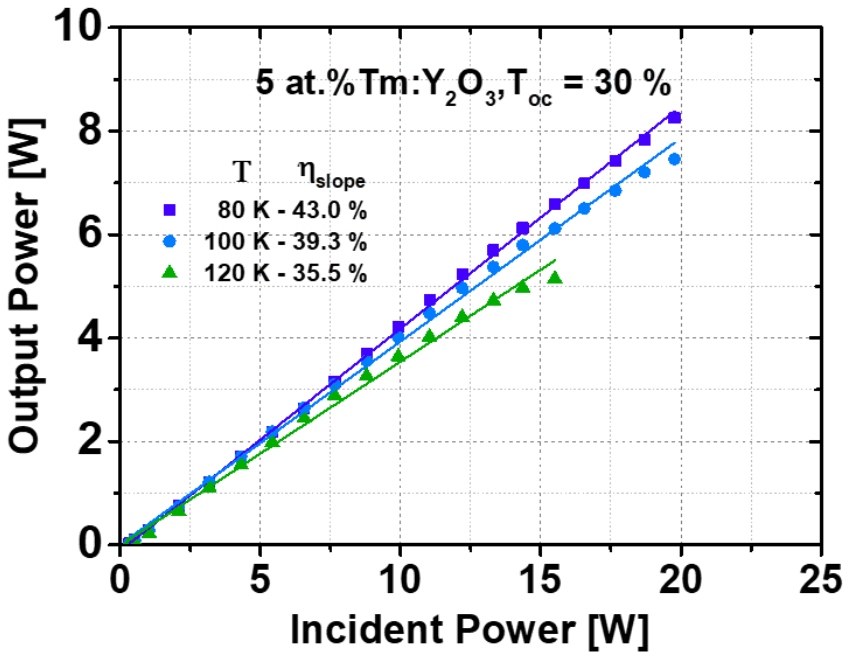

Figure 4-12 Incident/output characteristics of 5 at.% Tm:Y_2O_3 at 80, 100, and 120 K using T_{OC} = 30 %.

4.3.4 Laser wavelength and beam quality

The laser wavelength of the CW laser using various T_{OC}'s and at each temperature were measured for both 3 and 5 at.% Tm samples. As shown in Figure 4-13, all laser wavelengths centered at ~ 1932 nm for different T_{OC}'s at 80 K and using T_{OC} = 30 % at different temperatures until 180 K for 3 at.% and until 120 K for 5 at.%. This result matches well with the previous gain cross-section study in 3.2.5.

For both 3 and 5 at.% samples, the far field profile of the laser beam at full pump power was measured by using a wedge to reflect the beam to the Pyrocam camera and to reduce the intensity arriving at the camera. As shown in Figure 4-14, high-quality Gaussian beam was measured for both samples. The beam size difference was due to the different magnification used in the BeamGage software during measurement.

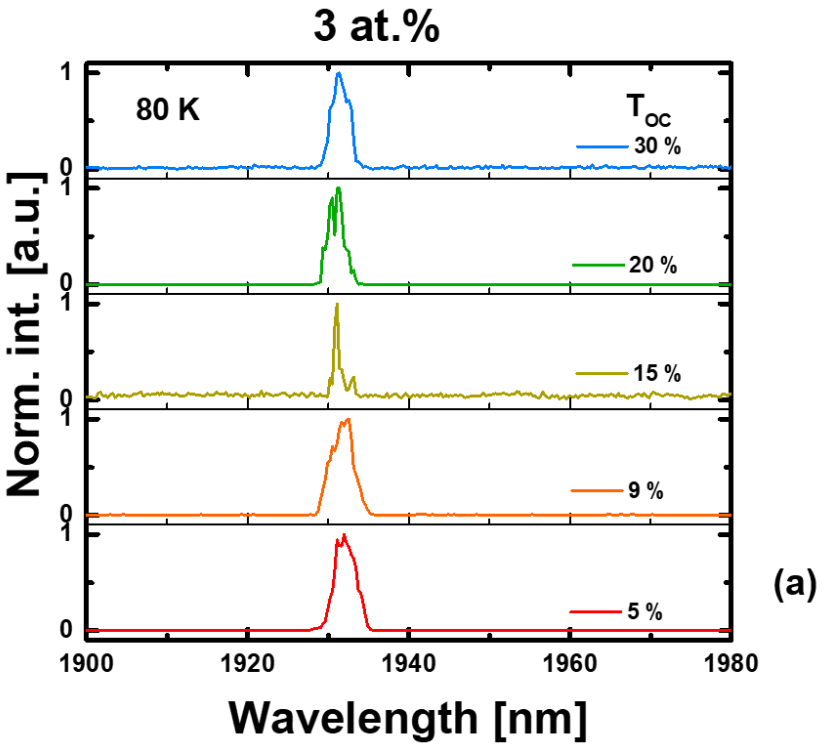
3 at.%
80 K
T_OC
30 %
20 %
15 %
9 %
5 %
Norm. int. [a.u.]
Wavelength [nm]
1900
1920
1940
1960
1980
(a)

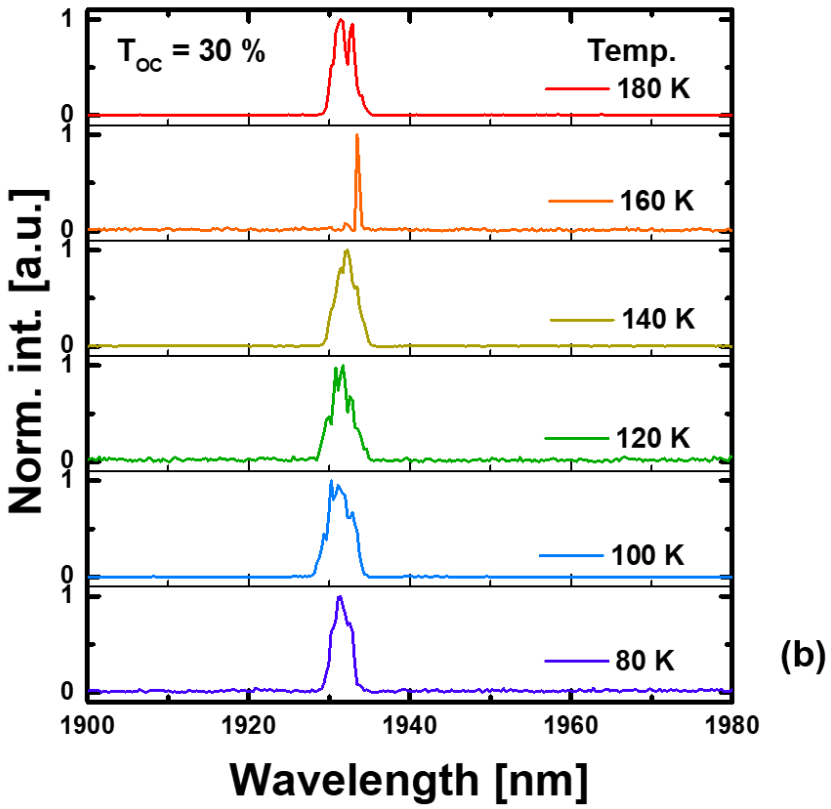
T_OC = 30 %
Temp.
180 K
160 K
140 K
120 K
100 K
80 K
Norm. int. [a.u.]
Wavelength [nm]
1900
1920
1940
1960
1980
(b)

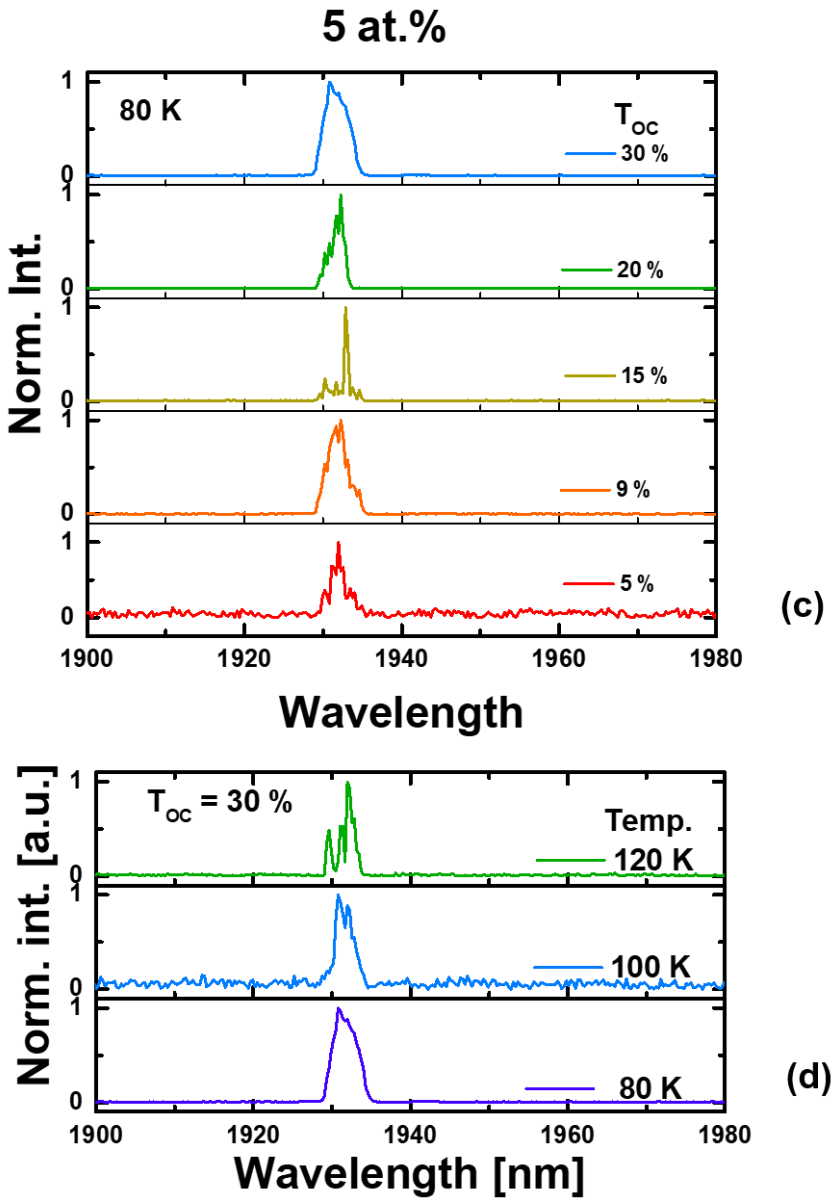

Figure 4-13 Laser wavelengths of 3 and 5 at.% samples (a) and (c) with various T_{OC}'s at 80 K, (b) and (d) with T_{OC} = 30 % at various sample temperatures, respectively.

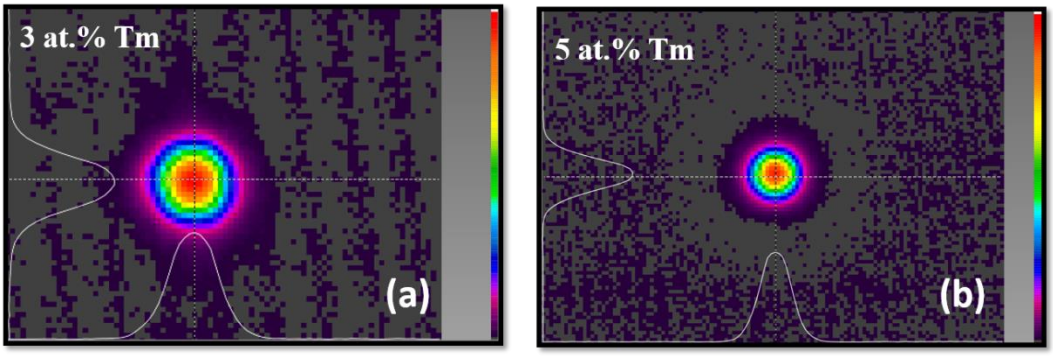

Figure 4-14 Far field laser beam profiles of the (a) 3 at.% sample and (b) 5 at.% Tm samples.

4.4. Summary

In this chapter, the laser potential of 3 and 5 at.% Tm:Y_2O_3 transparent ceramics at cryogenic temperatures were tested and confirmed by establishing a CW L-shaped two-mirror oscillator. From the experimental results, optimal laser design parameters were obtained. As pump source, a VBG stabilized LD emitting at 793 nm was preferred, which provided a high wavelength and bandwidth match with the sample absorption. Bulk copper sample holder was designed, which provided sufficient heat removal to preserve the laser output/incident linearity at cryogenic temperature. The sample temperature was optimal at 80 K, where better slope efficiency and maximum output power were achieved compared to higher temperatures (until 180 K). 5 at.% sample possessed higher maximum output power (8.2 W) and higher slope efficiency (43.0 % with respect to the incident power) compared to the 3 at.% sample. Samples with dopant concentration higher than 5 at.% were not tested here, which will require much higher cooling efficiency to mitigate the thermal induced issues. Regarding other laser parameters, i.e., lasing wavelength and beam quality, both samples showed a high rate of agreement. The lasing wavelength was found at ~ 1932 nm. The laser beam was a high quality Gaussian single mode. Thus, for the further MOPA demonstration, the operation temperature of the seed oscillator will be fixed at 80 K.

4.5. References

[1] W. Koechner, *Solid-State Laser Engineering*, New York: Springer, p. 17, (1986).
[2] S. So, *Power scaling of Tm:YLF-pumped Ho:YAG lasers*, University of Southampton, Optoelectronic Research Centre, Doctoral Thesis, (2007).

Chapter 5

Cryogenic master oscillator

This chapter is aimed at fulfilling the second objective of this work. The pulsed lasing potential of the Tm:Y_2O_3 transparent ceramics was studied at various repetition rates, and a master oscillator was demonstrated as the seed source for the further amplification. The laser experiments were carried out in the laboratory of HiLASE Centre, Institute of Physics of the Czech Academy of Sciences, Dolni Brezany, Czech Republic.

5.1. Experimental setup

The pulsed lasing was realized using the setup shown in Figure 5-1. The setup was modified from the CW laser setup described in chapter 4. The cavity included two HR mirrors (M1 & M3), a dichroic mirror (M2), a plano-convex lens (L3), a thin film polarizer (TFP), a rotatable λ/4-plate and a RTP (Rubidium Titanyl Phosphate) Pockels cell (PC). The TFP and the rotatable λ/4-plate functioned together as an adjustable output coupler and the RTP PC worked as an electro-optic switch. The pump source was the same as in the previous CW setup and the pulsed pumping was triggered by an external digital delay generator (DG645, Stanford Research Systems, Figure 3-5), which also triggered the PC. As the active medium, a 3 at.% AR-coated Tm:Y_2O_3 transparent ceramic was used, which had a diameter of 10 mm and a thickness of 3 mm. The sample temperature was kept at 80 K to achieve gain matching with further amplification.

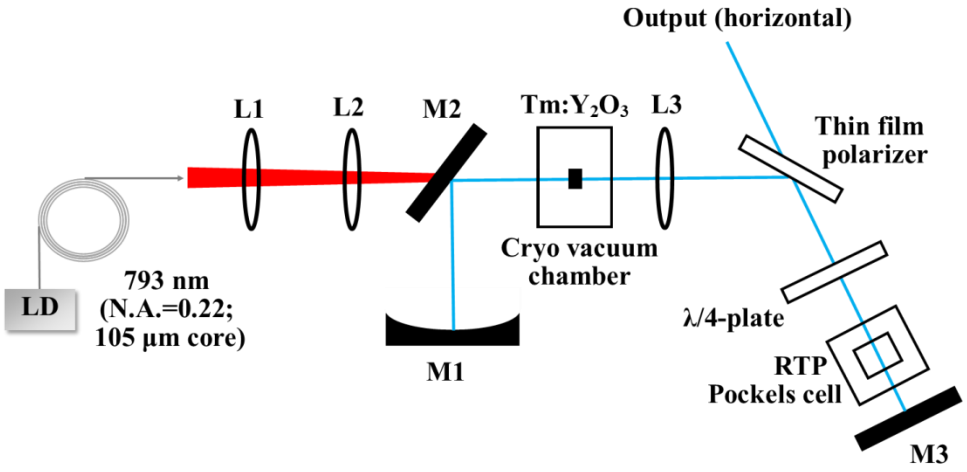

Figure 5-1 Sketch of the cavity-dumped MO setup. L1 & L2: achromatic lenses; M1: concave mirror; M2: dichroic mirror; M3: plane mirror; L3: plano-convex lens; λ/4-plate: rotatable quarter wave plate; TFP: thin film polarizer; RTP PC: $RbTiOPO_4$ Pockels cell.

To understand the function of the adjustable OC, Figure 5-2 is illustrated. As shown in the figure, the TFP worked as a polarization-dependent beam splitter, as it highly reflected s-polarized (vertically polarized) light and totally transmitted p-polarized (horizontally polarized) light. Thus, the radiation ① emitted from the active medium was split on the TFP and its vertical part (marked as ②) was reflected and passed through the λ/4-plate (as shown at position ③). The transmitted radiation was then reflected back by the HR mirror (marked

as ④) and passed the λ/4-plate for the 2nd time, shown as ⑤. When the λ/4-plate fast axis was rotated at an angle of α to the vertical direction, the polarization of ⑤ and ⑥ was mirrored along the fast optical axis and had an angle of 2α to the vertical direction, because the λ/4-plate functioned as a λ/2-plate for each double-passed light. The p-polarized part of ⑥, which was in a ratio of $\sin^2(2\alpha)$, was then coupled out through the TFP. The output coupling transmission is written as:

$$T_{OC,adj} = \sin^2(2\alpha). \tag{5.1}$$

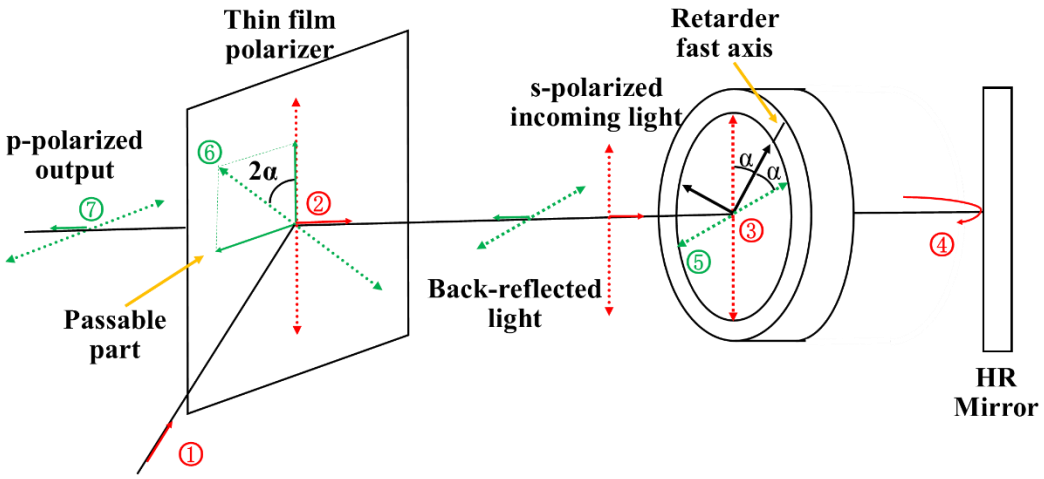

Figure 5-2 Principle of the polarization based adjustable output coupler.

In the pulse generation process via cavity dumping, $T_{OC,adj}$ should be periodically switched between 0 (for α = 0° or 90°) and 1 (for α = 45°). To actively alter the $T_{OC,adj}$, an electro-optical switch PC was inserted between the λ/4-plate and HR mirror. The cavity dumping was then achieved with the following steps:

1) Before switching on the PC, the λ/4-plate angle was fixed at 45°. In this phase, the cavity had high loss and no oscillation happened.
2) The λ/4-voltage of the PC was applied for an accumulation time t_{acc}. The PC worked as another λ/4-plate, whose fast axis was placed at 45° or - 45°, so that a total α was changed to 90° or 0°. In this phase, the cavity had low loss and all energy was held inside the cavity.
3) The λ/4-voltage was removed from the PC and the effect of the PC was canceled. The total α was changed back to 45°, and the accumulated energy was dumped out.

To be noted is that the intra-cavity oscillation mode was vertically polarized while the

output beam was horizontally polarized. The photographs of the whole MO setup, the RTP PC as well as its driver are shown in Figure 5-3.

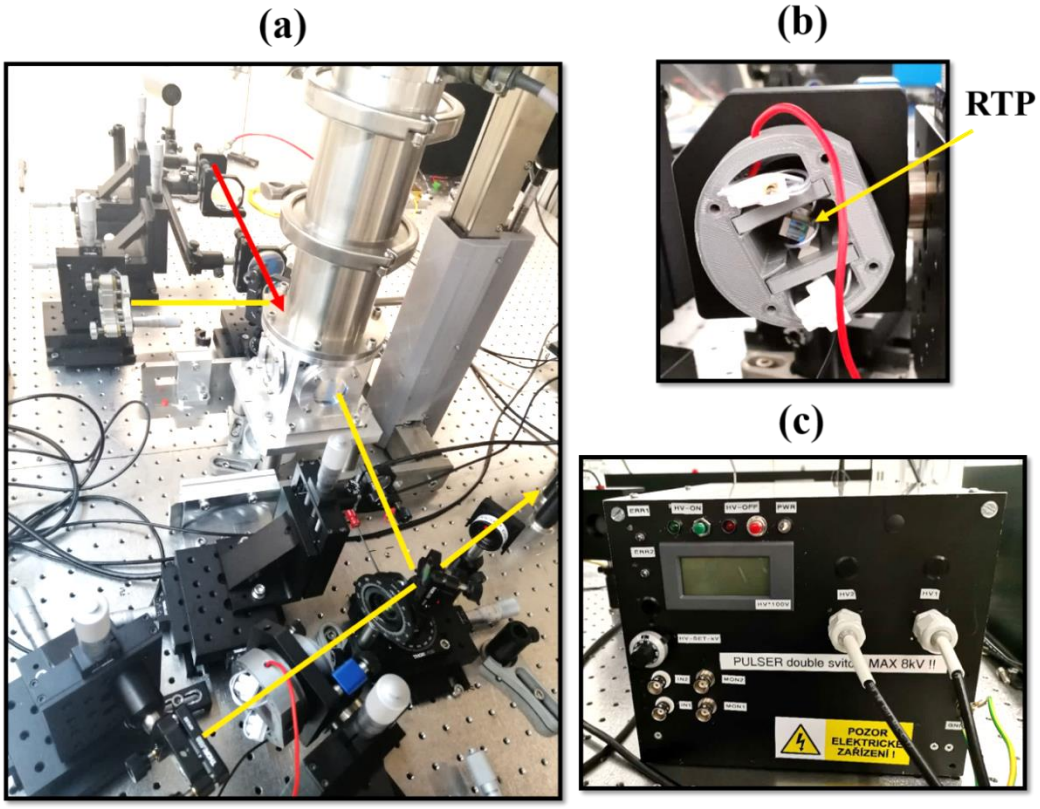

Figure 5-3 Photograph of (a) the experimental MO setup in the laboratory, (b) the RTP PC inside a 3D printed holder, and (c) the home-made high voltage driver for PC.

5.2. Results and discussion

5.2.1 Optimization in the CW regime

In this experiment, the distance between each optical component in the oscillator cavity was optimized in the CW regime. The output/incident power characteristics were measured for the optimized cavity setup with and without PC, as shown in Figure 5-4. The maximum CW output power was achieved when the λ/4-plate fast axis was rotated 12˚ from the s-polarization (clockwise direction). Comparing these two curves in the figure, one can see that, in the CW laser regime, introducing the PC resulted in almost no extra loss to the cavity (< 0.2 %). The laser wavelength was 1932.5 nm (measured by waveScan, A.P.E.), as shown in the inset of Figure 5-4.

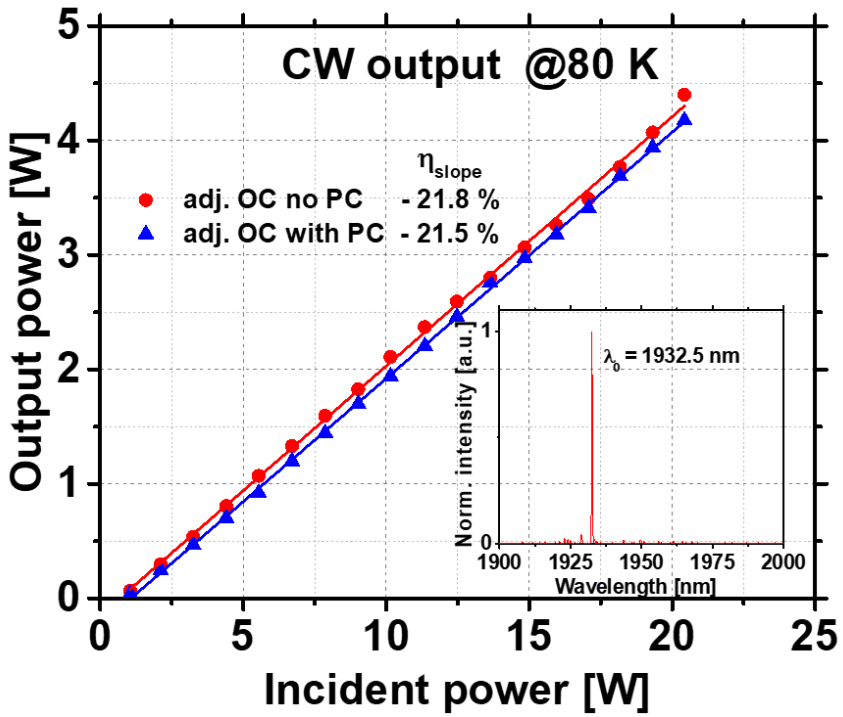

Figure 5-4 Output/incident power characteristics for CW cavity with (blue line) and without (red line) PC. Inset: laser wavelength measured at maximum output power.

5.2.2 Tunable cryogenic master oscillator

Employing the optimized cavity setup, the pulsed lasing potential was studied at various repetition rates and a seed laser oscillator was demonstrated. In the relative lower repetition rate regime (≤ 100 Hz), the pump duration was set to 7 ms, corresponding to a pump duty cycle of 0.7, 7, 35, and 70 %, for 1, 10, 50 and 100 Hz, respectively. In the relative higher repetition rate regime (0.5 – 2 kHz), a CW pumping was applied due to the slow rise time of the LD driver. In all experiments, a λ/4-voltage of 1.4 kV was applied to the PC and its accumulation time was set to be 50 ns, which was the lower limit of the PC driver.

- **Low repetition rate regime**

In this regime, the repetition rates of 1, 10, 50, and 100 Hz were tested. The output energy/average power was plotted as a function of the incident pump energy/power in Figure 5-5 (a) and (b), respectively. As shown in Figure 5-5 (a), at the lower rep. rates, the output pulse energy increases linearly with the incident pump energy and no clear variation due to the repetition rate was observed, which indicates that the active medium was cooled

efficiently until 100 Hz. This was also confirmed in the average output power with respect to the incident power shown in figure (b). The output power is free from any thermal rollover.

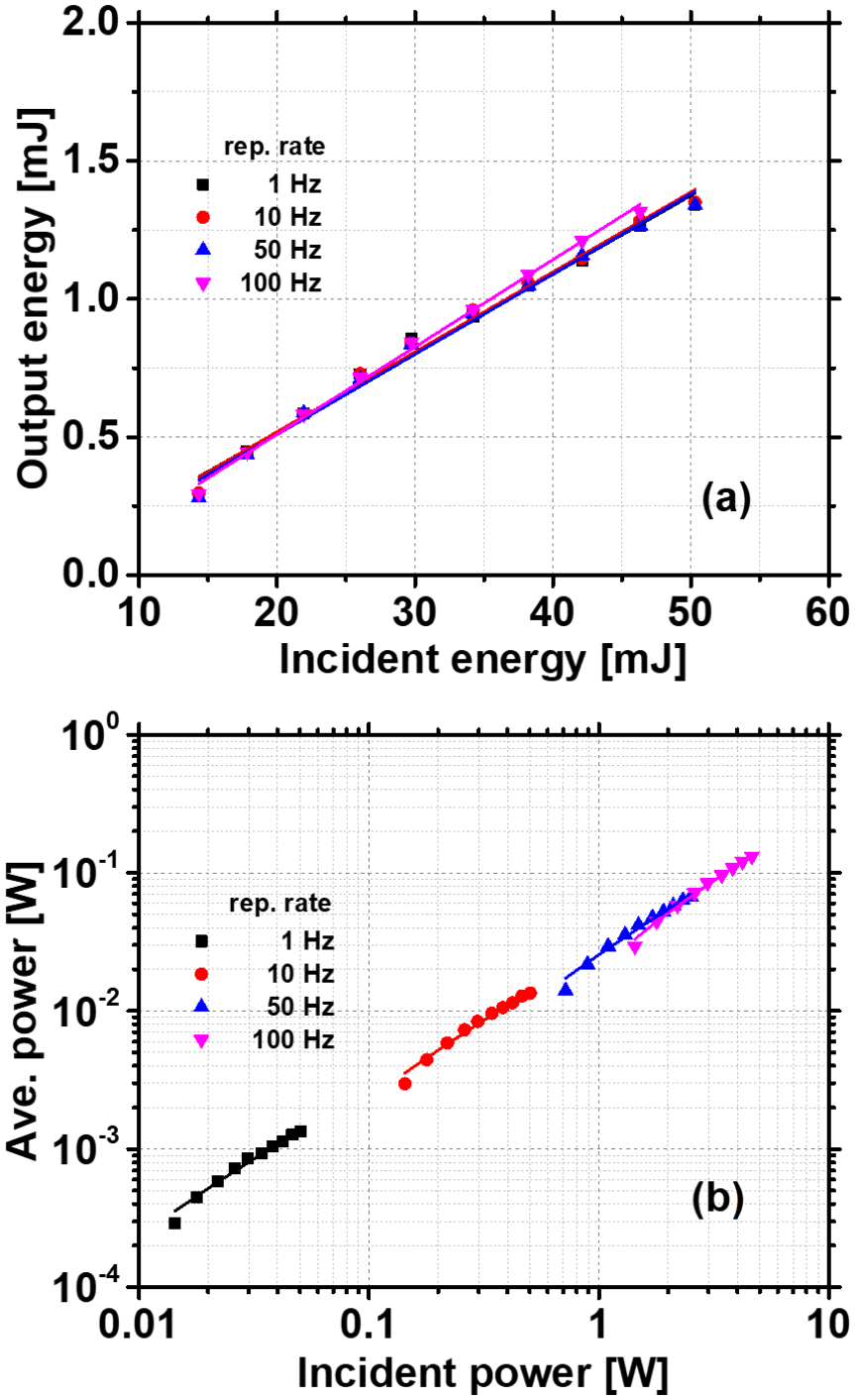

Figure 5-5 (a) Output/incident energy characteristics of seed pulses at various rep. rates ≤ 100 Hz and (b) the corresponding average power achieved.

A maximum single pulse energy of 1.35 mJ was obtained at 10 Hz and the maximum average output power achieved was 132 mW at 100 Hz. The measured pulse durations at various repetition rates showed consistency and were measured to be around 30 ns. Calculated

from the maximum achieved single pulse energy and the corresponding pulse width, a maximum peak power of 45 kW was obtained in this regime. A typical oscilloscope trace of the output single pulse (measured by UPD-3N-IR2-P, Alphalas) and its far field beam profile (measured by Pyrocam IIIHR, Ophir) are presented in Figure 5-6.

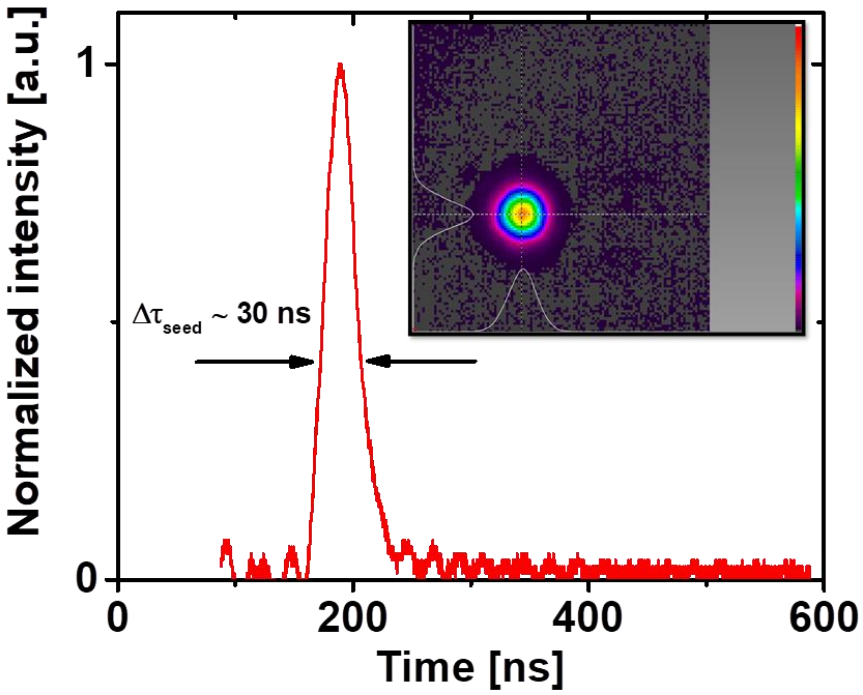

Figure 5-6 Oscilloscope trace of the 1.35 mJ pulse obtained at 10 Hz. Inset: corresponding far field beam profile.

- **High repetition rate regime**

In this regime, the tested repetition rate varied from 0.5 to 2 kHz. As shown in Figure 5-7 (a), the single pulse energy increased linearly with the incident CW pump power but decreased with the increase of the rep. rate. This can also be observed in the output/incident average power characteristics shown in Figure 5-7 (b). Although the maximum achieved average power increased with the rep. rate, this increase became minor from 1.5 to 2 kHz. This could be explained by the increased heat deposited in the active medium. The maximum average power achieved was 1.2 W at 2 kHz under the incident pump power of 6.7 W, beyond which sample damage was observed. Thus, higher pump power and higher repetition rates were not tested.

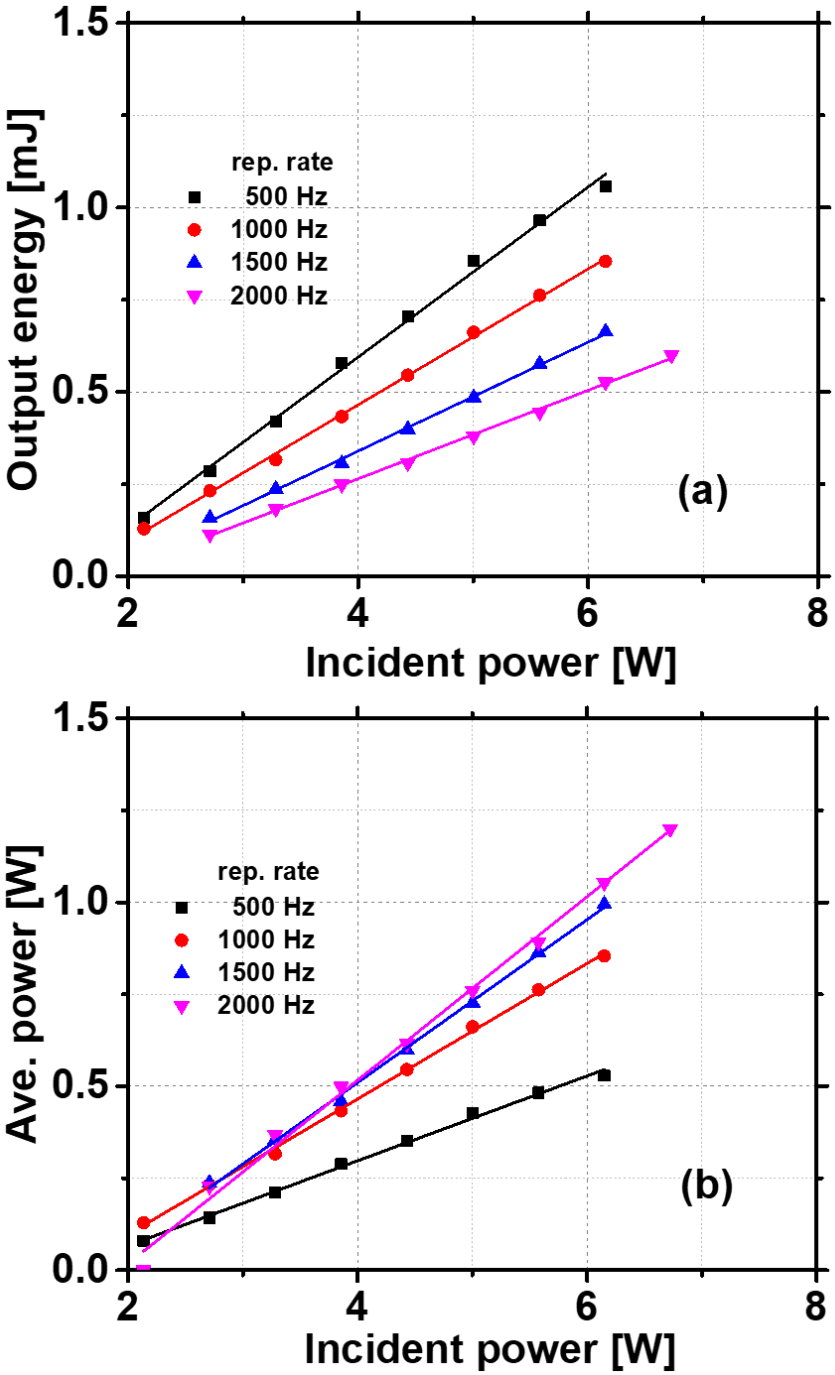

Figure 5-7 (a) Output/incident energy characteristics of seed pulses at various rep. rates from 0.5 – 2 kHz and (b) the corresponding average power.

5.2.3 Characterization of the seed pulse

The seed pulses were characterized in terms of energy and pointing stability. These parameters are of importance for potential applications as well as for further amplification.

The energy stability was characterized for one hour using an energy meter (VEGA, Ophir). The single pulse energy (measured after FI) and the rep. rates were set to 1 mJ, 10 Hz

in the probe test. As shown in Figure 5-8 (a), the average pulse energy (rms) was detected as 0.97 mJ. The minimum, medium and maximum single pulse energies were 0.75, 0.97, and 1.08 mJ, respectively. A standard deviation was measured as 0.04 mJ. Accordingly, the seed energy stability was estimated to be 4.1 %.

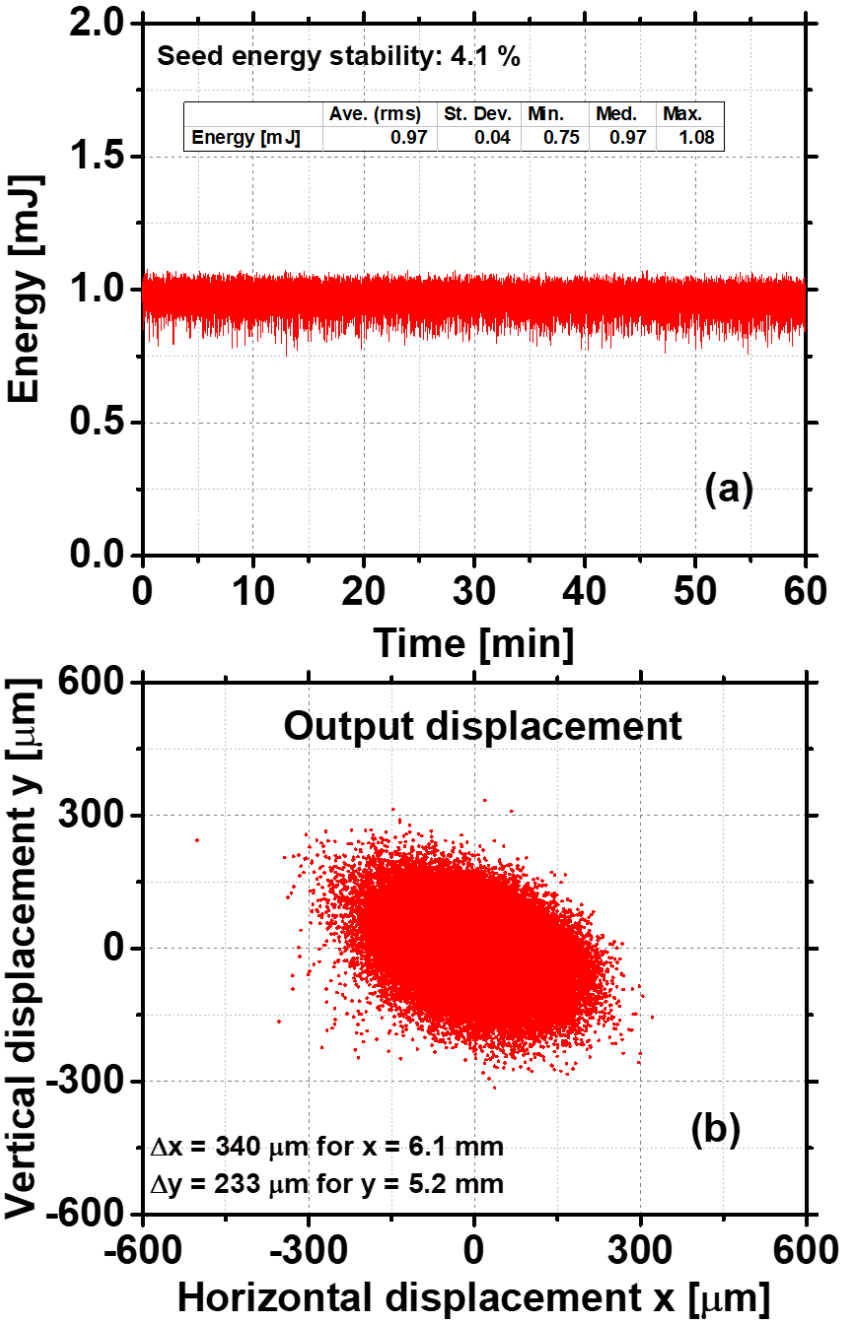

Figure 5-8 (a) Energy stability of 1 mJ pulses measured for 1 hour. (b) Seed horizontal and vertical displacement measured for 30 minutes. Δx/Δy: displacement in x/y direction; x/y: beam size in x/y direction.

The spatial displacement (pointing stability) was measured for 30 min. The measurement

was carried out in both horizontal and vertical direction for the free space propagating seed pulses by using the Pyrocam IIIHR, which was placed before the amplifier stage (after FI). As shown in Figure 5-8 (b), the displacements in the horizontal and vertical directions were, respectively, 340 and 233 μm for a D4σ beam diameter of 6.1 and 5.2 mm measured after a long distance free space propagation (being around 2 meters from the MO to the amplifier stage). The corresponding relative displacements were calculated as 4.5 and 5.6 %, respectively.

5.3. Summary

In this chapter, a master oscillator was demonstrated and the pulsed lasing potential of the cryogenically cooled Tm:Y_2O_3 transparent ceramics was studied. The repetition rate of the MO was tuned from 1 Hz to 2 kHz. A maximum pulse energy of 1.35 mJ was achieved at 10 Hz with a pulse duration of 30 ns, corresponding to a peak power of 45 kW. The maximum average power achieved was 1.2 W at 2 kHz. The pulses generated possessed sufficient energy/power to serve as the seed source for the further amplification process.

Chapter 6

Cryogenic multi-pass amplifier

In this chapter, the final objective of the thesis was accomplished. Cryogenic multi-pass amplifiers were demonstrated via multiple geometries. The amplifier parameters were optimized using a double-pass geometry. Further energy scaling was achieved via a four-pass amplifier setup. The experiments were carried out in the laboratory of HiLASE Centre, Institute of Physics of the Czech Academy of Sciences, Dolni Brezany, Czech Republic.

6.1. Experimental setup

6.1.1 Double-pass amplifier

To amplify the seed pulses, a double-pass setup was firstly demonstrated to test the amplification parameters. As shown in Figure 6-1, the pump diode possessed the same parameters as the one used in the MO, and the pulsed pumping was synchronized with the seed pulses by the same digital delay generator used in the MO. The pump radiation was imaged onto the active medium in a ratio of 1:6 by the AR coated achromatic lenses L4 and L5 (focal length *f* of 50 and 300 mm, respectively). As gain medium, an AR coated 5 at.% Tm:Y_2O_3 transparent ceramic (3 mm thick and 10 mm in diameter) was mounted inside a home-made vacuum chamber (pressure < 10^{-6} mbar) using a copper holder. Indium foil was applied between the sample and the copper holder to enhance the thermal contact. The sample and chamber windows were placed at normal incidence to the pump radiation. The cool finger connected to the sample was directly cooled by liquid nitrogen (LN2). To maintain the cooling effect, LN2 was refilled every half hour during the whole experiment.

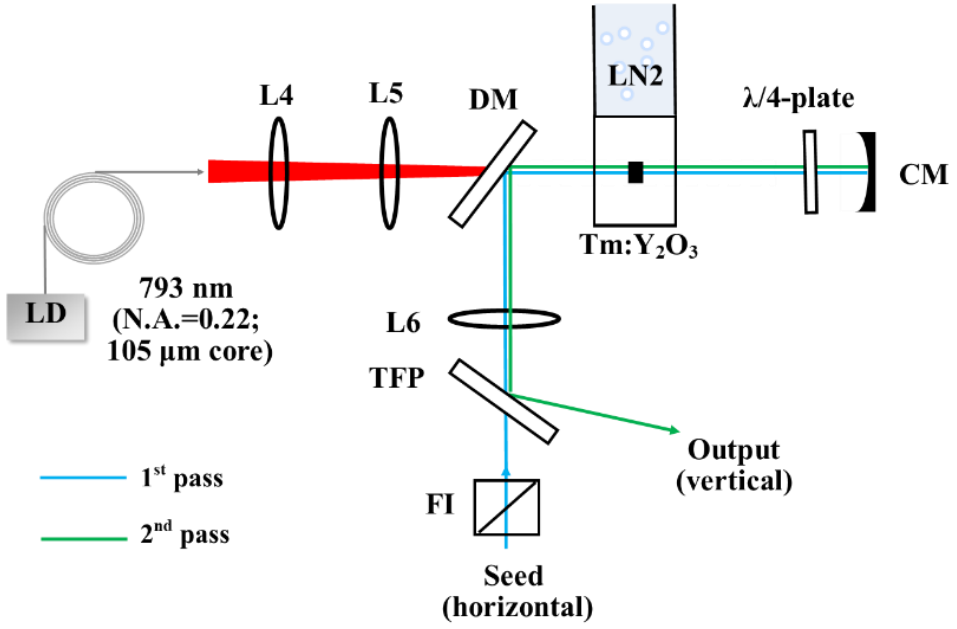

Figure 6-1 Sketch of the double-pass amplifier setup. Red line: pump radiation, blue line: the 1st laser pass, green line: the 2nd laser pass. L4 & L5: AR coated achromatic lenses; FI: Faraday isolator; TFP: thin film polarizer; L6: AR coated thin lens; DM: dichroic mirror; CM: curved mirror.

The double-pass amplification was realized based on the polarization-dependent beam splitter TFP. Since the seed pulses were horizontally polarized, they transmitted the TFP & L6

fully. After being bended by the DM, these seed pulses passed through the gain medium & the λ/4-plate for the 1st time at normal incidence and were reflected back by the curved mirror CM (ROC = -500 mm) to realize a 2nd pass through the sample and the λ/4-plate. In this scenario, the double-pass amplified pulses were changed to be vertically polarized due to a double-pass through the λ/4-plate and exited the amplifier cavity via a total reflection on the TFP. To be noted is that a Faraday isolator (FI) was placed before the amplifier stage to avoid back-reflection damage to the MO. The thin lens L6 (f = 250 mm) and CM adjusted the laser beam size on the sample. The pulse energy, pulse duration, and beam profile of the amplified light were monitored by an energy meter (PE25-C, Ophir), an ultrafast photodetector (UPD-3N-IR2-P, Alphalas) and a beam profiler camera (Pyrocam IIIHR, Ophir), respectively.

6.1.2 Four-pass amplifier

For further energy scaling, a four-pass amplifier was demonstrated by modifying the previous double-pass setup. As shown in Figure 6-2, after passing the TFP, L6 and a λ/4-plate, the injected seed pulses passed through the gain medium at an angle of ~ 6° to the pump beam via the direction of a HR plane mirror (M4). Then, the laser beam was reflected back by mirrors M5 & M6 and passed through the gain medium for the 2nd time. A reversed propagation was realized via the back-reflection of the CM, during which the 3rd and 4th passes were achieved. The exit of the four-pass amplified pulses was realized, as in the double-pass geometry, with the help of a double-pass through the λ/4-plate and the total reflection on TFP.

In this experiment, the beam diameter of the seed pulses was estimated to be around 0.15 mm using the 90/10-knife-edge method and that of the pump radiation was confirmed using a CCD camera (BGP-USB-SP503, Spiricon). Due to the spatial limitation of the employed optical components, the pump beam sizes of 0.63 and 0.525 mm were tested by setting L4:L5 ratio to 1:6 and 1:5, respectively. The four-pass amplifier setup in the laboratory was presented in Figure 6-3.

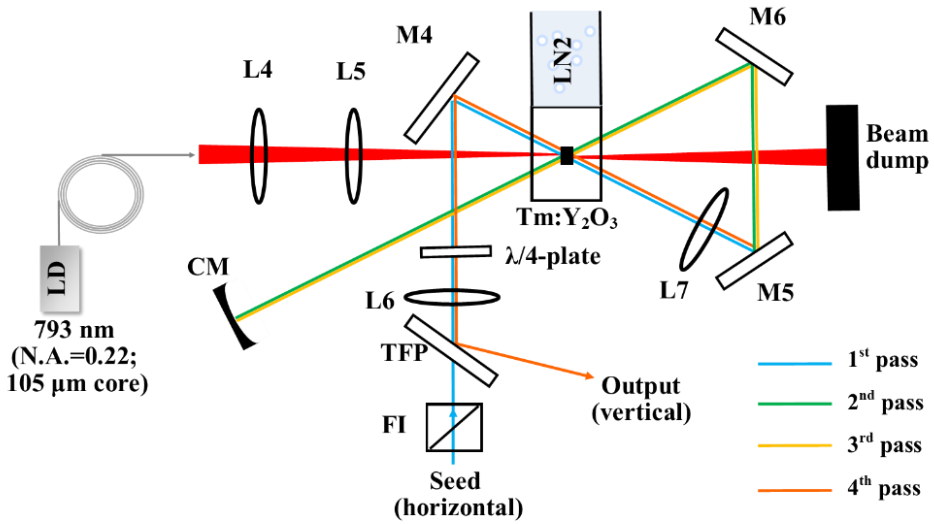

Figure 6-2 Sketch of the four-pass amplifier setup. Red line: pump radiation, blue line: the 1st laser pass, green line: the 2nd laser pass, yellow line: the 3rd laser pass, and the orange line: the 4th laser pass. L4 & L5: AR coated achromatic lenses; FI: Faraday isolator; TFP: thin film polarizer; L6 & L7: AR coated thin lens; M4-6: HR mirror; CM: curved mirror.

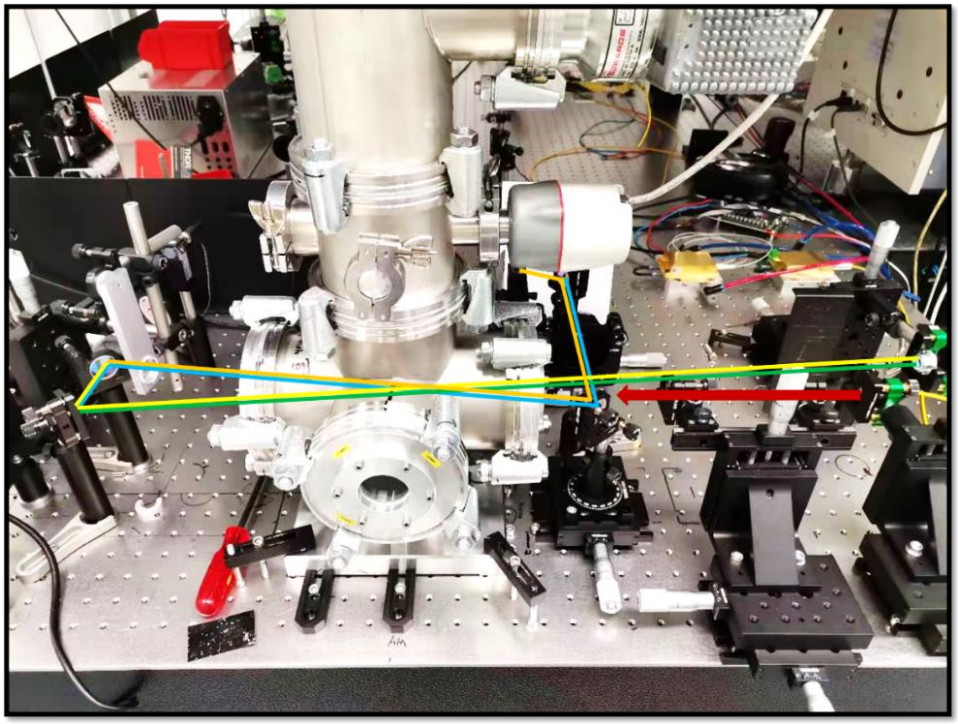

Figure 6-3 Photograph of the cryogenic four-pass amplifier setup in the laboratory.

6.2. Results and discussion

6.2.1 Optimization via a double-pass geometry

To amplify the pulse energy, a double-pass geometry as illustrated in 6.1.1 was implemented. The amplification process was characterized by changing three parameters: the amplifier

pump duration, the launched seed energy, and the repetition rate. In each characterization, we varied one parameter and fixed the other two.

In a first step, various pump durations (3.5 – 14 ms) were tested with the seed pulses fixed to 1 mJ, 10 Hz. The amplified pulse energy vs. incident pump energy was plotted for the single- and double-pass amplifications in Figure 6-4 (a) and (b), respectively. As shown in figure (a), after the 1st pass, the single pulse energy was amplified up to ~ 2 mJ for all pump durations. The increase of pump duration resulted in little variation of the maximum amplified pulse energy. In contrast, after the 2nd pass, as shown in figure (b), the maximum pulse energy decreased with the increase of pump duration, under which increased heat was deposited in the gain medium. Therefore, a pump duration of 3.5 ms was to be used in the further experiments.

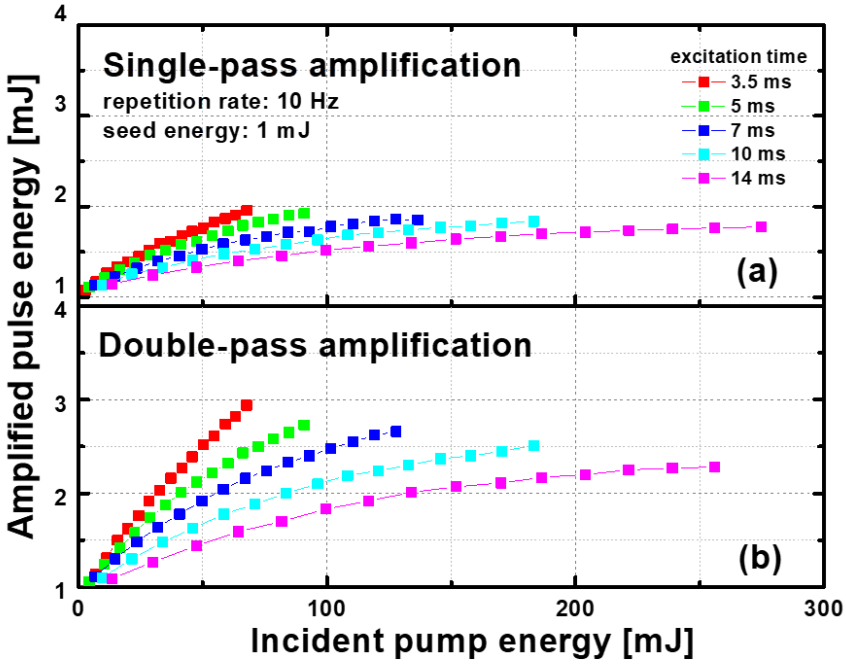

Figure 6-4 Amplified/pump energy characteristics for (a) single-pass, (b) double-pass amplification using different pump durations, and for (c) single-pass, (d) double-pass amplification using various incoming seed energies.

In a second step, various injected seed energies (0.6, 0.8, and 1 mJ) were tested with the amplifier pump duration fixed to 3.5 ms and the seed/pump repetition rate set to 10 Hz. The amplified/pump energy characteristics were presented in Figure 6-5 (a) and (b). As shown in both figures, the amplified pulse energy increased linearly with the incident pump energy. No saturation due to the pump was observed until the LD's maximum pump energy (67.7 mJ),

which indicates that employing a pump source of higher power can result in further energy scaling. Moreover, the increase of the injected seed energy resulted in an increase of the output pulse energy after both single- and double-pass amplifications. In the single-pass amplification, the maximum amplified pulse energy increased from 1.25 to 1.96 mJ for a seed energy increase from 0.6 to 1 mJ, while, after the double-pass amplification, it increased from 1.9 to 2.94 mJ.

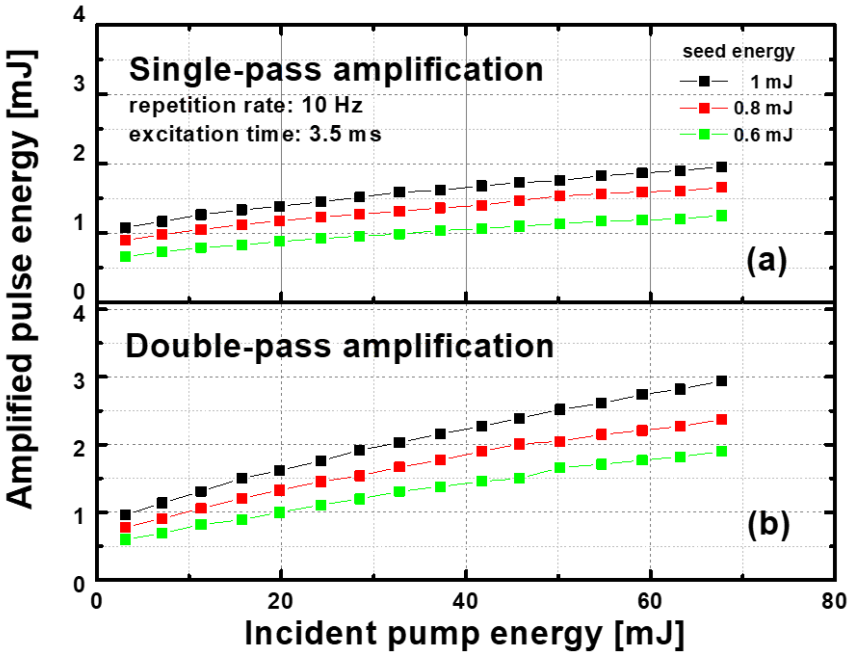

Figure 6-5 Amplified/pump energy characteristics for (a) single-pass, (b) double-pass amplification using different pump durations.

In a third step, the amplified single pulse energy was measured using 1 mJ seed pulses at various repetition rates (1 – 100 Hz). The pump duration was maintained at 3.5 ms. The amplified/pump energy characteristics are presented in Figure 6-6 (a) and (b). As shown in figure (a), the single pulse energy was amplified to the same level at a repetition rate until 50 Hz. Only at 100 Hz, we observed a small reduction, which was also shown in the double-pass amplification (Figure 6-6 (b)). This decrease at 100 Hz was mainly caused by the increased heat deposited in the sample, which required an enhanced cooling efficiency.

The pulse duration and corresponding beam profile measured at the maximum pulse energy are shown in Figure 6-7. The pulse duration was around 30 ns for all the repetition rates. Accordingly, a maximum peak power of 107, 92, 82, and 65 kW can be calculated for the double-pass amplified pulses at 1, 10, 50, and 100 Hz, respectively. As shown in the

insets, the obtained far field beam profiles are high-quality Gaussian and single mode for each repetition rate.

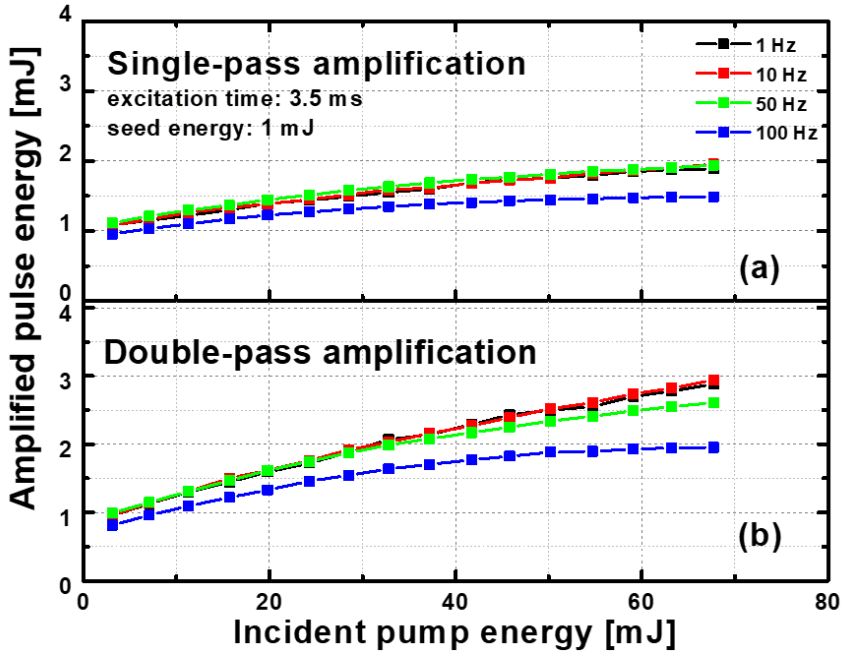

Figure 6-6 Amplified/pump energy characteristics for (a) single-pass and (b) double-pass amplification at various repetition rates.

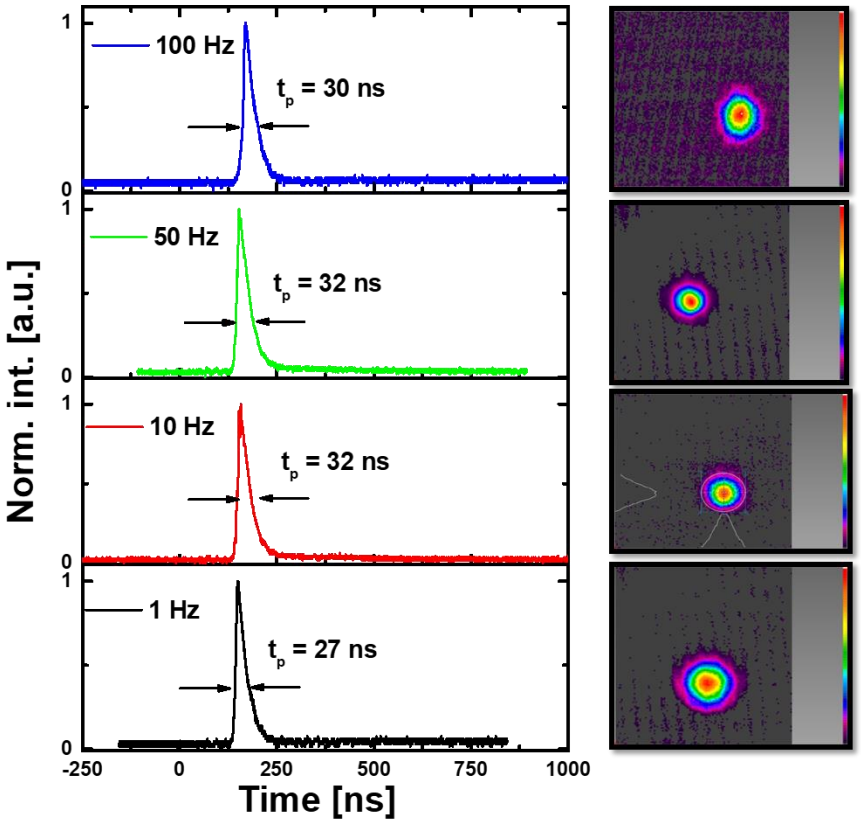

Figure 6-7 Oscilloscope trace of double-pass amplified pulses obtained at various repetition rates, insets: corresponding far field beam profile.

According to the results achieved in steps 1 & 3, one can see that this gain medium is sensitive to the temperature and requires high cooling efficiency. To confirm this fact, shorter pump durations were tested at 100 Hz, which should mitigate the thermal issues and improve the amplifier output. As shown in Figure 6-8, the amplified/pump energy exhibited clear linearity and less fluctuation, when the pump duration reduced to shorter than 2 ms. A maximum amplified pulse energy of 2.34 mJ was achieved using the 2-ms pump duration, and the highest optical conversion efficiency of 11 % (with respect to the incident pump energy of 18.0 mJ) was estimated using 1 ms pump duration. However, in this condition, the maximum amplified pulse energy was not improved because of the low pump energy limited by LD power. Thus, enhancing the pump source or/and increasing the cryostat's cooling efficiency will greatly help in the further energy scaling. The amplification at higher repetition rates (0.5 – 2 kHz) was, therefore, not executed with the current setup.

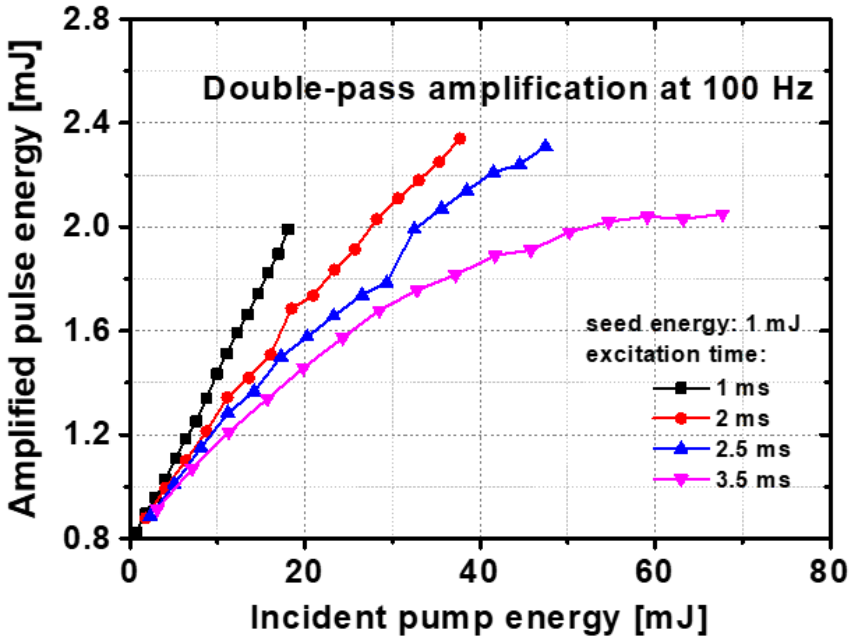

Figure 6-8 Amplified/pump energy characteristics for 100 Hz double-pass amplification using various pump duration (excitation time).

6.2.2 Energy scaling via a four-pass geometry

In this section, a four-pass amplifier was demonstrated for further energy scaling. The amplifier pump duration was set as 3.5 ms and two pump beam sizes (0.63 and 0.525 mm) were tested for the amplification. The seed pulses used had a pulse energy of 1 mJ and a

repetition rate of 10 Hz. Owing to the geometry convenience, the amplified pulse energy after single-, double- and four-pass was detected. All the results are presented in Figure 6-9. As shown in the figure, the amplified pulse energy after the single-pass showed a minor difference resulted from the change of pump beam size, while after the double- and four-pass, the maximum achieved pulse energy increased from 2.54 to 3.12 mJ and 4.21 to 4.87 mJ, respectively, when the smaller pump size was used.

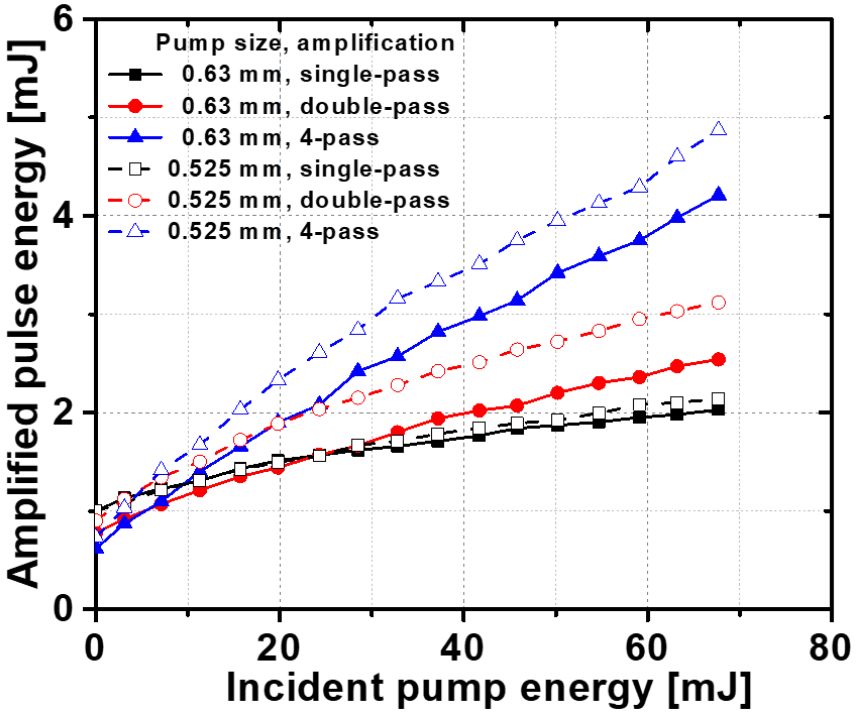

Figure 6-9 Amplified pulse energy measured after a single-, double- and four-pass amplification: solid lines are for the pump beam size of 0.63 mm and dashed lines for 0.525 mm.

The maximum single pulse energy of 4.87 mJ was achieved after the four-pass amplification under a maximum pump energy of 67.7 mJ (pump beam size of 0.525 mm), corresponding to an average power of 48.7 mW. The maximum optical conversion efficiency was estimated to be 7.2 % with respect to the incident pump energy. Based on the measured pulse duration of 28 ns, as shown in Figure 6-10, the maximum peak power can be calculated as 174 kW. The corresponding spatial profile of the maximum amplified pulses is shown as inset in Figure 6-10.

In addition, the energy stability of the amplified pulses was characterized. As shown in Figure 6-11, the energy stability for one hour monitoring was estimated to be 4.1 % rms with

an averaged value of 4.37 mJ and a standard deviation of 0.18 mJ. This energy stability agreed well with the seed stability we obtained in Section 5.2.2. The minimum, medium, and maximum energy were measured as 3.58, 4.38, and 4.87 mJ, respectively.

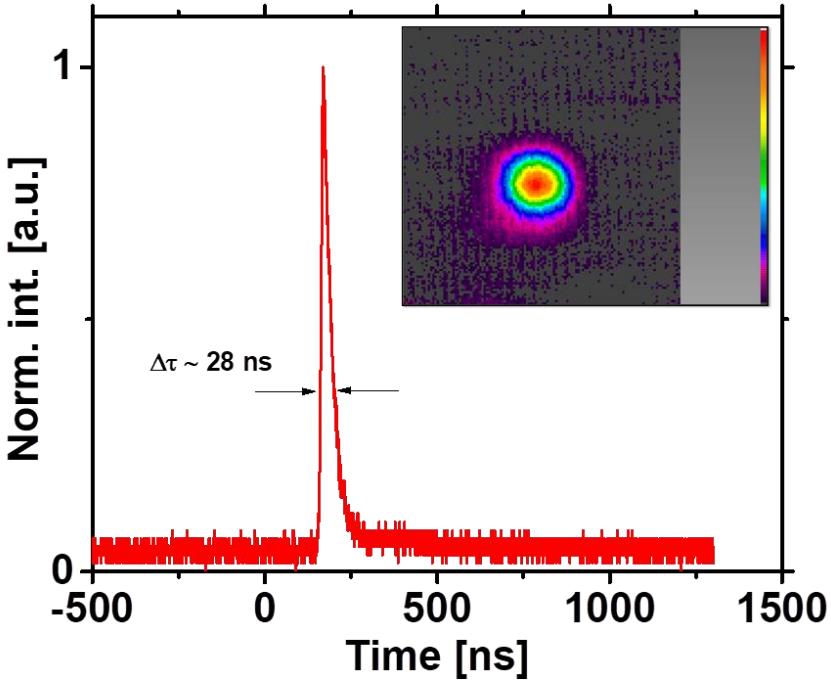

Figure 6-10 Oscilloscope trace of amplified pulses. Inset: the corresponding far field spatial beam profile.

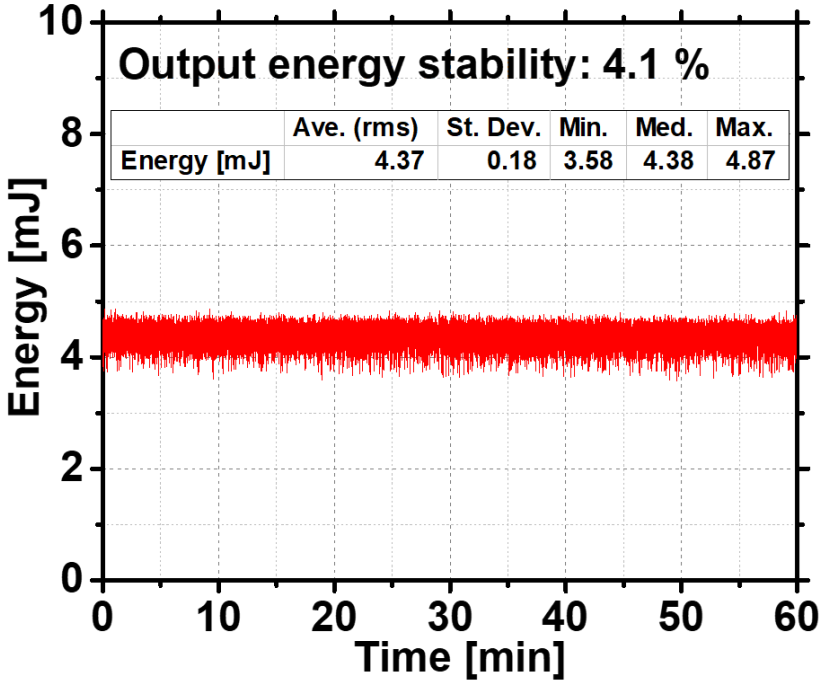

Figure 6-11 One-hour energy stability of amplified pulses after four-pass amplification

6.2.3 Small-signal gain

From the measured single-pass output, the small-signal gain g_0 was possible to be estimated. This parameter was important to characterize the amplifier gain medium. According to [1], the output energy fluence E_{out} can be written as a function of the incident seed fluence E_{in}, saturation fluence E_s, small-signal gain g_0 and sample length l:

$$E_{out} = E_s * ln\left(1 + \left[exp\left(\frac{E_{in}}{E_s}\right) - 1\right]\exp(g_0 l)\right). \quad (6.1)$$

Therefore, g_0 can be calculated from eq. (6.1) as:

$$g_0 = \frac{1}{l} * [ln\left(exp\left(\frac{E_{out}}{E_s}\right) - 1\right) - ln\left(exp\left(\frac{E_{in}}{E_s}\right) - 1\right)], \quad (6.2)$$

where $E_{in} = 5.97\, J/cm^2$ for a seed energy of 1 mJ, $E_s = \frac{h\upsilon}{\sigma_e} = 3.67\, J/cm^2$ for the 5 at.% Tm sample at 80 K, and $l = 0.3\, cm$ for the sample thickness were used.

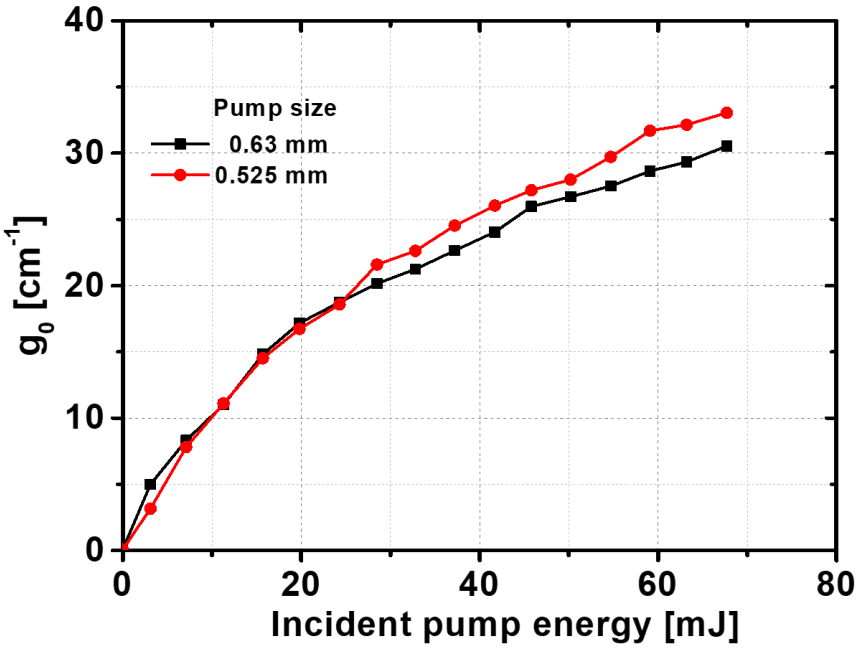

Figure 6-12 Small-signal gain per cm as a function of the incident pump energy measured for pump beam size of 0.63 mm (black line) and 0.525 mm (red line).

As shown in Figure 6-12, the g_0 showed a linear increase at lower pump energy (< 20 mJ) but a slight saturation, when the incident pump energy increased further. This saturation can be resulted from the insufficient cooling during high energy pumping, which again confirmed the temperature sensitivity of the gain medium. In addition, comparing the results achieved under the two pump beam sizes, one can see that g_0 was slightly higher in the higher pump region (> 25 mJ), when the smaller pump beam size was used. This could be resulted

from the increased pump intensity as well as from the increased beam overlapping efficiency between the pump and seed. Under the maximum LD pump energy (67.7 mJ), a maximum g_0 of 6.15 and 6.76 [cm^{-1}] were estimated for the pump beam sizes of 0.63 and 0.525 mm, respectively, corresponding to the gain factor values $G_0 = \exp(g_0 l)$ of 6.3 and 7.6. Further gain can still be achieved with enhanced pump energy.

6.3. Summary

In this chapter, multi-pass amplifiers were demonstrated via multiple geometries. The amplification parameters were characterized using a double-pass geometry. The energy scaling was achieved via a four-pass amplifier. A maximum single pulse energy of 4.87 mJ was achieved at 10 Hz with a pulse duration of 28 ns, corresponding to a peak power of 174 kW. At the far field output, a high-quality Gaussian and single mode beam was detected for the amplified pulses. The amplified output energy stability for one hour was estimated to be 4.1 %. These achieved results can fulfill the further application demands and proved that Tm:Y_2O_3 transparent ceramics are promising gain media for the cryogenic HAPP laser development.

6.4. Reference

[1] W. Koechner, *Solid-State Laser Engineering*, New York: Springer, p. 122, (1986).

Chapter 7

Summary and outlook

7.1. Summary of the achieved results
7.2. Contributions to the laser community
7.3. Outlook on future research

In this chapter, all the achieved results and the contributions to the laser community were summarized. A brief outlook on the future research was also introduced.

7.1. Summary of the achieved results

The most significant results achieved in this dissertation are as follows:

- The transparent ceramic active medium Tm:Y_2O_3 was characterized in terms of structure with SEM, XRD and Raman spectroscopy measurements. The results confirmed that this material is in line with its crystalline counterpart.
- A detailed spectroscopic characterization of the Tm:Y_2O_3 transparent ceramic was presented from 6 to 300 K for various manifolds. Crucial laser design parameters were obtained, such as the exact pump wavelength, absorption bandwidth, transition cross-sections, radiative lifetime, etc.
- The laser potential of the Tm:Y_2O_3 active medium was confirmed by demonstrating a cryogenic CW laser at 80 to 200 K. At 80 K, a maximum output of 8.2 W was obtained using the 5 at.% sample, corresponding to a slope efficiency of 43.0 % with respect to the incident pump power. The laser wavelength was 1932 nm with a high-quality Gaussian single mode beam.
- A seed source at 1932 nm with high quality Gaussian beam profile was demonstrated at 80 K. The pulsed lasing potential of Tm:Y_2O_3 was confirmed from 1 Hz to 2 kHz. A maximum pulse energy of 1.35 mJ was achieved at 10 Hz with a pulse duration of 30 ns. The maximum obtained peak/average power was 45 kW at 10 Hz and 1.2 W at 2 kHz, respectively.
- A multi-pass amplifier was demonstrated via four-pass geometry. A maximum amplified single pulse energy of 4.87 mJ was achieved. The corresponding pulse duration, repetition rate, and peak power were 28 ns, 10 Hz, and 174 kW, respectively.

7.2. Contributions to the laser community

This work provides a detailed temperature-dependent spectroscopy study on the Tm:Y_2O_3 transparent ceramic for the first time. This study provided valuable data, such as the temperature-dependent absorption/emission/gain cross-sections, crucial laser design

parameters, etc., for further material relevant scientific research as well as for the laser developments based on such material.

This work also reported the first demonstration of a cryogenically cooled 2 μm laser based on the Tm:Y_2O_3 transparent ceramics. The CW, pulsed and amplification laser potential of this material was tested and confirmed. This can serve as a useful reference for further laser engineering. A record peak power was achieved, to the best of our knowledge, by using such a gain medium. The obtained output can fulfill multiple application demands in the future.

7.3. Outlook on future research

The further research can be firstly focused on the optimization of the current laser setup by methods, such as:

- Employing active media with higher dopant concentration or larger volume;
- Improving the cooling efficiency of the cryostat;
- Increasing the pump energy by using pump sources with higher power, or via double-side pumping.

Further work can also be concentrated on the applications of the current setup in several fields, such as:

- Multi-stage amplifier system demonstration, in which the current amplifier can serve as a preamplifier stage,
- Ho-doped laser development, for which the current laser can serve as a reasonable pump source.

Besides, since the properties of the active medium Tm:Y_2O_3 transparent ceramic were well studied, other laser designs using this active medium can also be investigated, such as passive Q-switched laser or mode-locked laser.

In addition, other Tm-doped materials are also interesting for the laser development. A similar methodology can be applied in a further study with Tm-doped Sc_2O_3, Lu_2O_3, or mixed sesquioxide ceramic materials, which have outstanding properties for the laser development.

PUBLICATION LIST

DISSERTATION RELEVANT

Publications in impact journal

1. **F. Yue**, V. Jambunathan, S. P. David, X. Mateos, J. Šulc, Martin Smrž, and T. Mocek, "Diode-pumped master oscillator power amplifier system based on cryogenically cooled Tm:Y_2O_3 transparent ceramics," Opt. Mater. Express, (2021). (submitted)
2. **F. Yue,** V. Jambunathan, S. P. David, X. Mateos, M. Aguiló, F. Díaz, J. Šulc, A. Lucianetti, and T. Mocek, "Spectroscopy and diode-pumped continuous-wave laser operation of Tm: Y_2O_3 transparent ceramic at cryogenic temperatures," Appl. Phys. B 126, 44 (2020).

Conference proceeding

3. **F. Yue**, V. Jambunathan, S. P. David, X. Mateos, J. Šulc, A. Lucianetti, and T. Mocek, "Development of high average and peak power laser around 2 μm based on cryogenically cooled Tm:Y_2O_3 transparent ceramic," in OSA High-brightness Sources and Light-driven Interactions Congress 2020 (EUVXRAY, HILAS, MICS), paper JW1A.30 (2020).

ADDITIONAL WORK

Publications in impact journal

4. J. Körner, V. Jambunathan, **F. Yue**, J. Reiter, O. Slezak, A. Lucianetti, J. Hein, T. Mocek, and M. C. Kaluza, "Pulse pumped, cryogenically cooled, q-switch Tm:YAG laser at 1.88 μm ," High Power Laser Sci. 9, E11, (2021).
5. S. P. David, V. Jambunathan, **F. Yue**, A. Lucianetti, and T. Mocek, " Diode Pumped Cryogenic Yb:$Lu_3Al_5O_{12}$ Laser in Continuous Wave and Pulsed Regime," Opt. Laser Technol. 135, 106720 (2021).
6. **F. Yue**, P. Loiko, M. Chen, J. M. Serres, Y. Wang, J. Li, L. Basyrova, E. Dunina, A. Kornienko, L. Fomicheva, S. Dai, Z. Chen, J. E. Bae, T. G. Park, F. Rotermund, V. Jambunathan, A. Lucianetti, T. Mocek, M. Aguiló, F. Díaz, U. Griebner, V. Petrov, and X. Mateos, "Spectroscopy and diode-pumped laser operation of transparent Tm:$Lu_3Al_5O_{12}$ ceramics produced by solid-state sintering," Opt. Express 28, 28399-28413 (2020).
7. S. P. David, V. Jambunathan, **F. Yue**, B. J. Le Garrec, A. Lucianetti, and T. Mocek, "Laser performances of diode pumped Yb:Lu_2O_3 transparent ceramic at cryogenic temperatures," Opt. Mater. Express 9, 4669-4676 (2019).
8. S. P.David, V. Jambunathan, **F. Yue**, A. Lucianetti, and T. Mocek, "Efficient diode pumped Yb:Y_2O_3 cryogenic laser," Appl. Phys. B 125, 137 (2019).
9. S. P. David, V. Jambunathan, **F. Yue**, P. Navratil, M. Mika, A. Lucianetti, and T. Mocek, "Effect of Gd^{3+}/Ga^{3+} on Yb^{3+} emission in mixed YAG at cryogenic temperature," Ceram. Int. 45, 9418-9422 (2019).

10. P. Navratil, V. Jambunathan, S. P. David, **F. Yue**, J. M. Serres, X. Mateos, M. Aguiló, F. Díaz, U. Griebner, V. Petrov, A. Lucianetti, and T. Mocek, "Continuous-wave and passively Q-switched cryogenic Yb:$KLu(WO_4)_2$ laser," Opt. Express 25, 25886-25893 (2017).

11. V. Jambunathan, P. Navratil, T. Miura, **F. Yue**, A. Endo, A. Lucianetti, and T. Mocek, "Cryogenic Yb:YGAG ceramic laser pumped at 940 nm and zero-phonon-line: a comparative study," Opt. Mater. Express 7, 477-483 (2017).

Conference proceeding

12. M. Chen, P. Loiko, **F. Yue**, V. Jambunathan, A. Lucianetti, T. Mocek, J. M. Serres, M. Aguiló, F. Díaz, T. G. Park, J. E. Bae, F. Rotermund, X. Xu, J. Xu, S. Dai, Z. Chen, U. Griebner, V. Petrov, X. Mateos, and A. Major "Multi-watt continuous-wave and passively Q-switched Tm:$CaYAlO_4$ micro-lasers", Proc. SPIE 11259, Solid State Lasers XXIX: Technology and Devices, 1125927 (2020).

13. F. Yue, V. Jambunathan, S. P. David, J. Reiter, J. Körner, D. Klöpfel, J. Hein, M. C. Kaluza, A. Lucianetti, and T. Mocek "Diode-pumped cryogenic Tm:$LiYF_4$ laser", Proc. SPIE 11033, High-Power, High-Energy, and High-Intensity Laser Technology IV, 110330E (2019).